MONOLAYER ANALYSIS USING HIGH-RESOLUTION RUTHERFORD BACKSCATTERING SPECTROSCOPY

KAORU NAKAJIMA

2009

ACKNOWLEDGEMENTS

I would like to express my deepest gratitude to Professor Kenji Kimura for the guidance, constructive suggestions, valuable discussions and continuous encouragement throughout this study.

I would like to heartily appreciate Professor Motofumi Suzuki for his valuable advice and encouragement.

I am grateful to Professors Michi-hiko Mannami, Yoshikazu Fujii and Yasufumi Susuki for offering the guidance and imparting the basic knowledge in this research field of at the beginning of this study.

I am grateful to Professors Akio Itoh, Ikuji Tkagi, and Nobutsugu Imanishi, and Messrs. Kouji Yoshida and Keizou Norisawa, and the members of the Department of Nuclear Engineering and the Quantum Science and Engineering Center (QSEC) of Kyoto University for their kind help in the operation of the 4 MV Van de Graaff accelerator.

I wish to thank many colleagues and students who have collaborated with me in this study. I was greatly helped by Dr. Kazumasa Narumi, Dr. Ming Zhao, Messrs. Kazuomi Ohshima, Yoshio Ooka, Atsushi Konishi, Yasutaka Okazaki, Noriyuki Hosaka, Yoshihiko Hano, Shinji Joumori, Kohei Kinoshita, Wataru Sakai, Yasutaka Okura, Shigetaka Hosoi, Akira

Fujiyoshi, and many other students in my experiments.

Finally, I would like to sincerely thank my wife, Yae, my daughters, Chimomo, Chiori, Chihiro, and my parents, Yasuko and Shigeo for their reception of my research life and continuous encouragement.

Kyoto
July, 2009 Kaoru Nakajima

CONTENTS

Chapter 1

Introduction

1.1 Growing importance of ultrathin film characterization

In the modern electronic technology, thin films are used as key components, such as gate dielectric films and gate electrodes in metal-oxide-semiconductor field-effect transistors (MOSFETs) in ultra-large scale integrations (ULSIs). To upgrade these electronic devices their dimensions have shrunk to range of nanometers. Consequently accurate control of quality of the films and the interfaces between them is of increasing importance for further advance of the devices. In addition, increasing diversity of desired functions of the devices leads to variety of materials and complexity of the film structures. Therefore advanced techniques are required to characterize these ultrathin films at the atomic level. Information of elemental composition as well as film thickness and interface abruptness is essential for the film characterization because various properties of the film depend on them.

1.2 Analytical techniques for compositional depth profiling

There are several widely-used analytical techniques for compositional depth profiling, such as X-ray photoelectron spectroscopy (XPS), secondary ion mass spectrometry (SIMS) and Rutherford backscattering spectroscopy (RBS). In the following paragraphs, a short description of these techniques and their drawbacks and advantages for high-resolution compositional depth profiling will be given.

X-ray photoelectron spectroscopy (XPS)

X-ray photoelectron spectroscopy (XPS) is currently the most widely used surface-analytical technique. The specimen surface to be analyzed is irradiated with soft X-ray photons (typically in range of keV). When a photon of energy $h\nu$ interact with an electron in the level X with the binding energy E_B ($h\nu > E_B$), the entire photon energy is transferred to the electron, which is consequently emitted from the surface with the kinetic energy, $E(h\nu, X) = h\nu - E_B - \Phi_S$, where Φ_S is a small work function term. Because each element has a unique set of the binding energies of electrons in core levels, measurement of the kinematic energy of photoelectrons enables elemental analysis. In addition, the binding energies of electrons belonging to an atom depend on its chemical environment, therefore chemical information of the atom is available as well as the

elemental composition. XPS can be applied for all elements except hydrogen and helium.

Since the typical inelastic mean free path of photoelectrons (~ keV) in a solid is about 2–10 nm, XPS provides the average chemical composition in the surface region of depth less than several nm. When depth distribution of chemical composition within depth of several nm is required, non-destructive depth profiling is possible from a series of measurements with various emission angles of photoelectrons to be detected. This technique is referred to as angle-resolved XPS (AR-XPS). AR-XPS enables nondestructive depth profiling of the chemical composition near the surface with sub-nanometer resolution. However it is usually difficult to extract the unique depth profile from the angle dependence of the energy spectra. This is why the smoothest profile among possible depth profiles which can reproduce the measured angle dependence is usually adopted as the "real" depth profile (maximum entropy method: MEM).

Secondary ion mass spectrometry (SIMS)

When a heavy energetic particle such as an argon ion (typically 1 to 15 keV) hits a solid target, it penetrates through the surface and imparts its energy to the solid along the pathway due to atomic and electronic scattering. As a result of ion-atom collisions on the way some target atoms are displaced from their original position. The displaced atom (primary knock-on atom) may recoil additional target atoms if it have sufficient

energy, resulting in a complex sequence of collisions and displacements. This sequence is called a collision cascade. When the cascade spreads out from the path of the primary ions and then reach to the surface, neutral or ionized atoms or clusters are emitted from the surface. Since most of the secondary particles originate from the top monolayers of the solid, detecting the ionized particles with a mass spectrometer informs us about the elemental compsition of the surface layer. Depth profiling is avalable from time evolution of the secondary ion yields because the surface is gradually etched by the irradiation of primary ions itself.

Because SIMS can provide some chemical information of a specimen with remarkably high sensitivity to elements, it is widely employed for compostional depth profiling near the surface, in particular, that of minor constituent elements such as dopants in semiconductors. However, there are still several difficulties in SIMS analysis in spite of recent improvements in SIMS measurements (use of sub-keV Cs^+ or O^+ ions as primary ions, and/or grazing-angle irradiation). One of the difficulties is the so-called matrix effect [1]; i.e., the relative sensitive factor (RSF) for an element generally depends on the matrix composion of the specimen surface. Matrix effect is due to the fact that ionization probabilities of sputtered atoms are highly dependent on their chemical environment within the analyzed material. If this effect is significant, accurate composition can not be extracted straightforward from the detected secondary ion yields with constant RSFs, which are usually applied in composition analysis by SIMS. The other difficulty is surface

transient effects in SIMS, that is, nonequilibrium nature of sputtering events (sputtering rate, ionization probability) at the beginning of the measurement. This may be caused by accumulation of the primary ions implanted near the surface. This effect leads to inaccurate estimate of the measured depth and the composition near the original surface of the specimen.

Rutherford backscattering spectroscopy (RBS)

Rutherford backscattering spectroscopy (RBS) is one of the most frequently used technique for quantitative analysis of elemental compotition, thickness and depth profiles of solid samples near the surface region. In RBS, a beam of monoenergetic ions, usually H^+ or He^+ of typical energy 0.5 to 2.5 MeV, is directed at a target, and the energies of the ions which are scattered backwards are analyzed. Because of its quantitative reliability, RBS often serves as a standard for other techniques.

In the following sections, the principles of RBS as well as the possible factors limiting the depth resolution will be described in detail.

1.3 Fundamentals of RBS [2]

1.3.1 Kinematics of elastic collisions

In Rutherford backscattering spectroscopy, a beam of monoenergetic light ions is incident on a solid target and the energy spectrum of the particles scattered from target atoms into a particular angle is measured. In the collision, a part of energy of the projectile is transferred to the target atom. The energy of the scattered particle depends on the masses of the projectile and the target atom, which enables elemental analysis of the solid target.

The energy transfer in an elastic collision between a projectile and a target atom can be solved by applying the principles of conservation of energy and momentum. The primary energy of a projectile (mass M_1) is E_0, while a target atom (mass M_2) is at rest before collision. The energy E_1 of the scattered projectile is determined by the scattering angle θ for the laboratory system of coordinates (Fig. 1.1). The ratio of the projectile

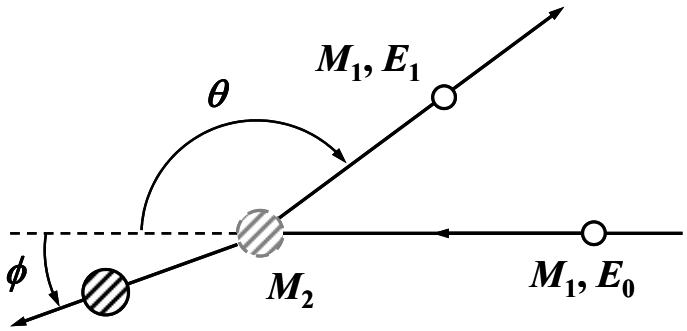

Fig. 1.1 Schematic drawing of an elastic collision between a projectile of mass M_1 and energy E_0 and a target atom of mass M_2 which is initially at rest.

energies for $M_1 < M_2$ is

$$\frac{E_1}{E_0} = \left[\frac{M_1 \cos\theta + \sqrt{M_2^2 - M_1^2 \sin^2\theta}}{M_1 + M_2} \right]^2 . \tag{1.1}$$

The energy ratio E_1/E_0 is called the kinematic factor k. The energy difference $E_2 = E_0 - E_1$ taken by the target atom is given by

$$\frac{E_2}{E_0} = \frac{4M_1M_2}{(M_1 + M_2)} \cos^2\varphi , \tag{1.2}$$

where φ is the recoil angle. For θ = 180º, the maximum energy is transferred to the target atom, where

$$\frac{E_1}{E_0} = \left(\frac{M_2 - M_1}{M_1 + M_2} \right)^2 , \tag{1.3}$$

$$\frac{E_2}{E_0} = \frac{4M_1M_2}{(M_1 + M_2)^2} . \tag{1.4}$$

For a given M_1, E_0 and scattering angle θ, the mass M_2 of the target atom is determined from Eq. (1.1) by measuring the energy E_1. Figure 1.2 shows the kinematic factor k for ^{4}He projectile as a function of the mass M_2 of the target atom at various scattering angles. Since the difference of k for a given difference of M_2 increases with scattering angle for relatively large M_2 ($M_2 \geq 30$), an experimental geometry with a large scattering angle is preferable for high mass resolution.

1.3.2 Scattering cross section

As described in the previous section, the target atom is identified by the energy of the scattered particle after the elastic collision. The number N_s (= Nt) of the target atoms per unit area is determined by the number Q_D of

the scattered particles for a given number Q of the projectiles incident on the target. For the geometry of Fig. 1.3, the number Q_{D} of the particles scattered into a solid angle Ω is given as

$$Q_D = \frac{d\sigma(\theta)}{d\Omega}\Omega Q\frac{N_s}{\sin\theta_i}, \tag{1.5}$$

where θ_{i} is the angle of incidence with respect to the surface and $\mathrm{d}\sigma(\theta)/\mathrm{d}\Omega$ is the differential scattering cross section of a target atom for scattering a projectile at an angle θ. The yield Y of detected particles is $Q_{\mathrm{D}}\cdot\varepsilon$, where ε is the efficiency of the detector, i.e.,

$$Y = \frac{d\sigma(\theta)}{d\Omega}\Omega Q\frac{N_s}{\sin\theta_i}\varepsilon\,. \tag{1.6}$$

From Eq. (1.5) one can note that the cross section $\mathrm{d}\sigma(\theta)/\mathrm{d}\Omega$ has the

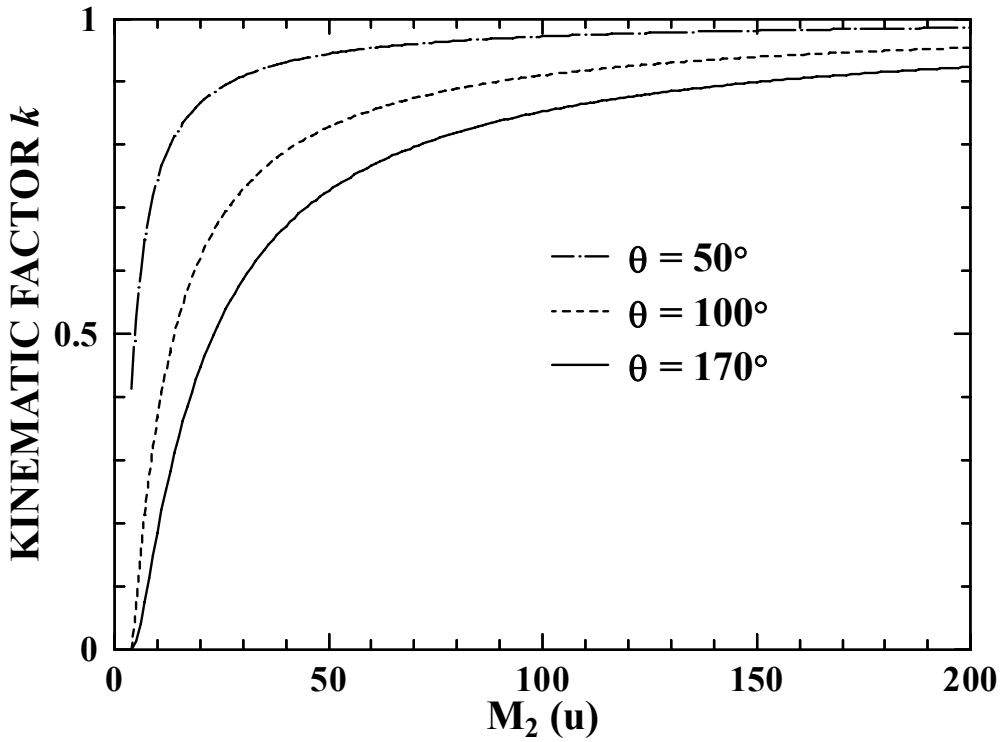

Fig. 1.2 Kinematic factor k for ^{4}He projectile as a function of the mass M_2 of the target atom at various scattering angles.

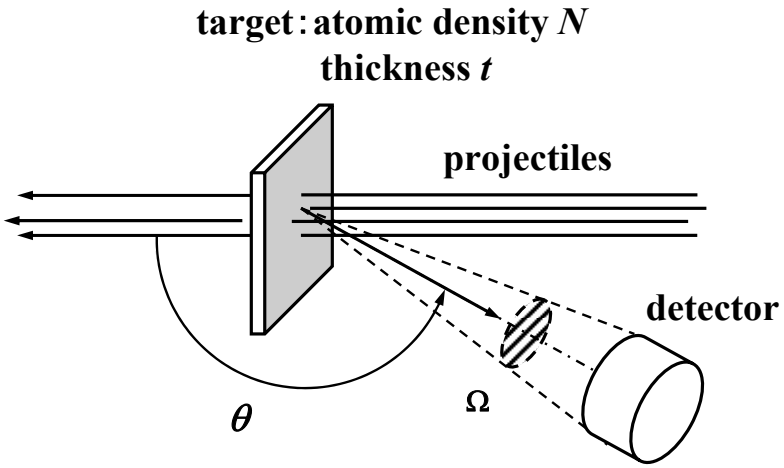

Fig. 1.3 Simplified layout of a scattering experiment to demonstrate the concept of differential scattering cross section.

dimension of an area.

The scattering cross section can be calculated from the force that acts during the collision between the projectile and the target atom. For most case in backscattering spectroscopy, the distance of the closest approach during the collision is smaller than the orbit of electrons, so that the force can be described as an unscreened Coulomb repulsion of two charged nuclei with charge of Z_1e and Z_2e, where Z_1 and Z_2 are the atomic numbers of the projectile and the target atom and e is the magnitude of charge of an electron. The screening of the charge of the nuclei by electrons gives an only small correction. The force F at a distance r between the projectile and the target atom is given in the cgs system by

$$F = \frac{Z_1 Z_2 e^2}{r^2}. \tag{1.7}$$

As demonstrated in Fig. 1.4, the nucleus of the target atom is assumed to be a point charge fixed at the origin O. The projectile

approaches the target atom initially parallel to line *OA* at a distance *b* with a kinematic energy of *E* and finally leaves the target atom parallel to line *OB*, which makes an angle θ_c with *OA*. The suffix c means that the angle is defined in the center-of-mass (COM) system. The scattering angle θ_c can be uniquely related to the impact parameter *b* by classical mechanics as

$$\tan\frac{\theta_c}{2} = \frac{Z_1 Z_2 e^2}{2Eb}. \tag{1.8}$$

The differential cross section $d\sigma(\theta_c)/d\Omega$ is, by the definition, expressed as

$$2\pi b db = -\frac{d\sigma(\theta_c)}{d\Omega}\cdot 2\pi \sin\theta_c d\theta_c, \tag{1.9}$$

that is,

$$\frac{d\sigma(\theta_c)}{d\Omega} = \frac{-b}{\sin\theta_c}\frac{db}{d\theta_c}. \tag{1.10}$$

From Eqs. (1.8) and (1.10),

$$\frac{d\sigma(\theta_c)}{d\Omega} = \left(\frac{Z_1 Z_2 e^2}{4E}\right)^2 \frac{1}{\sin^4\theta_c/2}. \tag{1.11}$$

It should be noted that the scattering cross section is proportional to Z_1^2, Z_2^2, $(\sin^4\theta_c/2)^{-1}$ and E^{-2}.

We discussed the scattering cross section in the center-of-mass system above. The cross section (Eq. (1.11)) is true for the scattering of a particle by a fixed center of force. However, the target atom is not fixed but recoils from its initial position. As a result, the scattering angle θ in the laboratory system differs from the angle θ_c in the center-of-mass system. The angles are related by

$$\tan\theta = \frac{\sin\theta_c}{\cos\theta_c + M_1/M_2}. \tag{1.12}$$

By the transformation, Eq. (1.11) is rewritten as

$$\frac{d\sigma(\theta)}{d\Omega}=\left(\frac{Z_1Z_2e^2}{4E}\right)^2\frac{4}{\sin^4\theta}\frac{(\{1-[(M_1/M_2)\sin\theta]^2\}^{1/2}+\cos\theta)^2}{\{1-[(M_1/M_2)\sin\theta]^2\}^{1/2}}, \qquad (1.13)$$

which can be expanded for $M_1 < M_2$ in a power series to give

$$\frac{d\sigma(\theta)}{d\Omega}=\left(\frac{Z_1Z_2e^2}{4E}\right)^2\left[\sin^{-4}\frac{\theta}{2}-2\left(\frac{M_1}{M_2}\right)^2+\cdots\right], \qquad (1.14)$$

where the terms omitted in Eq. (1.14) are of order of $(M_1/M_2)^4$ and of the higher order. It is clear that Eq. (1.14) is reduced to Eq. (1.11) in the limit of $M_1 << M_2$, and that the corrections are generally small.

1.3.3 Deviation from Rutherford scattering

In the previous section, the Rutherford scattering cross section is derived from a Coulomb potential between the projectile with charge of Z_1e and the target atom with charge of Z_2e. This is a good approximation when the energy of the projectile is sufficiently high so that the projectile penetrates well inside the electron shells of the target atoms. In small-angle

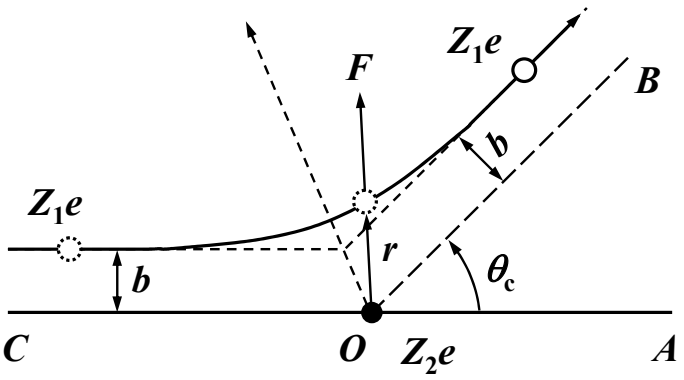

Fig. 1.4 Rutherford scattering geometry. The scattering angle θ_c defined in the center-of-mass system can be related to the impact parameter b by classical mechanics.

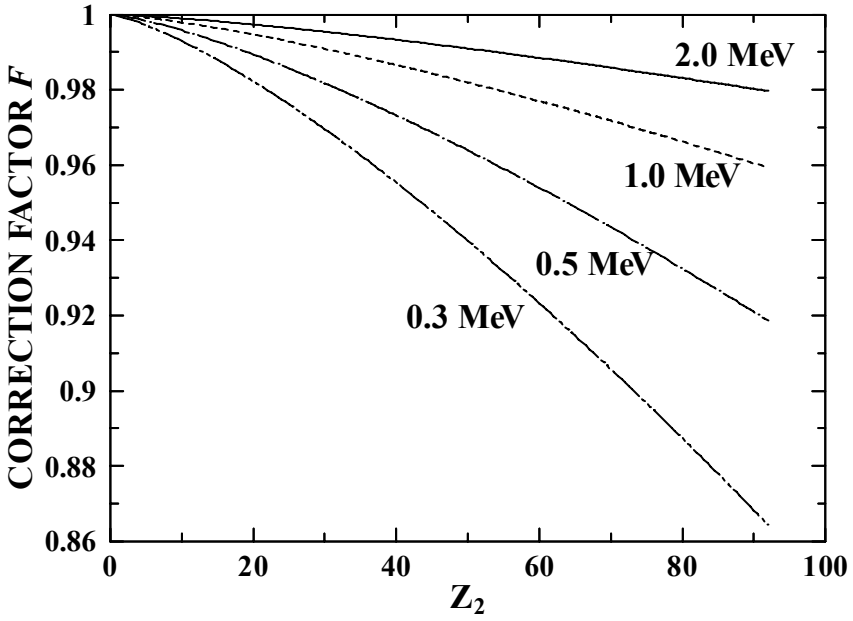

Fig. 1.5 Correction factor F for ^{4}He scattering from a target atom of the atomic number Z_2 at various kinetic energies of the projectile.

scattering or for low-energy and/or heavy projectile, however, the projectile does not completely penetrate through the electron shells and consequently the charge of the nucleus of the target atom is partially screened by the inner electrons of the target atom.

In analysis of Rutherford backscattering spectroscopy, the influence of screening can be approximately treated with a correction factor F. The screened Coulomb cross section σ_{sc} is given by the product of the cross section in Eq. (1.13) and the factor F as

$$\sigma_{sc} = \sigma(\theta)F\,, \tag{1.15}$$

where $F = (1-0.049Z_1Z_2^{4/3}/E)$ and E is given in keV [3]. Values of the correction factor are given for He^+ scattering from atoms, Z_2 in Fig. 1.5. The deviation from pure Rutherford scattering cross section is only 3%

with 1 MeV He^+ incidence on Pb atoms, while it is significant for lower energy of incident ions and heavy target atoms.

1.3.4 Energy loss and stopping

Penetrating a solid target in Rutherford backscattering, energetic light particles such as He ions gradually lose their energy mainly through excitation of target electrons or ionization of target atoms. The energy loss due to excitation or ionization is a discrete process, but can be regarded as a continuous process to a good approximation. What we need in usual analysis with Rutherford backscattering is the average energy loss during the penetration of ions into a given material. The average energy loss is usually expressed in terms of stopping power S (= dE/dx) or stopping cross section ε (= S/N), where N is the atomic density of the target. One can get the value of ε for a proton or a ^{4}He ion penetrating in a solid consisting of one element in Refs. [4-6], where a set of empirical formulae available over wide range of projectile energy is given together with tabulated parameters. Recently, the SRIM code has been widely used as well to estimate stopping powers or stopping cross sections.

For a target that contains more than one element, the energy loss is given by summing the losses of the constituent elements weighted by the abundance of the elements. This reasonable assumption is known as Bragg's rule and states that the stopping cross section ε^{AmBn} of the solid with composition A_mB_n is given by

$$\varepsilon^{A_mB_n} = m\varepsilon^A + n\varepsilon^B, \qquad (1.16)$$

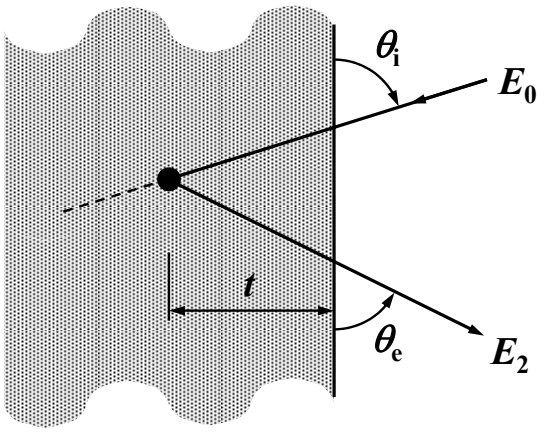

Fig. 1.6 Schematic drawing of backscattering geometry to demonstrate the energy loss of a projectile that scatters from depth *t*.

where ε^A and ε^B are the stopping cross sections of the atomic constituents A and B.

Consider that a projectile with primary energy E_0 is scattered from a target atom at the depth t and emerges from the target surface as shown in Fig. 1.6. The angles of incidence and exit of the projectile are θ_i and θ_e, respectively, from the surface plane. The projectile loses energy along its incident path and has energy E_1 just before the scattering from the target atom. E_1 is given as

$$E_1 = E_0 - \int^{t/\sin\theta_i} \frac{dE}{dx} dx = \left.\frac{dE}{dx}\right|_{in} \cdot t / \sin\theta_i , \tag{1.17}$$

where $\left. dE/dx \right|_{in}$ is an average stopping power along the incident pass. After the scattering the projectile emerges with energy

$$\begin{aligned} E_2 &= kE_1 - \int^{t/\sin\theta_e} \frac{dE}{dx} dx \\ &= kE_0 - t\left(\frac{k}{\sin\theta_i} \left.\frac{dE}{dx}\right|_{in} + \frac{1}{\sin\theta_e} \left.\frac{dE}{dx}\right|_{out} \right), \end{aligned} \tag{1.18}$$

where $dE/dx|_{out}$ is an average stopping power along the outward pass. The energy width ΔE of the particles scattered from a film of thickness Δt is

$$\Delta E = \Delta t \left(\frac{k}{\sin\theta_i} \frac{dE}{dx}\bigg|_{in} + \frac{1}{\sin\theta_e} \frac{dE}{dx}\bigg|_{out} \right) = \Delta t\,[S]. \tag{1.19}$$

[S] is often referred to as the backscattering energy loss factor. For thin films, the change in energy along the inward and outward paths is so small that one can use the "surface energy approximation", in which $dE/dx|_{in}$ and $dE/dx|_{out}$ are evaluated at energy E_0 and kE_0, respectively. In this approximation the energy width ΔE from a film of thickness Δt is

$$\Delta E = \Delta t \left(\frac{k}{\sin\theta_i} \frac{dE}{dx}\bigg|_{E_0} + \frac{1}{\sin\theta_e} \frac{dE}{dx}\bigg|_{kE_0} \right). \tag{1.20}$$

1.3.5 Depth resolution

In Rutherford Backscattering spectroscopy one can determine compositional depth profile of the specimen from the energy spectrum of the scattered projectiles. The relation between the depth resolution δt and the energy resolution δE is given by Eq. (1.19) as

$$\delta t = \delta E / [S]. \tag{1.21}$$

For a given detector energy resolution, therefore, the depth resolution is improved by enlarging the energy loss factor [S]. Generally this is done by grazing-angle technique so that the path length of ions in the sample and hence the energy loss is a maximum. From the definition of [S] in Eq.

(1.19), the depth resolution is optimized by detecting scattered ions emerging from the surface at grazing angle, $\theta_e << 1$. With this geometry depth resolution as small as 2 nm can be achieved using a standard solid-state detector (typically $\delta E \sim 10$ keV for MeV He ions). However, improvement of depth resolution using the grazing-angle technique is limited by following factors. (a) Finite detector acceptance angle, (b) Surface roughness, and (c) Energy loss straggling.

(a) *Finite detector acceptance angle*. In any system a detector has a finite acceptance angle, which constitutes a broadening to the scattering angle set by the geometry. Uncertainty in the scattering angle due to the acceptance angle is typically less than 1°, but this leads to significant difference in the path length and the energy loss for the grazing-angle geometry (typically $\theta_e < 5°$). In addition, the broadening of the scattering angle causes uncertainty in the kinematic factor k (kinematic broadening). Extremely small acceptance angle is impractical from the viewpoint of measuring time or required ion fluence.

(b) *Surface roughness*. This also leads to uncertainty in the path length of ions in the sample and hence the energy loss. This influence is enhanced in the grazing-angle geometry.

(c) *Energy loss straggling*. An energetic particle moving through a medium loses energy via many individual encounters. Such a discrete process is subject to statistical fluctuation. As a result, identical energetic particles, which have the same initial velocity, do not have exactly the same energy after passing through a given thickness of a homogeneous

medium. That is, the energy loss ΔE is subject to fluctuations. This is called energy loss straggling. Energy loss straggling places a finite limit on the depth resolution.

1.3.6 Energy loss straggling

Light particles such as H or He in the MeV energy range lose energy primarily by encounters with the electrons in the target, and the statistical fluctuations in these electronic interactions is the dominant contribution to the energy loss straggling. The distribution of energy loss ΔE for the particles after passing through a foil gives a distribution that is approximately Gaussian when ΔE is small compared with the incident energy E_0. Thus the probability of finding an energy loss between ΔE and ΔE+dΔE is expressed as

$$P(\Delta E)d\Delta E = \frac{1}{\sqrt{2\pi\Omega^2}}\exp\left[\frac{-(\Delta E-\Delta E_m)^2}{2\Omega^2}\right]d\Delta E\,, \tag{1.22}$$

where ΔE_{m} is the mean energy loss and Ω^2 is the mean square deviation. Based on classical considerations of collisions between a charged particle such as proton or α particle and free target electrons, Ω^2 is given as

$$\Omega^2 = \Omega_B^2 = 4\pi Z_1^2 e^4 N Z_2 t\,, \tag{1.23}$$

where t is the path length in the target [7]. This expression is often referred to as the Bohr value of energy loss straggling. For estimation of the energy resolution, the full width at half maximum (FWHM) is $2(2\ln 2)^{1/2}$ times the standard deviation (Ω). Lindhard and Scharff [8] modified Eq. (1.23) to

$$\frac{\Omega^2}{\Omega_B^2} = \begin{cases} L(\chi)/2 & \chi \le 3 \\ 1 & \chi \ge 3 \end{cases} \tag{1.24}$$

considering the local electron density of the target atom, where

$$L(\chi) = 1.36\chi^{1/2} - 0.16\chi^{3/2}, \tag{1.25}$$

$\chi = (v/v_B)^2/Z_2$, v the velocity of the particle and v_B the Bohr velocity. Recently, Yang et al. [9] proposed an empirical formula for energy loss straggling, which is based on Chu's calculation [10]. This formula is well-fitted to many experimental measurements for energy loss straggling.

1.3.7 Channeling

For analysis of a surface layer which consists of atoms of lower mass than the substrate atoms, the contribution of the lighter atoms in the energy spectrum of scattered ions appears as a small peak on an intense continuous spectrum arising from the substrate atoms, because the kinematic factor and the scattering cross section for the lighter atoms are smaller than those for the substrate atoms. This results in low sensitivity and limited quantitative performance for the lighter atoms. If the substrate is single-crystal and the layer consisting of the lighter atoms is not so, however, channeling technique enables higher quantitative analysis for them. Channeling occurs when the ion beam is carefully aligned with a major symmetry direction of the single crystal. Channeled ions cannot get close enough to the atomic nuclei of the crystal to undergo large-angle Rutherford scattering. Therefore scattering from the subsurface atoms is drastically reduced by a factor of approximately 100. Consequently,

channeling improves the sensitivity for the lighter atoms in amorphous or polycrystalline surface layer.

1.4 Outline of this thesis

As described in Section 1.3.5, the depth resolution of Rutherford Backscattering spectroscopy (RBS) is limited by the energy resolution of the detector for scattered ions. The typical depth resolution of RBS using a standard solid-state detector is as large as ~10 nm. Even with grazing-angle technique, the depth resolution (~2 nm) is not enough for analysis of ultrathin films with nanometer thickness. Alternatively, the use of an electrostatic or magnetic energy analyzer makes it relatively easy to achieve higher depth resolution below 1 nm. If the depth resolution is improved to as small as 0.2 nm (typical interplanar distance in a crystalline target), a compositional analysis for each atomic layer is available.

In this thesis, so-called monolayer analysis for surfaces and interfaces of ultrathin films will be demonstrated by means of high-resolution RBS with sub-nanometer depth resolution.

Chapter 2 consists of a brief review of the high-resolution depth profiling using high-resolution RBS or ERD in both historical and instrumental aspects, and a description of our experimental setup for high-resolution RBS.

Chapter 3 demonstrates a successful monolayer analysis of the (001) and (111) surfaces of PbTe. The structures of the outermost atomic layers of both the surfaces are discussed from the experimental results of high-resolution RBS along with reflection high-energy electron diffraction (RHEED).

In chapter 4, charge fraction of 400 keV He ions scattered from three well-defined surfaces, SiO_2(2.5 nm)/Si(001), clean Si(001)(2×1), Ag/Si(001) was investigated. The dependence of the charge fraction on the kind of surface and the exit angle of ions was discussed in terms of the energy levels of electrons in the outermost tail of the surfaces. The favorable scattering geometry for highly quantitative analysis by high-resolution RBS was also proposed.

In chapter 5, intermixing of Ge and Si atoms in the initial stage of heteroepitaxy of Ge on a clean Si(001) surface was observed.

In chapter 6, initial stage of dry oxidation of Si(001) was investigated at 20–700°C in 10^{-7}–10^{-4} Torr oxygen pressure. The observed results were compared with an oxidation model proposed by a theoretical study.

In chapter 7, the growth-temperature dependence of the transition structure at the SiO_2/Si interface was observed by high-resolution RBS/channeling. The temperature dependence of the magnitude of Si lattice distortion near the interface was discussed in terms of the viscous flow of SiO_2 at high temperature.

In chapter 8, characterization of a HfO_2 (3 nm)/Si(001) interface prepared by atomic-layer chemical vapor deposition was performed with high-resolution RBS (HRBS). Strain depth profile in the interface region was measured with a combination of HRBS and channeling technique.

In chapter 9, several recent approaches to improve high-resolution RBS are briefly mentioned as closing remarks.

References

[1] V.R. Deline, W. Katz, C.A. Evans and P. Williams, Appl. Phys. Lett. 33 (1978) 832.

[2] For example, L.C. Feldman and J.W. Mayer, *Fundamentals of Surface and Thin Film Analysis* (North-Holland, Amsterdam, 1986).

[3] J. L'Ecuyer, J.A. Davies, N. Matsunami, Nucl. Instr. and Meth. 160 (1979) 337.

[4] H.H. Andersen and J.F. Ziegler, Hydrogen Stopping Powers and Ranges in All Elements (Pergamon, New York, 1977).

[5] J.F. Ziegler, Helium Stopping and Ranges in All Elements (Pergamon, New York, 1977).

[6] J.F. Ziegler, J.P. Biersack, U. Littmark, *The Stopping and Ranges of Ions in Solids* (Pergamon, New York, 1985).

[7] N. Bohr, Kgl. Danske Videnskab. Selskab. Matt-Fys. Medd. 18 (1948) No. 8.

[8] J. Lindhard, M. Scharff, Kgl. Danske Videnskab. Selskab. Matt-Fys. Medd. 27 **(**1954) No. 15.

[9] Q. Yang and D.J. O'Connor, Nucl. Instr. and Meth. B 61 (1991) 149.

[10] W.K. Chu, Phys. Rev. A 13 (1976) 2057.

Chapter 2

Experimental setups for high-resolution RBS

2.1 Brief history for monolayer analysis with RBS

Attempts for the development of high-resolution RBS using high-resolution energy analyzer have started since 1960s [1]. Bøgh et al. used a sector magnetic spectrometer with energy resolution of 1 keV and achieved a depth resolution of as small as 1 nm [2]. The energy resolution of their spectrometer would be good enough for monolayer analysis, provided they employed an appropriate geometry of grazing exit angle θ_e. However they were not successful in monolayer analysis. One of the reasons for this should be radiation damage given to the target. Because they needed to sweep the magnetic field to obtain an energy spectrum of the scattered ions, a long-time irradiation was necessary. Therefore, it is probable that the target crystal was significantly disordered due to the radiation damage, which should hamper monolayer analysis.

Monolayer analysis with high-energy ion scattering could not be achieved till the early 1990s. Vrijmoeth et al. in the FOM institute, Amsterdam (Netherlands) successfully performed monolayer analysis for the first time using a troidal electrostatic spectrometer [3]. They observed the surface of $NiSi_2(111)$ with 100 keV protons as probe ions. Figure 2.1 shows an example of the observed energy spectra obtained under the conditions of [001] blocking. The contributions of the protons scattered from Ni and Si atoms in the second atomic layer are seen as shoulders on the lower energy side of the primary peaks that correspond to Ni and Si atoms in the outermost atomic layer. The solid curve represents the

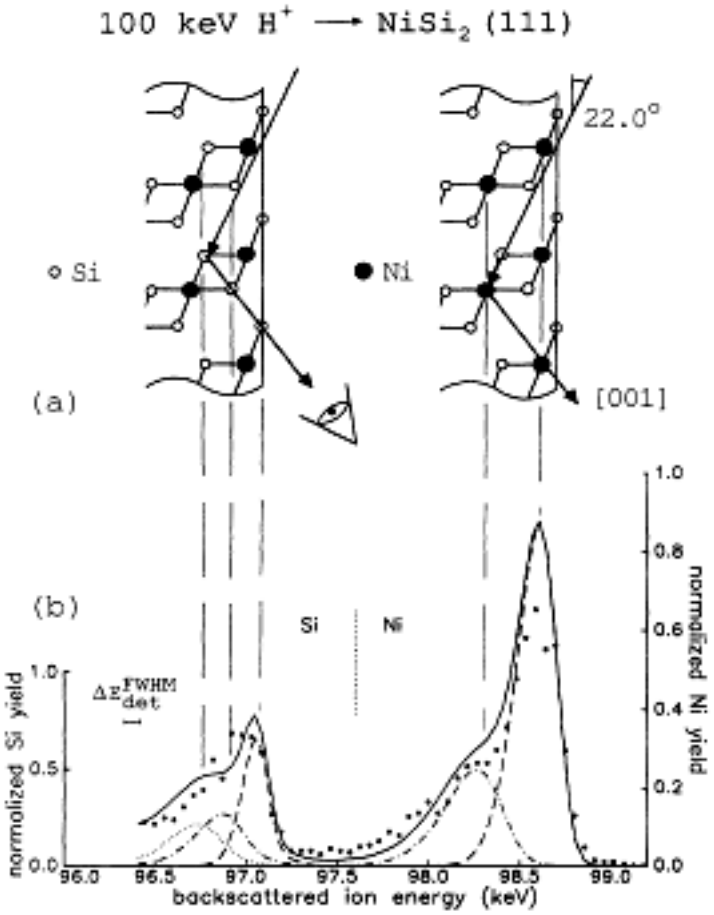

Fig. 2.1 Example of the observed energy spectra of protons backscattered from the surface of $NiSi_2(111)$ under the conditions of [001] blocking [3].

calculated spectrum with a Monte Carlo simulation and the dashed curves the calculated contribution of the individual atomic layers. The simulation reproduces the observed spectrum well, indicating that their measurements possess the potential to resolve individual atomic layers.

Their troidal spectrometer allows measuring the angular distribution of the scattered ions as well as the energy. Figure 2.2 shows their measurements for the surface structure of $NiSi_2(111)$ by means of blocking. It was found that the surface of $NiSi_2(111)$ is terminated by the Si-Ni-Si

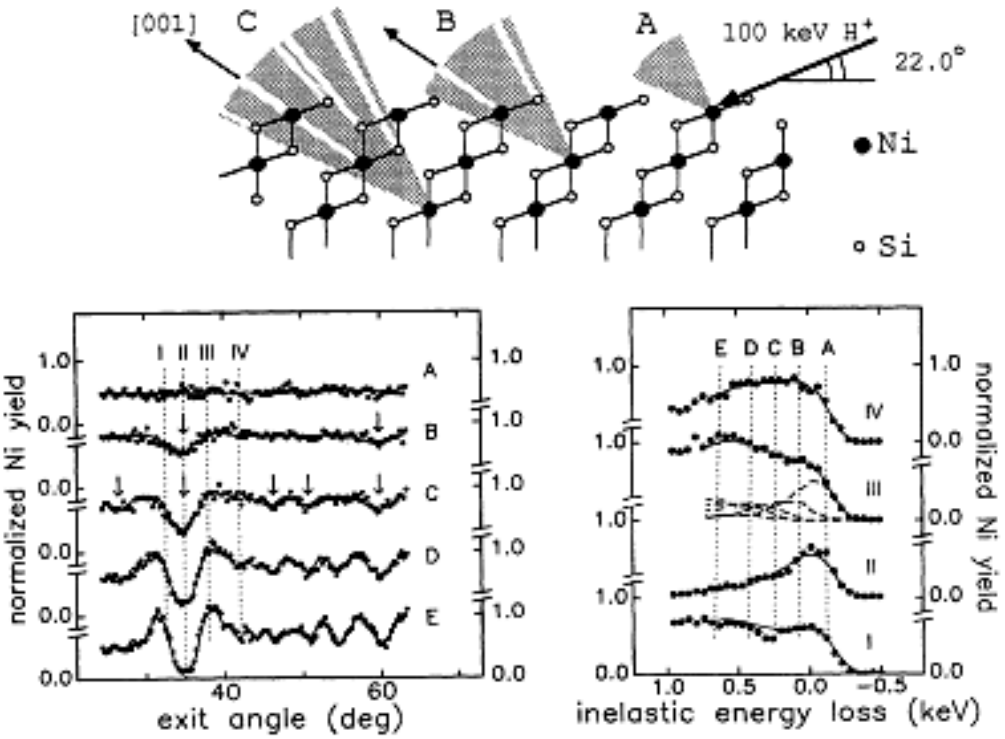

Fig. 2.2 Example of the observed energy spectra of protons backscattered from the surface of $NiSi_2(111)$ under the conditions of [001] blocking [3].

trilayer and that the distance between the outermost Si layer and the adjacent Ni layer is larger by 0.019 nm than the bulk interlayer distance.

Thus, Vrijmoeth et al. were able to resolve the contributions from the individual atomic layers using the blocking technique. However, they were not able to do under the random conditions (see spectra of I and IV in Fig. 2.2).

In the next year, Kimura et al. in Kyoto University demonstrated that they were able to resolve the contributions from the individual atomic layers even under the random conditions by the combination of a sector magnetic spectrometer and grazing-angle technique [4]. Their spectrometer

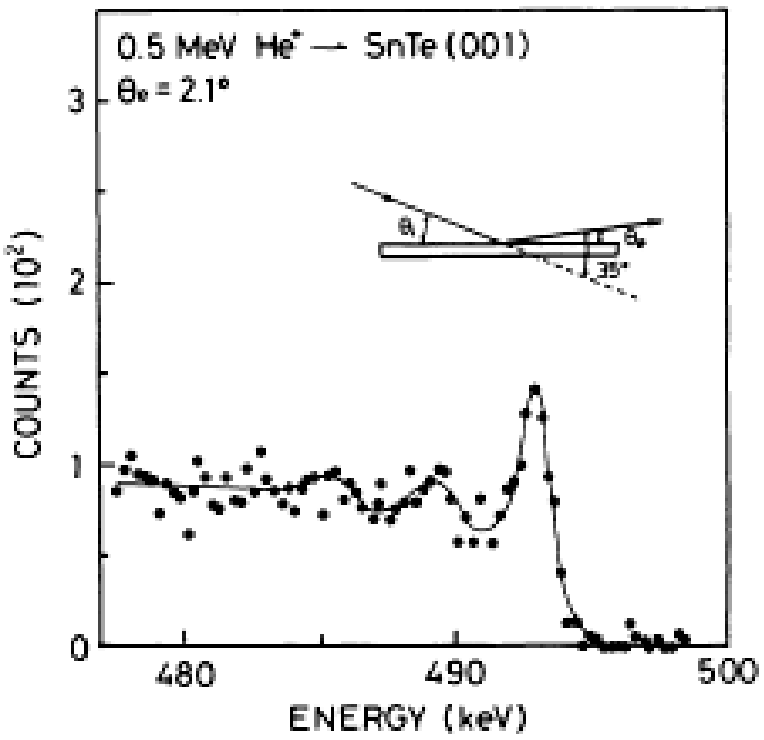

Fig. 2.3 Example of the observed energy spectra of protons backscattered from the surface of $NiSi_2$(111) under the conditions of [001] blocking [4].

was a double-focusing 90° sector magnetic spectrometer (energy resolution $\Delta E/E$ = 0.1%) that equipped a position-sensitive detector placed on the focal plane. They observed the surface of SnTe(001) using 0.5 MeV He^+ ions as probe. Figure 2.3 shows the observed energy spectrum of the scattered ions emerging at grazing exit angle of 2.1° (scattering angle was 35°). There are several peaks at equal spaces in the spectrum. These peaks correspond to Sn and Te atoms in the individual atomic layers. It is noted that Sn and Te atoms in the identical atomic layer contribute to a single peak since the kinematic factors for Sn and Te are approximately same under the scattering conditions.

Following the successes above, several other groups have reported

high-resolution depth profiling by high-energy ion scattering [5-12] using various energy spectrometers. In the next section, the works done by these groups are reviewed with particular emphasis on their spectrometers and the achieved resolution.

2.2 Spectrometers used for high-resolution RBS or ERD

Carstanjen et al. used an electrostatic spectrometer for high-resolution RBS and high-resolution ERD [5-7]. The spectrometer consists essentially of three parts: the lens system, the electrostatic analyzer, and the detecting device. It can be used for energies up to 2 MeV of singly charged particles. Figure 2.4 is a schematic drawing of the spectrometer and the scattering chamber. The lens system consists of four electrostatic quadrupole lenses and one hexapole. The quadrupole lenses are used to focus particles emitted from the sample onto the entrance slit of the analyzer. The hexapole correct for curved imaging of the slit by the analyzer. The typical acceptance angle is 0.15 msr for 1 mm entrance slit.

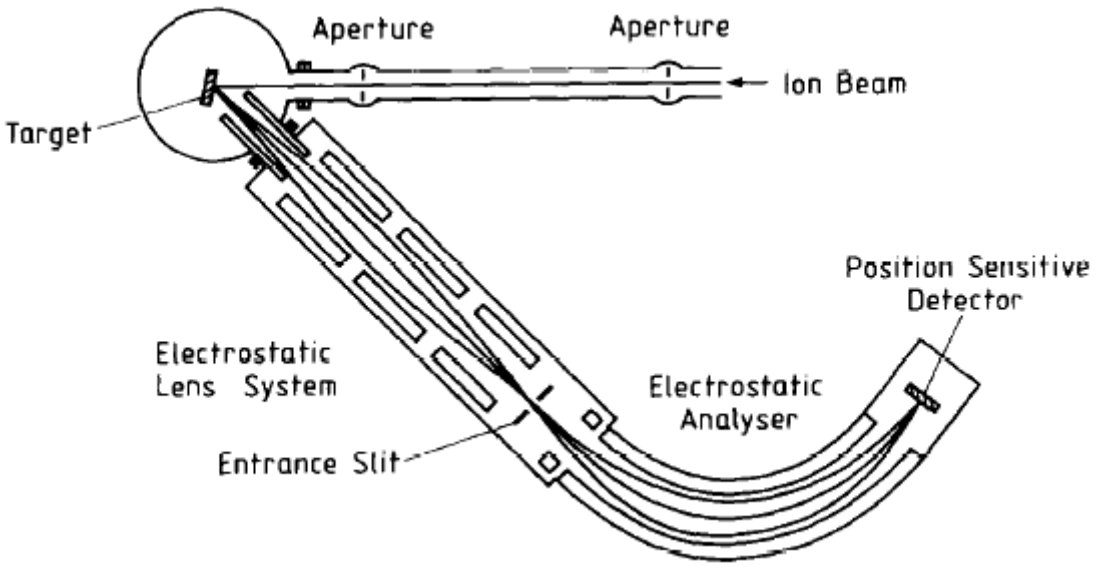

Fig. 2.4 Schematic drawing of the spectrometer and the scattering chamber used for high-resolution RBS and high-resolution ERD [5].

The analyzer is a 100° cylindrical condenser of 700 mm radius and 19.8 mm gap width. The simultaneously available energy window is 2.8% of the analyzed energy. The energy resolution of the instrument is better than 0.03%. For the detection of the particle, one-dimensional position sensitive silicon-surface barrier detectors are used. The dimension of the detector is typically 30 mm length. The spatial resolution, which is expected to be proportional to the total length, for 1 MeV He^+ ions is about 1.65 mm. When very high resolution is required, a 10 mm long detector is used. With this setup energy resolutions of 1.9 keV was achieved.

Dollinger et al. have improved the depth resolution of ERD by using a Q3D magnetic spectrograph [8] at the Munich tandem accelerator [9,10]. The Q3D magnetic spectrograph consists of one quadrupole and three dipoles, as shown in Fig. 2.5. The designed energy resolution is 0.02% and the maximum bending power, mE/q^2 = 140 MeV·amu/e^2. The solid angle of detection is changeable up to 14.7 msr, but the typical solid angle is up to 5 msr for high depth resolution. A 1 m long position-sensitive ΔE–E gas detector is used as a focal plane detector. They reported that the energy resolution of about 0.07% could be achieved in ERD for the surface of a bulk graphite monocrystal using 60 MeV ^{58}Ni ions even at a large solid angle of 5 msr [9]. This energy resolution corresponds to a carbon thickness of 0.34 nm for a given geometry. In 1998, They demonstrated the resolution of single (002) graphite layers of a highly oriented pyrolythic graphite (HOPG) sample by analyzing the $^{12}C^{5+}$ ions recoiled by 60 MeV $^{127}I^{23+}$ ions [10].

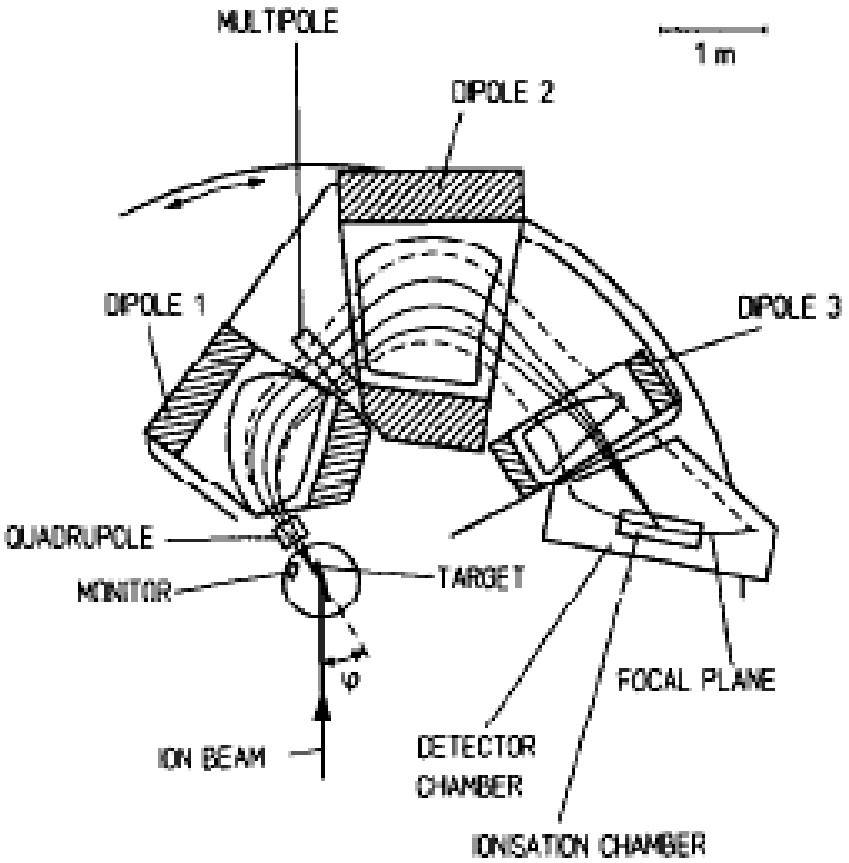

Fig. 2.5 Schematic drawing of the Q3D magnetic spectrograph used in high-resolution ERD [9].

Arnoldbik et al. have described a magnetic spectrograph which was designed for high-resolution RBS and ERD (Fig. 2.6) [11]. The spectrometer consists of a quadrupole lens, a Wien filter and a 90° dipole magnet with field correction The bending radius of the magnet is 0.5 m and the magnetic rigidity is 0.5 T·m (the maximum bending power, mE/q^2 = 12 MeV·amu/e^2) . Double focusing, energy-to-point focusing in the horizontal (energy dispersive) plane and angle-to point focusing in the vertical plane is realized. In the focal plane a two-dimensional position-sensitive detector is used to resolve an area of 70 mm (horizontal) × 50 mm (vertical) with a

resolution of 0.25 × 0.25 mm^2. The horizontal interval corresponds to an energy bin with a width of 13% of the analyzed energy. The vertical interval corresponds to an angular range of 5°. The opening angle of the spectrograph in the energy dispersive direction is determined by slits and can be chosen between 0.1° and 0.3°. The maximum angular acceptance is 0.5 msr. The spectrograph can be rotated together with a scattering chamber along a circular rail (radius 2.5 m) to change scattering geometry. The designed energy resolution is 0.04%. In a RBS measurement of an Au surface using 2.135 MeV He^+ ions, they demonstrated an energy resolution of 0.09% including the energy spread of the He ions delivered by the tandem accelerator. The scattering angle was 70° and the angle of incidence was 35° with respect to the surface. The energy resolution can be translated into a depth resolution of 0.6 nm at the surface.

Lanford et al. developed a compact magnetic spectrometer for high-resolution He RBS and other types of ion beam analysis, shown in Fig. 2.7 [12]. The outside dimensions of the spectrometer are 0.86 m by 0.58 m, including a scattering chamber. For RBS incident ions enter the spectrometer through the 160° or 180° port and bombard the target in the center of the scattering chamber. Ions scattered from the target are analyzed by two dipole magnets and are focused along the focal plane of the spectrometer. This spectrometer has the Maximum bending power, mE/q^2 = 5 MeV·amu/e^2. The detection solid angle is changeable up to 3.7 msr. The designed energy resolution is $\Delta E/E$ = 0.05% for a 2 msr solid angle. The range of ion energy (with fixed magnetic field) focused along the focal

plane is as wide as 88% of E_{max}, although the development of a long focal plane detector was failed. They tested the energy resolution by measurement of α-particles from the $^{15}N(p,\alpha)^{12}C$ reaction with a short silicon position sensitive detector (PSD) of 10 mm length. The measured energy resolution was 2.15 keV at 3940 keV (0.055%), which includes contributions from the position resolution of the focal plane detector, the finite width of the beam spot on target, any surface contamination or oxidation effects of the target and beam energy spread.

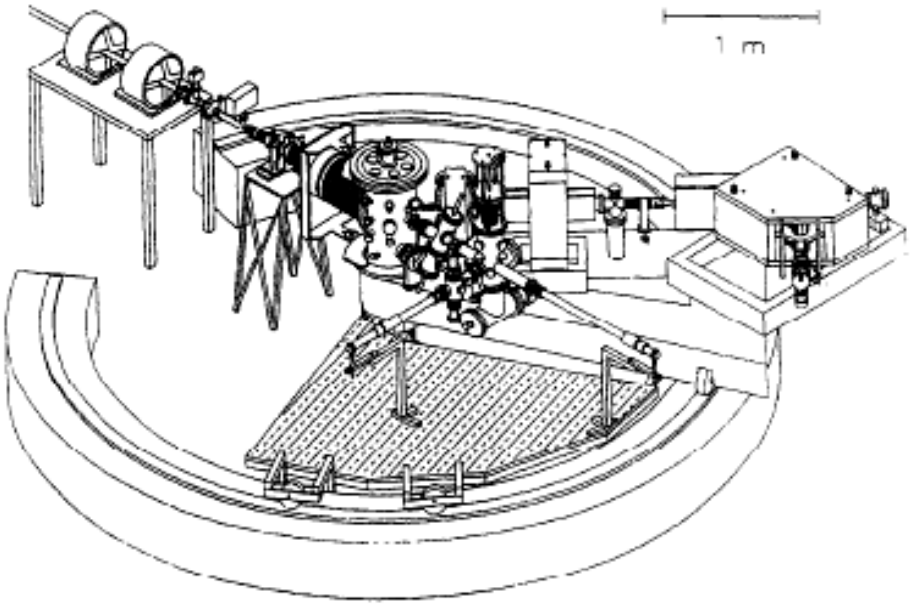

Fig. 2.6 Schematic drawing of the magnetic spectrograph designed for high-resolution RBS and ERD [11].

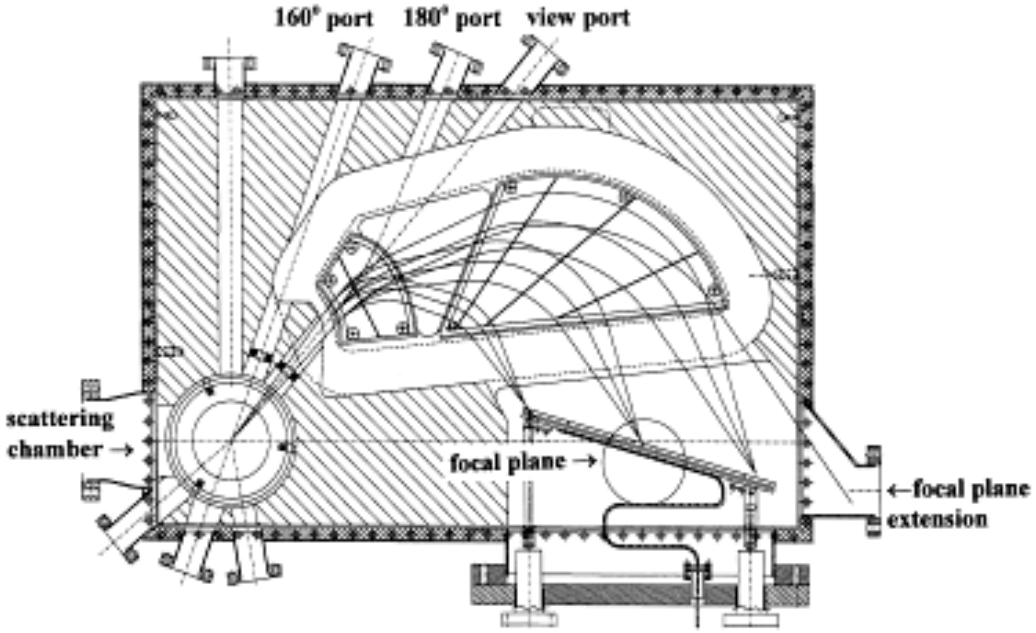

Fig. 2.7 Schematic drawing of the compact magnetic spectrometer developed for high-resolution He RBS and other types of ion beam analysis. The outside dimensions of the spectrometer are 0.86 m by 0.58 m, including a scattering chamber [12].

2.3 Setup of HRBS system at Kyoto University

The Setup of HRBS system used in this work will be described in this section. The setup has been modified in various points from the initial one that was used for the study in Chapter 3, so only the present system will be described here.

The HRBS system includes a 400 keV Cockcroft-type accelerator, an ultrahigh vacuum (UHV) scattering chamber, a magnetic spectrometer, a one-dimensional position-sensitive detector (1D-PSD), and electronic modules for signal processing and data acquisition. The schematic of the system without electronics is shown in Fig. 2.8.

The 400 keV Cockcroft-type accelerator was built by Kobe Steel Co. This accelerator has a PIG type ion source and an acceleration tube in an isolation tank of diameter 0.6 m and height 1.5 m which is filled with SF_6 gas (> 5 atm). He^+ ion beam generated by the accelerator with energy of 400 keV is mass analyzed with a switching magnet and transported into the beam line connecting to the UHV scattering chamber. The ion beam is collimated to 2×2 mm^2 in size and less than ±0.1° in divergence angle by two sets of four-jaw slits separated by 1.2 m in the beam line. The beam intensity is highly stable and the typical beam current is 50 nA.

The UHV scattering chamber is pumped by a series of turbo molecular pumps (and a sputter ion pump) and the base pressure is 1×10^{-10} Torr after an adequate bake-out for 1 or 2 days. The chamber is connected to the beam line via a differential pumping system and is equipped with a

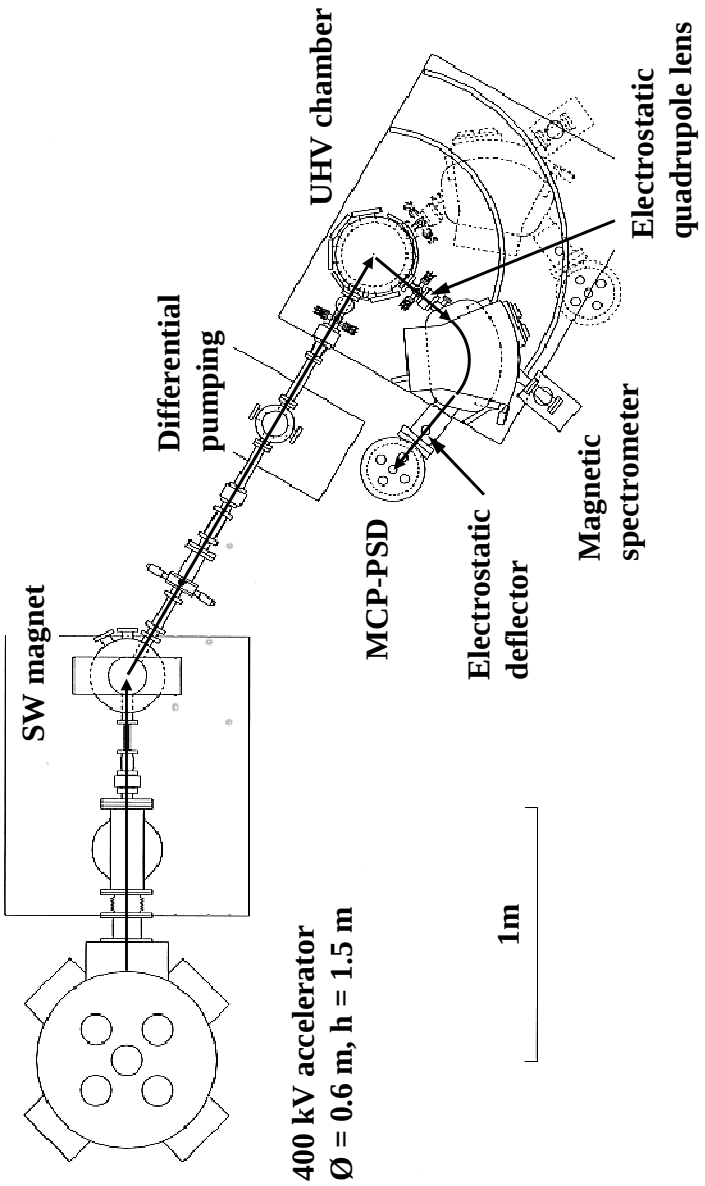

Fig. 2.8 Schematic drawing of the Kyoto Univ. HRBS system

five-axis high precision goniometer, a reflection high-energy electron diffraction (RHEED) gun, an evaporator using tungsten helical filaments and/or an UHV electron-beam evaporator. Specimens are mounted on the goniometer in the UHV scattering chamber. Two different sample holders were used depending on the specimens and the required thermal treatment. One is for the experiments that demand a clean surface of Si. This holder clips both the ends of a strip Si specimen by electrodes and so allows

heating the specimen by direct current up to 1200°C. The other is for the specimens that need only low-temperature treatment up to 300°C. The scattering chamber has four connecting ports (25°, 50°, 75°, 100° form the direction of the incident ion beam) to which the magnetic spectrometer can be connected, allowing us to select the detecting scattering angle depending on the specimen and what is demanded in the analysis. Ions scattered from the specimen are energy analyzed by the magnetic spectrometer and detected by a 1D-PSD placed on the focal plane of the spectrometer.

The spectrometer is basically a standard 90° sector magnetic spectrometer with 26.6° inclined boundaries for double focusing. The exit boundary is modified in the shape of an arc so that the focal plane is perpendicular to the optical axis [13]. The bending radius of the spectrometer is 200 mm and the maximum bending power (mE/q^2) is 1.75 MeV·amu/e^2. The acceptance angle is variable up to 0.4 msr. The 1D-PSD of length 100 nm and width 15 mm consists of microchannel plates and a resistive anode. The Combination of the spectrometer and the detector allows measuring an energy spectrum over the energy window of 25% of the central energy without sweeping the magnetic field. The energy resolution of the spectrometer is designed to be less than 0.1% (0.4 keV at 400 keV) at an acceptance angle of 0.4 msr. In addition, the spectrometer has an electrostatic quadrupole lens (Q-lens) just before the entrance of the sector magnet and an electrostatic deflector between the magnet and the 1D-PSD. The Q-lens is used for the correction of the kinematic broadening, so that high depth resolution is achieved even for light elements. The

electrostatic deflector, which can deflect the ions vertically (perpendicular to the bending plane of the spectrometer), is for reduction of background noise in the observed spectra, operated in conjunction with the vertical displacement of the 1D-PSD to the off-center position.

The schematic of signal processing system to determine where the ions hit on the detector is shown along with the 1D-PSD in Fig. 2.9. In this system, the position where an ion is detected is determined by comparing the pulse heights of the signals generated on both ends of the resistive anode. Then one can convert the position distribution to the energy spectrum using an experimentally-obtained conversion function.

In this HRBS system several hundreds keV He^+ ions are used as probe projectiles. This is because use of several hundreds keV He^+ ions

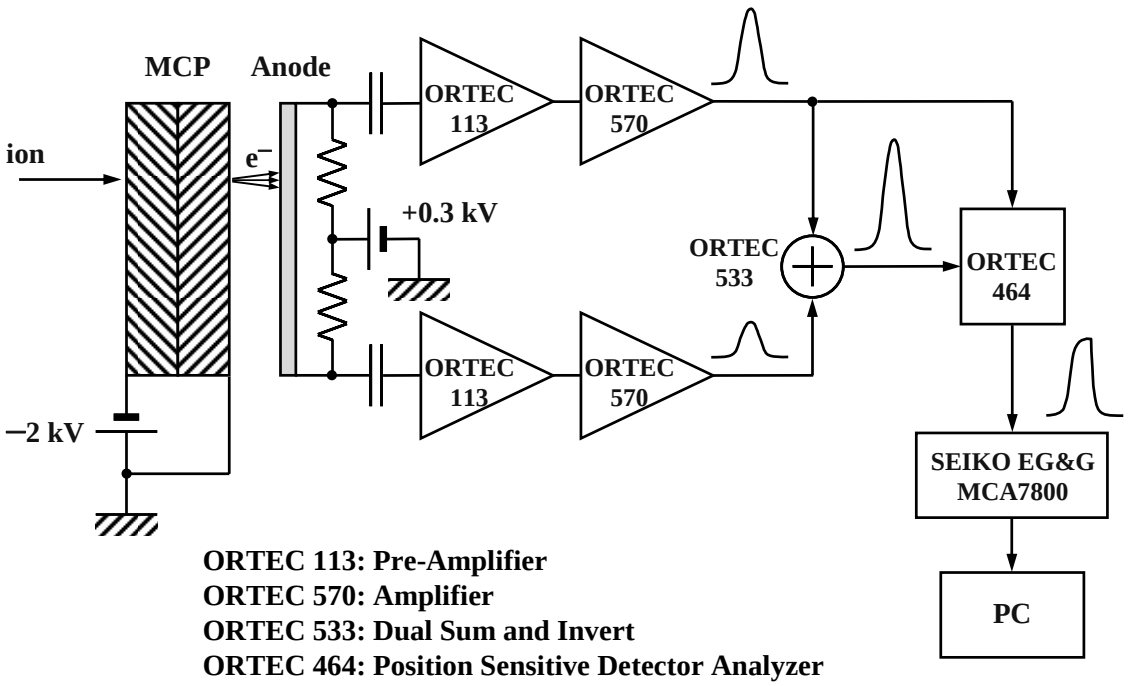

Fig. 2.9 The signal processing system employed for 1D-PSD in the HRBS system.

gives some advantages to the analysis by HRBS owing to the following. (a) Stopping power of many elements for He ions has a maximum at energy of several hundreds keV as shown in Fig. 2.10, so the best depth resolution can be achieved by using He ions in this energy region. (b) Equilibrium charge-state fraction of He^+ after penetrating a carbon foil is high and almost constant at the energy region of 200–400 keV as seen in Fig. 2.11 [14], indicating that reliable composition can be derived by detection of scattered He^+ only. (c) Relatively large cross section enables us to acquire a HRBS spectrum in a short time, typically 10 minutes despite the small acceptance angle of the spectrometer.

Figure 2.12 shows HRBS spectra for SiO_2/Si(001) for incidence of

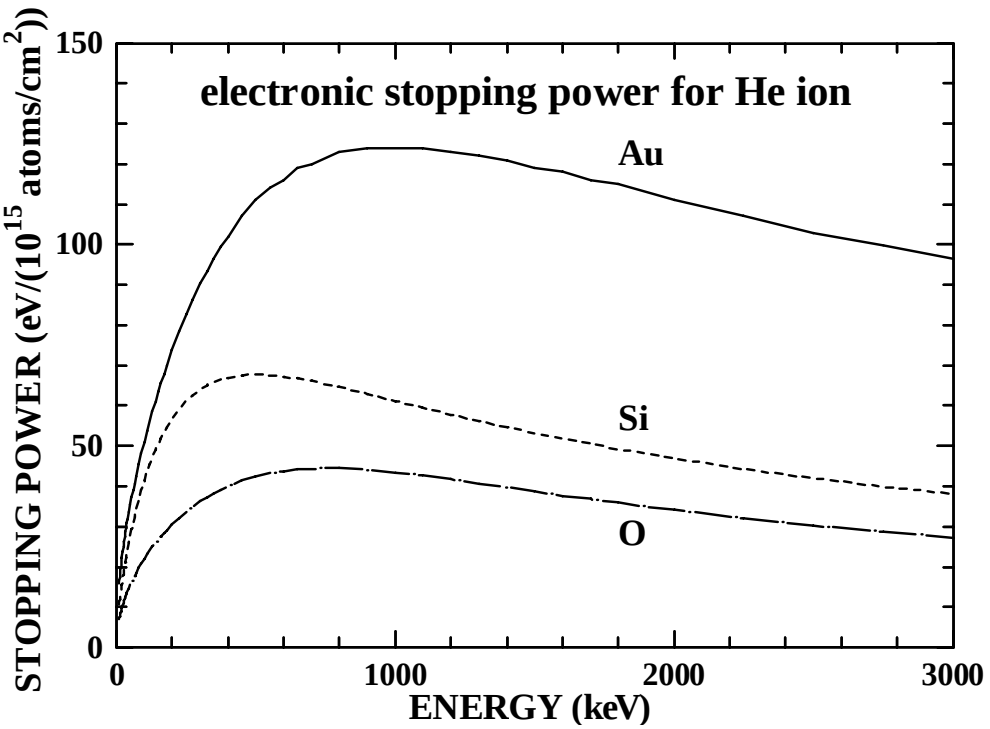

Fig. 2.10. Electronic stopping cross section of various elements as a function of energy of projectile He ions.

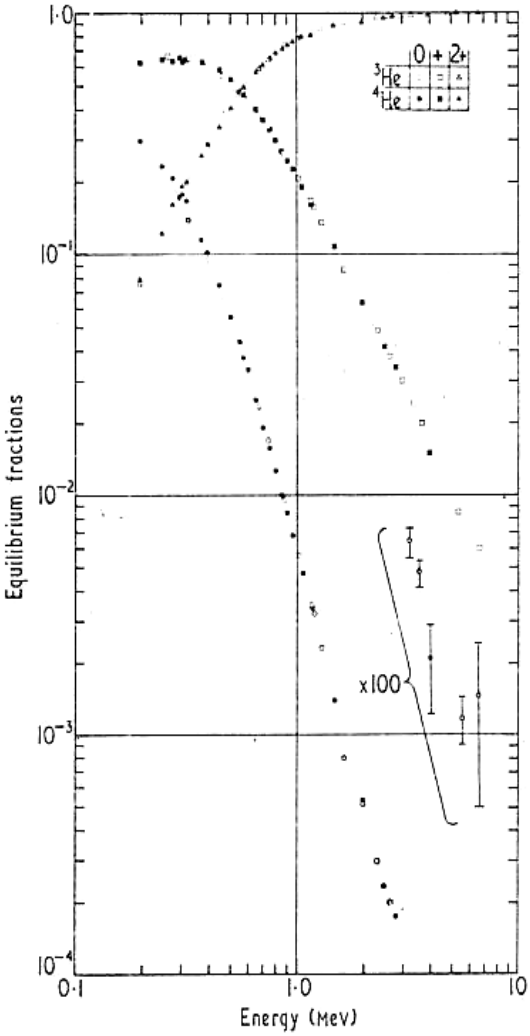

Fig. 2.11 Equllbrium charge-state fractions for helium ions in carbon [14].

350 keV He^+ ions under the [110] channeling condition without Q-lens (a), and with Q-lens (b) [15]. The scattering angle was 50° and the exit angle was 5° from the surface plane. The leading edge of the oxygen peak becomes as sharp as ~0.4 keV (0.1%) in width when the Q-lens is operating. The estimated depth resolution is ~0.1 nm at the surface under operation of the Q-lens, while the resolution without the Q-lens is ~0.3 nm. These spectra indicate that our HRBS system provides an analysis with

monolayar depth resolution and that correction of the kinematic broadening by the Q-lens is important for high resolution analysis of relatively light elements.

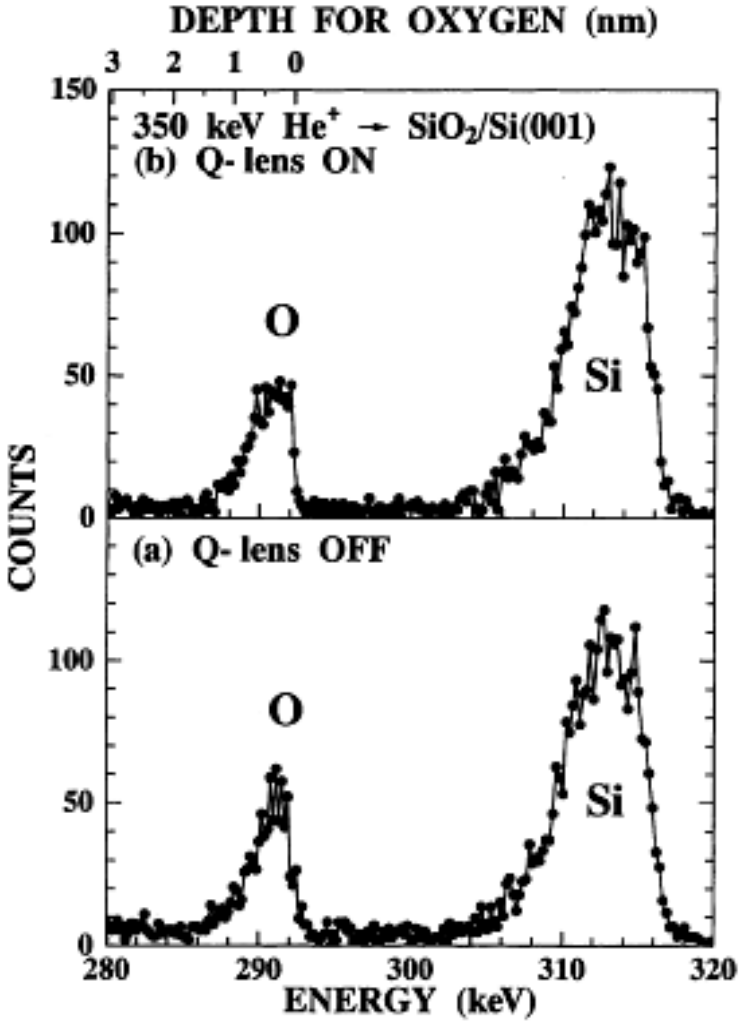

Fig. 2.12 HRBS spectra for SiO_2/Si(001) under the [110] channeling (a) without Q-lens (a), and with Q-lens (b).

References

[1] E. Bøgh, Phys. Rev. Lett. 19 (1967) 61.

[2] E. Bøgh, *Channeling* (ed. by D.V. Morgan, John Wiley & Sons, London, 1973) Ch. XV.

[3] J. Vrijmoeth, P.M. Zagwijn, J.W.M. Frenken, J.F. van der Veen, Phys. Rev. Lett. 67 (1991) 1134.

[4] K. Kimura, H. Ohtsuka, M. Mannami, Phys. Rev. Lett. 68 (1992) 3797.

[5] Th. Enders, M. Rilli, H.D. Carstanjen, Nucl. Instr. and Meth. B 64 (1992) 817.

[6] O. Kruse, H.D. Carstanjen, Nucl. Instr. and Meth. B 89 (1994) 191.

[7] H.D. Carstenjen, Nucl. Instr. and Meth. B 136-138 (1998) 1183.

[8] M. Löffler, H.J. Scheerer, H. Vonach, Nucl. Instr. and Meth. 111 (1973) 1.

[9] G. Dollinger, Nucl. Instr. and Meth. B 79 (1993) 513.

[10] G. Dollinger, C.M. Frey, A. Bergmaier, T. Faestermann, Nucl. Instr. and Meth. B 136-138 (1998) 603.

[11] W.M. Arnoldbik, W. Wolfswinkel, D.K. Inia, V.C.G. Verleun, S. Lobner, J.A. Reinders, F. Labohm, D.O. Boerma, Nucl. Instr. and Meth. B 118 (1996) 566.

[12] W.A. Lanford, S.Bedell, S. Amadon, A. Haberl, W. Skala, B. Hjorvarsson, Nucl. Instr. and Meth. B 161-163 (2000) 202.

[13] K. Kimura, M. Kimura, Y. Mori, M. Maehara, H. Fukuyama, in: J.L. Duggan, I.L. Morgan (Eds.), Application of Accelerators in Research

and Industry, American Institute of Physics, New York, 1999, p. 500.

[14] J.C. Armstrong, J.V. Mullendore, W.R. Harris, J.B. Marion, Proc. Phys. Soc. 86 (1965) 1283.

[15] K. Kimura, K. Nakajima, Y. Okazaki, Nucl. Instr. and Meth. B 183 (2001) 166.

Chapter 3

The (111) surface of PbTe observed by high-resolution RBS

The (001) and (111) surfaces of PbTe have been observed by high-resolution Rutherford backscattering spectroscopy (HRBS) and reflection high-energy electron diffraction (RHEED). The observed HRBS spectra for the incidence of 300–350 keV He^+ ions show several peaks corresponding to individual atomic layers, allowing direct determination of atomic concentrations for each layer. Whereas the (001) surface is stoichiometric up to the topmost atomic layer, the (111) surface is terminated by the Pb layer and the density of the topmost Pb layer is about 30% of the bulk density.

3.1 Introduction

Since the introduction and development of ultra-high-vacuum techniques in the early 1960s, solid surfaces have been subject to extensive studies. In addition to old techniques such as low energy electron diffraction and field emission microscopy, a number of new techniques have been introduced and exploited to study surfaces at the atomic level [1]. Among these techniques, Rutherford backscattering spectroscopy (RBS) is a unique technique. It allows quantitative and non-destructive analysis with a reasonable depth resolution, which is typically 10 nm. Recently, we have demonstrated that monolayer resolution can be achieved in RBS using both a high-resolution spectrometer and a grazing-angle technique [2]. This new technique, called high-resolution RBS (HRBS), realizes quantitative layer-by-layer analysis without destruction of specimens. In this chapter, we demonstrate the potential of HRBS in the study of surfaces. The (001) and (111) surfaces of PbTe are observed by HRBS. The surface reconstructions of these surfaces are discussed in combination with the observation of reflection high-energy electron diffraction (RHEED).

3.2 Experimental

The (001) and (111) surfaces of PbTe were prepared in situ by vacuum evaporation of pure PbTe (purity 99.999%) on substrate crystals in a UHV chamber (base pressure 3×10^{-10} Torr), which was connected to a 4 MV Van de Graaff accelerator via a differential pumping system. The PbTe(001) was grown at 500 K on a SnTe(001) surface, which was prepared by vacuum evaporation on a cleaved (001) surface of KCl. A well-defined 1×1 pattern was observed by RHEED, indicating that there was no surface reconstruction except for a possible rumpling reconstruction where the surface cations (anions) move inward (outward). The PbTe(111) surface was grown on a cleaved (111) surface of BaF_2 at 520 K. RHEED intensity oscillations were observed during the growth, showing that the crystal grows layer by layer [3]. The period of the oscillations corresponds to the growth time of one molecular layer of PbTe. This is consistent with the fact that PbTe is evaporated in a molecular form [4]. The surface showed a weak two-fold reconstruction pattern in the <110> direction by RHEED.

Beams of 300–350 keV He^+ ions from the accelerator were collimated to 2.5 mm × 2.5 mm and a divergence angle less than 2 mrad by a series of apertures. The typical beam current was 10–20 nA. The azimuth angle of incidence of the ion beam was carefully chosen to avoid the channeling/blocking effects. The ions scattered at 100° were energy analyzed by a 90° sector magnetic spectrometer. The radius of the

spectrometer was 300 mm and the dispersion was 1200 mm. The dispersion means the displacement of detecting position of an analyzed ion at the exit focal plane per unit change in the momentum. The magnet yoke had inclined boundaries (26.6°) for two-dimensional focusing. The acceptance solid angle of the spectrometer was variable up to 0.2 msr and the present measurements were done at the acceptance angle of 0.05 msr. The energy window of the spectrometer was 9% and the energy resolution was about 0.1% including the energy spread of the incident beam.

3.3 Results and discussion

3.3.1 (001) surface

An example of the HRBS spectrum for the PbTe(001) is shown in Fig. 3.1. The exit angle, θ_e = 2.6°, was measured from the surface plane. The spectrum shows several well-defined peaks at 285.5, 283.3, 281.1 and 277.8 keV, suggesting that these peaks correspond to the Pb atoms in the first, second and third atomic layers and the Te atoms in the first atomic layer, respectively. The energy difference of the ions scattered from the same kind of atoms in the adjacent layers is written as

$$\Delta E = Sd_p\left(\frac{k}{\sin\theta_i}+\frac{1}{\sin\theta_e}\right), \tag{3.1}$$

where S is the stopping power, d_p the interplanar distance, k the kinematic factor for ion–atom scattering (0.956 for the present He–Pb case) and θ_i is the incident angle measured from the surface plane. The energy difference ΔE at θ_e = 2.6° is calculated to be 2.4 keV using $d_p = a_0/2$ = 0.3231 nm and a stopping power given in the literature [5]. The observed energy difference between the adjacent peaks (~2.2 keV) agrees with the calculated value within the experimental error, indicating that the observed peaks correspond to the successive atomic layers.

The inelastic energy loss of the scattered ion is a measure of the depth where the ion is scattered from. Fig. 3.2 shows the inelastic energy losses for the observed peaks as a function of the exit angles. In the

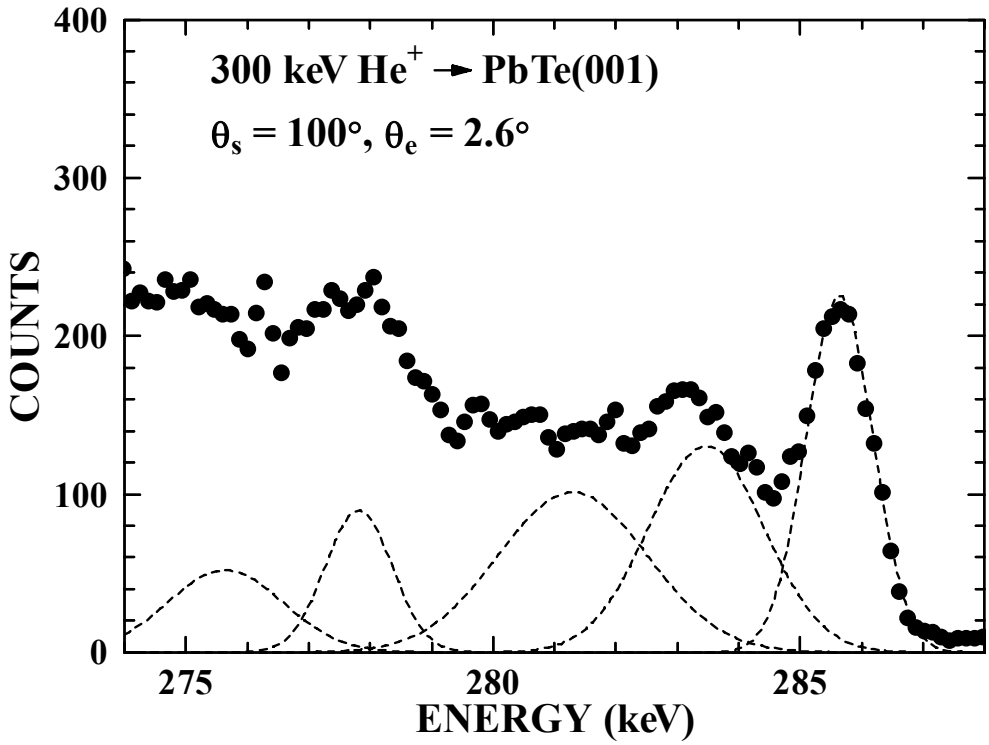

Fig. 3.1 Energy spectrum of 300 keV He^+ ions scattered at 100° from PbTe(001) at the exit angle θ_e = 2.6° measured from the surface plane. The contributions from the successive atomic layers (1st–3rd layers for Pb and 1st–2nd layers for Te) are resolved as separated peaks.

estimation of the inelastic energy loss, the energies of the leading edges in the HRBS spectrum observed at a large exit angle (see Fig. 3.3) were considered as the energies of the ions elastically scattered from Pb and Te atoms. The experimental error is mainly due to the fluctuation of the incident ion energy and the uncertainty in the determination of the peak position. The energy losses for the first Pb layer and for the first Te layer are the same within the experimental error, showing that the first layer contains both Pb and Te atoms and the rumpling reconstruction is small if existent. The yield of the first Te peak is about 40% of that of the first Pb peak. This yield ratio agrees with the cross-section ratio, $(52/82)^2$,

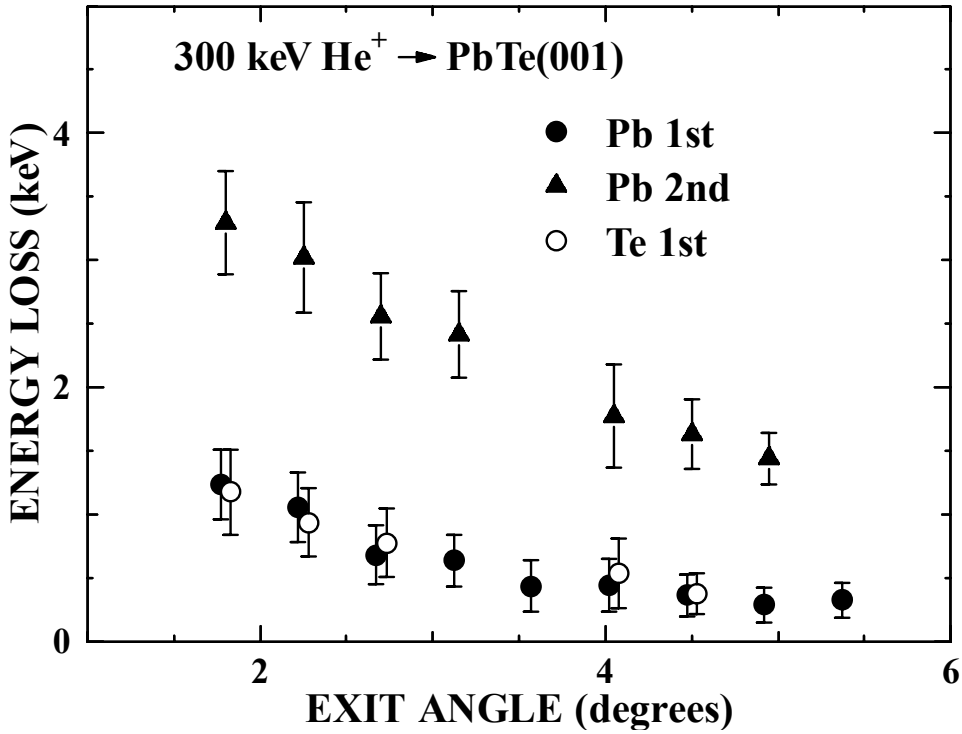

Fig. 3.2 Inelastic energy loss of the ions scattered from each atomic layer for PbTe(001). The energy loss for the first Pb peak agrees with that for the first Te peak, indicating that the topmost layer has both Pb and Te atoms.

indicating that the atomic densities of Pb and Te are the same as expected from the NaCl-type structure even in the first atomic layer.

3.3.2 (111) surface

Examples of the observed energy spectra of the scattered He^+ ions from the PbTe(111) at various exit angles are shown in Fig. 3.3. The spectrum shows a multipeak structure at a grazing exit angle as is similar to Fig. 3.1. For example, there are several peaks at 333.8, 331.9,329.3 and 323.5 keV in the spectrum at θ_e = 3.0°, which correspond to Pb atoms in the first, second and third layers and Te atoms in the first layer,

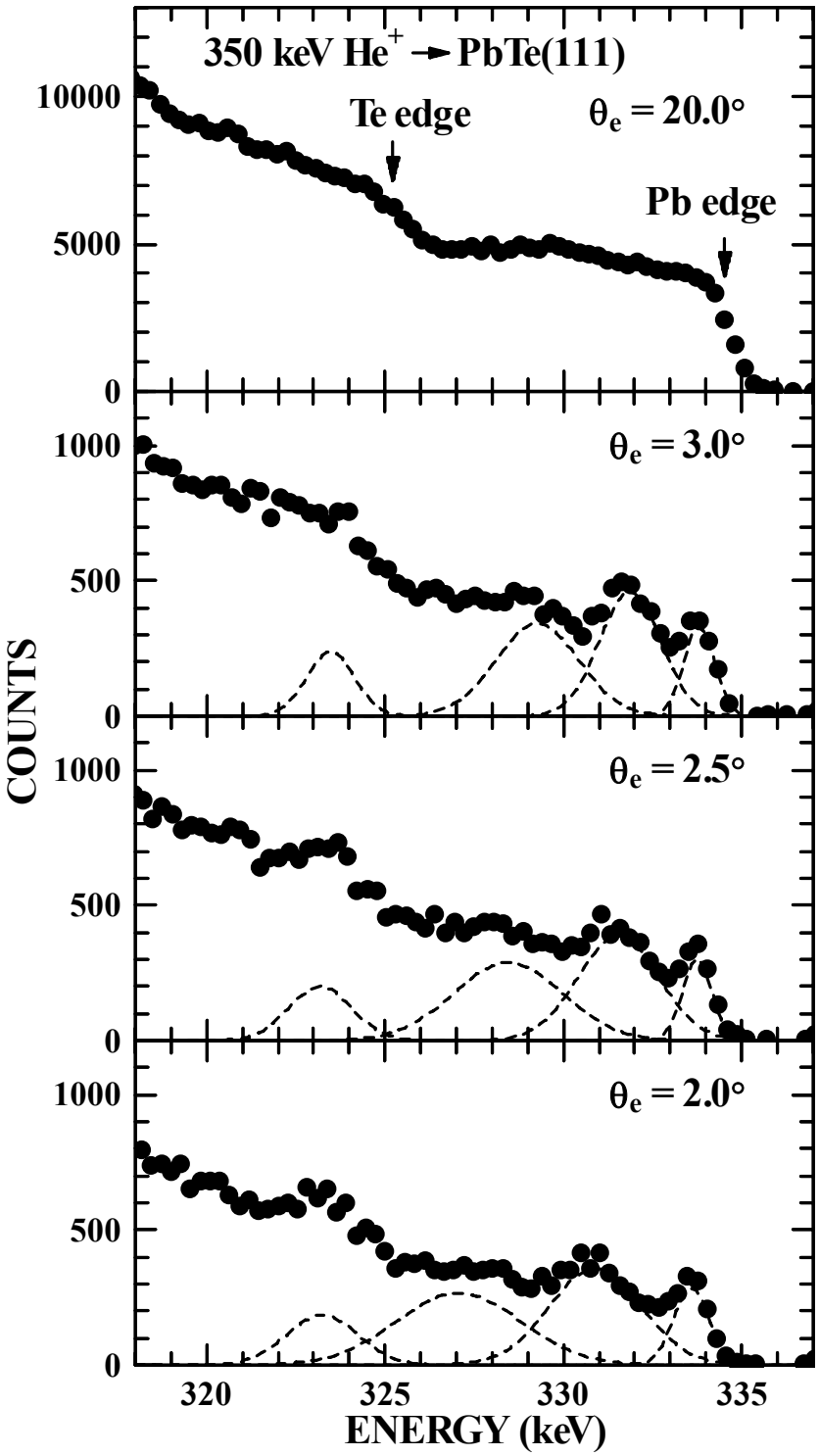

Fig. 3.3 Energy spectra of 350 keV He^+ ions scattered at 100° from PbTe(111) at various exit angles. The exit angle θ_e is measured from the surface plane. The spectra at grazing exit angles show several peaks corresponding to successive atomic layers. The peak spacing correspond to the interplanar distance between adjacent molecular layers, $a_0/\sqrt{3}$.

respectively. The energy difference ΔE at θ_e = 3.0° is calculated to be 2.6 keV using $d_p = a_0/\sqrt{3}$ = 0.373 nm (interplanar distance between adjacent molecular layers). The observed energy difference between the adjacent peaks agrees well with the calculated value except for that between the first and second Pb peaks (1.9 keV). The anomaly of the peak spacing between the first and second Pb peaks will be discussed later.

The PbTe crystal with a NaCl-type structure has a stacking sequence of Pb and Te layers parallel to (111). If the Pb and Te layers coexist at the surface, the peak spacing must correspond to the distance between adjacent atomic layers ($a_0/2\sqrt{3}$) instead of that between adjacent molecular layers ($a_0/\sqrt{3}$). The fact that the observed peak spacing corresponds to the interplanar distance between adjacent molecular layers indicates that the topmost atomic layer has only one species. In order to determine whether the topmost atomic layer is a Pb layer or a Te layer, we estimate the inelastic energy loss of ions scattered from each atomic layer from the observed spectra. The estimated inelastic energy losses of the ions scattered from successive atomic layers are shown in Fig. 3.4. The energy loss for the first Pb peak is always smaller than that for the first Te peak. This clearly indicates that the topmost atomic layer is a Pb layer.

The yields of Pb peaks are almost the same except for the Pb first peak, as is seen in Fig. 3.3. In addition, the observed yields of Te peaks are about 40% of that of Pb peaks for the subsurface Pb layers, which agrees with the ratio of Rutherford cross-sections, $(52/82)^2$. These results indicate that the PbTe crystal is stoichiometric except for the first Pb layer. The

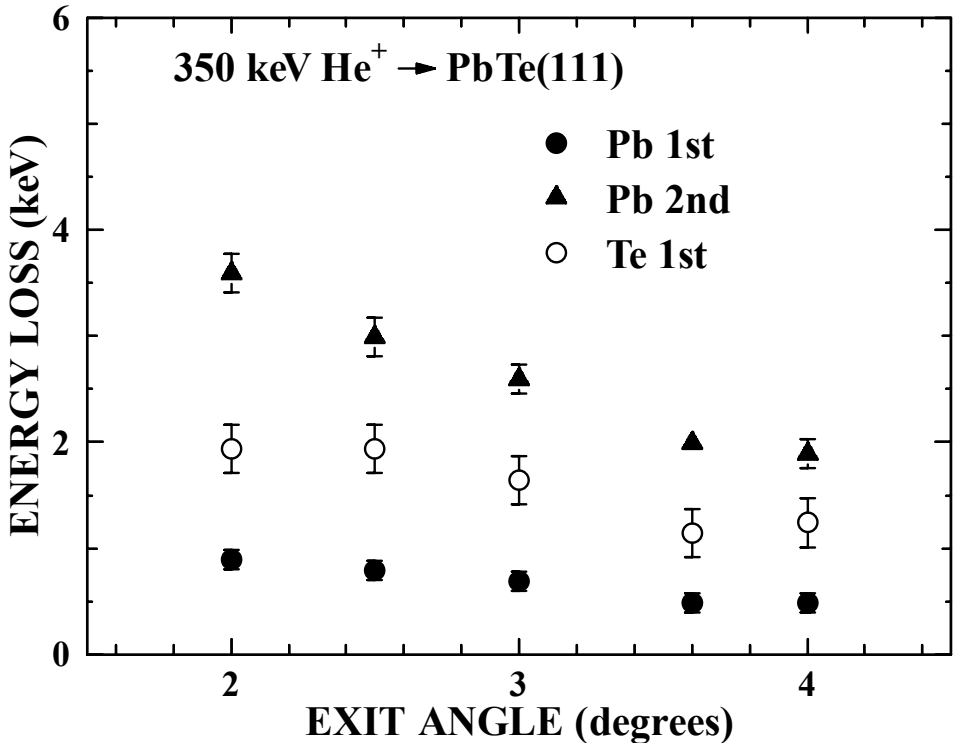

Fig. 3.4 Inelastic energy loss of the ions scattered from each atomic layer for PbTe(111). The energy loss for the first Pb peak is always smaller than that for the first Te peak, showing that the topmost atomic layer is a Pb layer.

yield of the first Pb peak is about 30% of the second Pb peak yield. This cannot be attributed to the channeling/blocking effects but to the reduction of atomic density in the topmost Pb layer, because the reduction of the first Pb yield is observed at various exit angles ranging from 2° to 4°. The anomalous peak spacing between the first and the second Pb peaks mentioned above is related to the reduction of the atomic density of the topmost Pb layer. The energy difference between the *i*th Pb peak and the (*i*+1)th Pb peak is written as

$$\Delta E_{i,i+1}^{Pb} = \left(\frac{k}{\sin\theta_i} + \frac{1}{\sin\theta_e} \right) \left[\frac{n_i^{Pb} + n_{i+1}^{Pb}}{2} \varepsilon^{Pb} + n_i^{Te} \varepsilon^{Te} \right], \tag{3.2}$$

where $n_i^{Pb(Te)}$ is the atomic density of the ith Pb (Te) layer and ε^{Pb} and ε^{Te} are the stopping cross sections of Pb and Te atoms. Using the observed density of the first Pb layer (30% of the bulk density), $\Delta E^{Pb}_{1,2}$ is calculated to be about 80% of $\Delta E^{Pb}_{2,3}$. This calculated reduction of the peak spacing agrees with the experimental result 1.9 keV/2.6 keV = 0.73 observed at θ_e = 3.0°. The (111) surface of PbTe shows two-fold reconstruction pattern in the <110> direction by RHEED. The reconstruction pattern is clear at room temperature, but appears much dimmer when the crystal is heated to 520 K. Although the reconstruction pattern in the <112> direction is not clear, a detailed observation ensures the existence of a two-fold reconstruction pattern in this direction. These patterns indicate that the (111) surface has a 2×2 superlattice structure at room temperature. A surface structure that has one Pb atom in every unit cell of 2×2 superlattice is likely because the observed atomic density of the surface Pb layer (30%) agrees roughly with the expected atomic density from the structure (25%).

3.4 Conclusion

The surfaces of PbTe(001) and PbTe(111) have been observed by high-resolution RBS and RHEED. While the (001) surface shows no surface reconstruction except for the possibility of a small rumpling reconstruction, the (111) surface shows a reconstruction. The (111) surface is terminated by Pb atoms and the atomic density of the surface Pb layer is about 30% of the bulk value.

References

[1] D.P. Woodruff, T.A. Delchar, Modern Techniques of Surface Science, Cambridge University Press, Cambridge, 1986.

[2] K. Kimura, K. Ohshima, M. Mannami, Appl. Phys. Lett. 64 (1994) 2232.

[3] J. Fuchs, Z. Feit, H. Preier, Appl. Phys. Lett. 53 (1988) 894.

[4] R.F. Brebrick, A.J. Strauss, J. Chem. Phys. 40 (1964) 3230.

[5] H.H. Andersen, J.F. Ziegler, The Stopping and Ranges of Ions in Matter, Pergamon Press, New York, 1977.

Chapter 4

Charge-state distribution of 400 keV He ions scattered from solid surfaces

Charge-state distribution of backscattered He ions was investigated when 400 keV He^+ ions were incident on three different surfaces; clean Si(001)(2×1), SiO_2(2.5 nm)/Si(001) and Ag(0.31 ML)/Si(001). The dependence of the charge state on the exit angle of the scattered ions was obtained by measuring the energy spectra of both the scattered He^+ and He^{2+} ions at various exit angles for each surface. For the Si(001)(2×1) surface, the charge state of the scattered ions shows a considerable dependence on the exit angle, while no dependence is observed for the SiO_2/Si(001) surface. For the Ag/Si(001) surface, the He^+ fractions in the ions scattered from the surface Si and Ag atoms are significantly different from each other at large exit angle from the surface. These dependences are explained by a model including the nonequilibrium charge-exchange process of the exiting ions with the valence electrons at the surface.

4.1 Introduction

High-resolution Rutherford backscattering spectroscopy (HRBS) is used widely for depth profiling of solid materials, since it provides quantitative elemental analysis with high depth resolution (0.1–0.2 nm) in the surface region using a magnetic spectrometer for energy-analyzing scattered ions [1-7]. In HRBS measurement, only ions in a particular charge state (mainly single-charged ions) are detected, which could lead to errors in the analysis if the fraction of the detected charge state is not constant [8,9]. About 300–500 keV He^+ ions are usually employed for primary ions in HRBS because the fraction of He^+ ions in solid is reasonably high and almost constant over the energy region [10], which guarantees quantitative analysis of HRBS. However, dependence of the charge fraction on scattering geometry, surface conditions or atomic species from which ions are scattered could also lead errors to the analysis, and it remains incompletely understood.

In this chapter, charge-state distribution of backscattered He ions is investigated when 400 keV He^+ ions are incident on three different surfaces; clean Si(001)(2×1), SiO_2(2.5 nm)/Si(001) and Ag(0.31 ML)/Si(001). Dependence of the charge state on the exit angle of the scattered ions and on the atomic species from which ions are scattered is discussed in terms of nonequilibrium charge exchange in interaction of the exiting ions with valence electrons at the surface.

4.2 Experimental

A UHV scattering chamber (base pressure 8×10^{-11} Torr) was connected to a 400 kV Cockcroft-Walton accelerator via a differential pumping system. A beam of 400 keV He^+ ions was collimated with a series of slit systems to the size of 2×2 mm^2 and to the divergence angle of less than 3 mrad. The ions scattered at 50° from a specimen in the UHV chamber were energy analyzed with a 90° sector magnetic spectrometer and detected with a one-dimensional position sensitive detector (PSD) consisting of micro-channel plates (energy window 25%). The acceptance angle of the spectrometer was about 0.3 msr. For detection of scattered He^{2+} ions without a background consisting of He^+ ions, an electrostatic deflector installed between the spectrometer and the PSD was applied to resolve He^{2+} and low-energy He^+ ions passing through the magnetic spectrometer, and then only He^{2+} ions were accepted with the PSD, which is movable vertically.

Three surfaces; clean Si(001)(2×1), SiO_2(2.5 nm)/Si(001) and Ag(0.31 ML)/Si(001) were prepared as below. A specimen from Si(001) wafer with 2.5 nm silicon oxide was mounted on a 5-axes precision goniometer in the UHV scattering chamber. The specimen was direct-current heated and degassed at 660°C in UHV condition for three days [SiO_2(2.5 nm)/Si(001)]. Then, the specimen was heated up to ~1200°C for several seconds (flashing) and the oxide layer was removed [Si(001)(2×1)]. The surface showed 2×1 diffraction pattern by reflection

high-energy electron diffraction (RHEED). Finally Ag of 0.31 ML was evaporated on the Si(001)(2×1) at 500°C [Ag(0.31 ML)/Si(001)], where 1 monolayer (ML) equals to the atomic density of a Si(001) plane (= 6.78×10^{14} cm^{-2}).

Energy spectra of both the scattered He^{+} and He^{2+} ions at various exit angles ranging from 3° to 30° were measured at room temperature for SiO_2(2.5 nm)/Si(001) and Ag(0.31 ML)/Si(001) surfaces and at 650°C for clean Si(001)(2×1).

4.3 Results and discussion

Figure 4.1(a) shows HRBS spectra for He^{+} and He^{2+} ions scattered from SiO_2(2.5 nm)/Si(001) at the exit angle of 7°, and Fig. 4.1(b) shows the derived fraction of He^{q+} (q = 1, 2) as a function of the energy of the scattered ions, where neutral He atoms is not took into consideration since

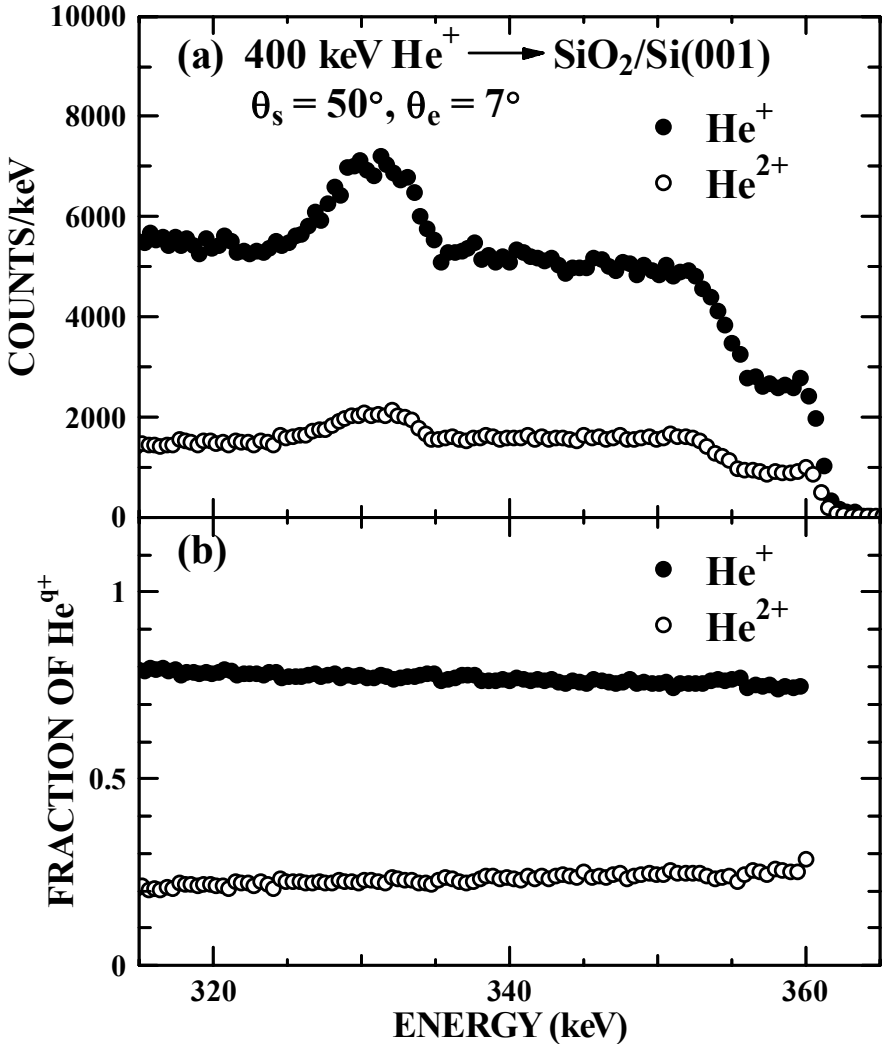

Fig. 4.1 (a) HRBS spectra for He^{+} and He^{2+} ions scattered from SiO_2 (2.5 nm)/Si(001) at the exit angle of 7°. (b) Derived fraction of He^{q+} (q = 1, 2) as a function of the energy of the scattered ions, where the existence of neutral He atoms is not took into consideration.

the fraction is expected to be much smaller than that of ions in this energy range [10]. The fraction of He^+ ions decreases slightly with the ion energy. This energy dependence was commonly observed independently of the exit angle and the kind of surface. It must be noted that the energy dependence of the He^+ ions is mostly artificial due to neglecting the fraction of neutral He atoms.

Figure 4.2 shows the observed fractions of He^+ ions scattered from Si atoms in the surface region of SiO_2(2.5 nm)/Si(001) and Si(001)(2×1) as a function of $1/\sin\theta_e$, which corresponds to pass length of exiting ions moving unit distance away from the surface, where θ_e is exit angle of the ions with respect to the surface. Whereas the fraction of He^+ ions scattered from SiO_2(2.5 nm)/Si(001) is almost constant at 0.74 over the investigated range of the exit angles, the fraction of He^+ ions scattered from Si(001)(2×1) exhibits a considerable dependence on $1/\sin\theta_e$. This dependence is explained as below by charge-exchange process of the exiting ions with valence electrons in the tail of electron distribution at the surface. Ions scattered beneath the atomic surface should achieve an equilibrium charge-state distribution during traveling to the atomic surface. Then the ions undergo interaction with valence electrons in the tail of electron distribution on the way of leaving the surface. Since the velocity of the valence electrons is lower than that of electrons beneath the atomic surface, the charge-state distribution of the ions shifts to higher charge state as they travel longer in the tail of the electron distribution.

Neglecting neutral He atoms, the fraction $F_1(\lambda)$ of He^+ ions on the

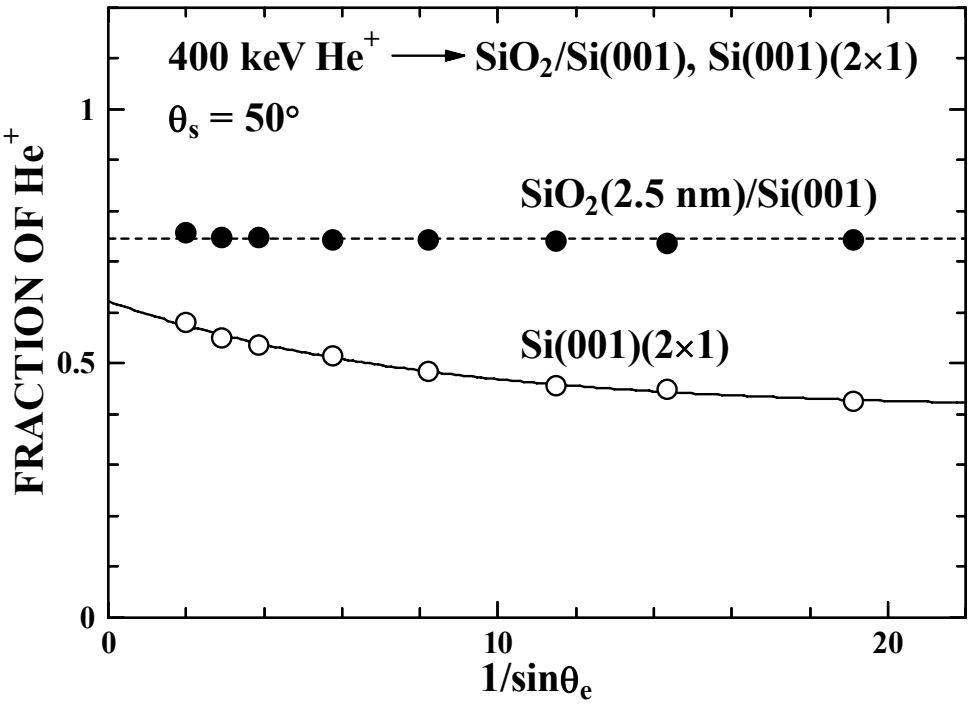

Fig. 4.2 Fractions of He^+ ions scattered from Si atoms in the surface region of SiO_2(2.5 nm)/Si(001) and Si(001)(2×1) as a function of $1/\sin\theta_e$, where θ_e is exit angle of the ions with respect to the surface. Solid line is given Eq. (4.2) fitted to the observed result for Si(001)(2×1).

exiting way from the surface of Si(001)(2×1) is described based on the above interpretation as

$$\frac{dF_1(\lambda)}{d\lambda} = (1 - F_1(\lambda))\sigma_c N(x) - F_1(\lambda)\sigma_l N(x), \tag{4.1}$$

where λ is the distance from the atomic surface along the exiting path of ions, $N(x)$ is the density of valence electrons at the distance of x from the atomic surface, and σ_c, σ_l are average electron capture cross section for He^{2+} ions and electron loss cross section for He^+ ions in the valence electrons outside the atomic surface, respectively. The observed fraction F_1^{obs} of He^+ ions after leaving the surface is given from Eq. (4.1) as

$$F_1^{obs} = \left(F_1^{bulk} - F_1^{surf}\right)\exp\left[-\frac{\sigma_c + \sigma_l}{\sin\theta_e}\int_0^\infty N(x)dx\right] + F_1^{surf}, \qquad (4.2)$$

where F_1^{bulc}, $F_1^{surf} = \sigma_c/(\sigma_c + \sigma_l)$ are the equilibrium charge fraction of He^+ ions beneath the atomic surface and in the valence electrons outside the atomic surface, respectively. The solid curve in Fig. 4.2 is given by Eq. (4.2) with $F_1^{bulc} = 0.622$, $F_1^{surf} = 0.410$ and $(\sigma_c + \sigma_l)\int_0^\infty N(x)dx = 0.128$, showing reasonably good agreement with the observed result for Si(001)(2×1). Considering that valence electrons of Si 3s and 3p are regarded to contribute to the charge exchange outside the atomic surface, the value of $\int_0^\infty N(x)dx$ can be estimated to be 1.36×10^{15} cm^{-2}. Therefore the average electron capture cross section σ_c for He^{2+} ions and electron loss cross section σ_l for He^+ ions in the valence electrons outside the atomic surface of Si(001)(2×1) are estimated to be 3.9×10^{-17} cm^2 and 5.6×10^{-17} cm^2, respectively.

On the other hand, the fraction of He^+ ions scattered from SiO_2(2.5 nm)/Si(001) surface is high and almost constant with $1/\sin\theta_e$. The large fraction of He^+ ions would come from the large electron capture cross section for He^{2+} ions due to the existence of oxygen atoms. Considering that oxygen supplies O 2s electrons with velocity close to the velocity of the scattered He ions, velocity matching proposed by Bohr, which predicts electrons with the velocity close to the velocity of ions are likely to be captured, can explain the large fraction of He^+ ions. The large capture cross section for He^{2+} ions from O 2s electrons can also contributes to the

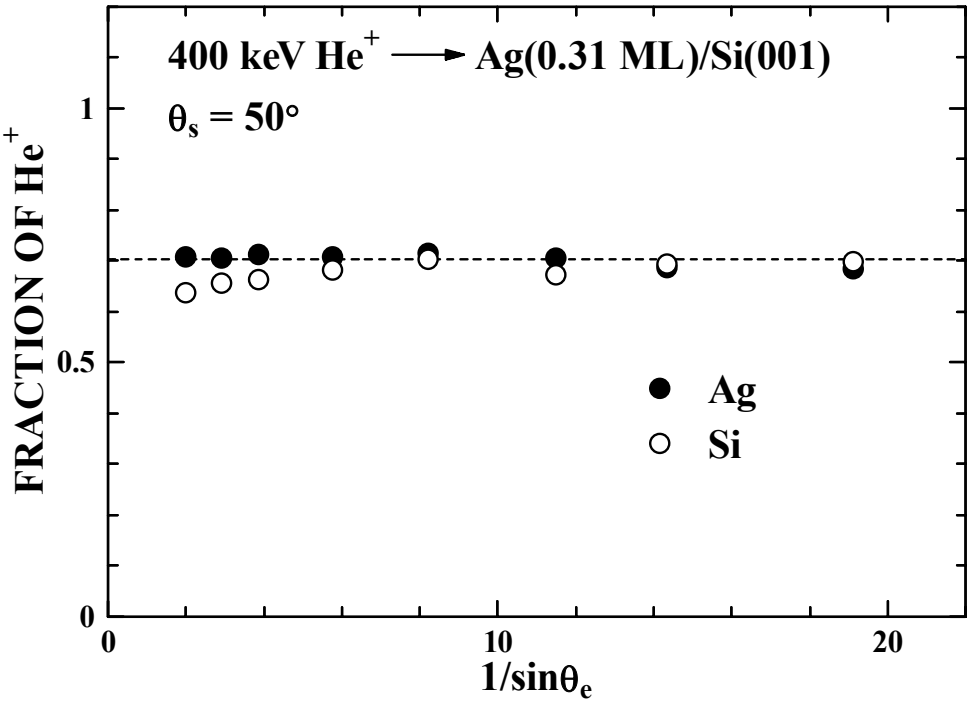

Fig. 4.3 Fractions of He^+ ions scattered from Si and Ag atoms in the surface region of Ag(0.31 ML)/Si(001) as a function of $1/\sin\theta_e$, respectively, where θ_e is exit angle of the ions with respect to the surface.

constant fraction of He^+ ions, since it may compensate electron loss due to Si valence electrons in the tail of electron distribution at the surface.

Figure 4.3 shows the observed charge fractions of He^+ ions scattered from Si and Ag atoms in the surface region of Ag(0.31 ML)/Si(001) as a function of $1/\sin\theta_e$. It is noted that the fraction depends significantly on whether ions are scattered from Si atoms or Ag atoms, beyond the margin of estimated errors in the fractions (< 1%; not shown in Fig. 4.2 and Fig. 4.3 as the error bars are smaller than the size of symbols). Whereas the fraction of He^+ ions scattered from Ag atoms is almost constant at 0.70, the fraction of He^+ ions scattered from Si atoms is smaller and increases as $1/\sin\theta_e$ increases. This can be explained again in terms of

velocity matching. Since Ag 4p electrons has velocity close to that of the scattered ions, the ions scattered from Ag atoms is likely to be in low charge state (large fraction of He^+ ions) and the charge state of ions from Si atoms also shifts lower as the exiting path near the surface Ag atoms is longer. Consequently, the difference in charge-state distribution corresponding to Si and Ag atoms is negligible at large $1/\sin\theta_e$, which means charge equilibrium is achieved. Conversely, analysis by measurement with small $1/\sin\theta_e$ or at large exiting angle θ_e, where charge equilibrium is not yet achieved, could be misleading in determination of surface composition, for example, amount of sub ML adsorbate. This case provides a good example suggesting that a scattering geometry with small exit angle is effective to avoid errors produced by assuming same charge-state distributions for ions scattered from different species.

4.4 Conclusion

Charge-state distribution of backscattered He ions has been investigated when 400 keV He^+ ions were incident on three different surfaces; clean Si(001)(2×1), SiO_2(2.5 nm)/Si(001) and Ag(0.31 ML)/Si(001). For Si(001)(2×1) surface, the charge state of the scattered ions shows a considerable dependence on the exit angle, while no dependence is observed for SiO_2/Si(001) surface. From the dependence of the charge state on the exit angle, the average electron capture cross section for He^{2+} ions and electron loss cross section for He^+ ions in valence electrons outside the atomic surface of Si(001)(2×1) are estimated to be 3.9×10^{-17} cm^2 and 5.6×10^{-17} cm^2, respectively. For Ag/Si(001) surface, the fraction of He^+ ions scattered from the surface Si and Ag atoms differs significantly from each other at large exit angle from the surface, which could be misleading in determination of surface composition using a same charge fraction for ions scattered from different species. Adopting a scattering geometry with small exit angle is effective to avoid errors produced by such a dependence of charge-state distribution.

References

[1] T. Enders, R. Rilli, H.D. Carstanjen, Nucl. Instr. and Meth. B 64 (1992) 817.

[2] G. Dollinger, T. Faestermann, P. Maier-Komor, Nucl. Instr. and Meth. B 64 (1992) 422.

[3] K. Kimura, K. Ohshima, M. Mannami, Appl. Phys. Lett. 64 (1994) 2232.

[4] K. Kimura, M. Mannami, Nucl. Instr. and Meth. B 113 (1996) 270.

[5] W.M. Arnoldbik, W. Wolfswinkel, D.K. Inia, V.C.G. Verleun, S. Lobner, J.A. Reinders, F. Labohm, D.O. Boerma, Nucl. Instr. and Meth. B 118 (1996) 567.

[6] W.A. Lanford, B. Anderberg, H. Enge, B. Hjorvarsson, Nucl. Instr. and Meth. B 136-138 (1998) 1177.

[7] K. Kimura, K. Nakajima, M. Mannami, Nucl. Instr. and Meth. B 136-138 (1998) 1196.

[8] T. Nishimura, Y. Hoshino, Y. Kido, Surf. Sci. 452 (2000) 139.

[9] C. Klein, R. Grötzschel, M. Mäder, W. Möller, Nucl. Instr. and Meth. B 190 (2002) 122.

[10] J.C. Armstrong, J.V. Mullendore, W.R. Harris, J. B. Marion, Proc. Phys. Soc. 86 (1965) 1283.

Chapter 5

Direct observation of intermixing at Ge/Si(001) interfaces by high-resolution Rutherford backscattering spectroscopy

The initial stage of epitaxial growth of Ge on Si(001) is studied with high-resolution Rutherford backscattering spectroscopy. In contrast to the generally accepted picture, intermixing of Ge and Si starts before the deposition of first atomic layer at 500°C. Even when sub-monolayer Ge is deposited at room temperature, intermixing takes place during annealing at 300–800°C. These observations are in reasonable agreement with a recent theoretical study based on generalized gradient approximation density functional calculations [Y. Yoshimoto and M. Tsukada, Surf. Sci. **423**, 32 (1999)].

5.1 Introduction

The growth of Ge on Si(001) is a typical model system for investigation of heteroepitaxy. It has been extensively studied from the viewpoint of fundamental physics and because of its technological importance. The growth mode is known to be the Stranski-Krastanov mode with a critical thickness of three monolayers (ML; 6.78×10^{14} cm^{-2} in the present case) [1]. In the sub-ML coverage region, investigations with low-energy electron microscopy [2] and surface stress-induced optical deflection [3] provide a picture of dispersive adsorption, with Ge displacing Si from terraces. This is followed by full Ge termination at 1 ML, because the Ge dangling-bond energy is lower than the Si dangling-bond energy [4]. Above 1 ML coverage, an intermixing phase has been observed. The first evidence of the intermixing layer was reported by Copel *et al.* with medium energy ion scattering (MEIS) [5]. They found intermixing at the coverage larger than 2 ML at a growth temperature of 500°C, while no intermixing was detected at 1 ML. Similar results were also reported at 400°C using extended x-ray absorption fine structure: substantial intermixing was observed at 2 ML, while no intermixing was detected at 1 ML [6].

In a recent study, however, significant intermixing at 1 ML was reported by Sasaki *et al.* using the Auger electron diffraction (AED) technique [7]. They found that more than half of the deposited Ge atoms are distributed in the subsurface region even at 1 ML, when the Ge/Si(001) is annealed at 350–600°C after room-temperature (RT) deposition. The best

fit between the observed and simulated AED patterns was obtained with a Ge distribution over the first to the fifth layers with a concentration ratio of 4:1:1:1:1 [7]. The same result was obtained by the deposition of 1 ML Ge at 400–600°C and the formation of a stable phase was concluded [8]. More recently, Ikeda *et al.* studied the intermixing at the Ge/Si(001) interfaces prepared by the deposition of 0.15 and 1 ML Ge at 400°C by means of surface energy loss spectroscopy of MEIS (SELS-MEIS) [9]. They reported that the observed mean energy loss of the scattered ions from the surface Ge atoms can be explained by a Ge distribution with a concentration ratio of 4:3:1 or 4:2:2 for the first to the third layers both at 0.15 and 1 ML. Although neither AED nor SELS-MEIS provides an accurate Ge distribution, these results disagree qualitatively with the generally accepted picture of the full Ge termination at 1 ML.

It is important in the semiconductor industry to solve the above controversy, because the intermixing may affect considerably the Si/Ge heterostructure properties (optical, electronic, and so on). More accurate measurement of the Ge profile is required to capture the true picture of intermixing of Ge and Si in the sub-ML region. Recently, we have demonstrated that monolayer resolution can be achieved in Rutherford backscattering spectroscopy (RBS) using a high-resolution spectrometer and a grazing-angle technique [10]. This new technique, called high-resolution RBS (HRBS), is a powerful tool in surface studies [11]. Here we report on the direct measurement of the Ge distribution in the initial stage of the Ge/Si(001) epitaxial growth with HRBS. Existence of an

intermixing layer at sub-ML coverage is confirmed by the direct measurement of the Ge profile.

5.2 Experimental

The preparation of the samples was performed in a UHV scattering chamber (base pressure 9×10^{-11} Torr), which was connected to a 300 kV tandem-type accelerator (Shimazu, MIG-300) via a differential pumping system. A clean Si(001) surface was prepared *in situ* by dc-resistive heating of a Si(001) wafer with a native oxide at ~1200°C. A Si buffer layer with thickness about 50 nm was deposited at 650°C with an electron beam evaporator to prepare a flat and clean (2×1) surface. Deposition of Ge was done with a tungsten-wire basket at a rate of ~0.5 ML/min at RT or 500°C. The layer deposited at RT was annealed successively in vacuum at 300, 400, 500, 600, 700, and 800°C for 3 min at each temperature. The temperature of the Si wafer was measured with an infrared radiation thermometer.

The details of the HRBS measurements are described in Chapter 2, thus only the brief overview is given here. A beam of 400 keV He^+ ions collimated to 3×3 mm^2 by a series of apertures was incident on the samples of Ge/Si(001). A typical beam current was about 10 nA. The ions scattered at 30° from the Ge/Si(001) were energy analyzed by a 90° sector magnetic spectrometer. The exit angle θ_e was 2° with respect to the surface plane. The energy resolution of the system was about 0.9 keV, which was mainly determined by the energy spread of the incident beam. A typical dose for one HRBS measurement was about 20 μC.

5.3 Results and discussion

5.3.1 Anneal after deposition at RT

Figure 5.1(a) displays an example of the observed HRBS spectrum for the Ge/Si(001) prepared by the deposition of 0.4 ML Ge at RT together with the HRBS spectrum for the virgin Si(001). There is a sharp peak at ~393.5 keV, which corresponds to the Ge atoms in the topmost atomic layer. To derive the depth profile of Ge atoms from the observed HRBS spectrum, we have developed a simulation code to calculate the HRBS spectrum from the elemental compositions in the individual atomic layers. The simulation includes the energy loss straggling and the reduction of the scattering cross section from the Rutherford formula due to screening effects. The solid and dotted curves in Fig. 5.1(a) show the best-fit result of the simulation and the Ge contribution in each atomic layer, respectively. The concentrations C_i of Ge are found to be 32.5%, 3.5%, 0.5%, and 1% ± 0.5% for the first, second, third, and fourth atomic layers, respectively. These concentrations are close to those (33%, 6%, 1%, and 0.1%) expected for the simultaneous multilayer growth mode [12], which suggests that surface diffusion is almost perfectly inhibited at RT.

Upon annealing at 300°C for 3 min, a notable change can be seen in the HRBS spectrum as shown in Fig. 5.1(b). The height of the Ge peak decreases, while the total amount of Ge does not change. This change indicates that a part of the Ge atoms move into the subsurface layers as the

result of the intermixing of Ge and Si during the annealing. It must be noted that a formation of Ge islands by annealing can explain the observed change, but the observed reflection high energy electron diffraction (RHEED) pattern showed no bulk spots that indicate the island formation. This RHEED observation is consistent with scanning tunneling microscopy

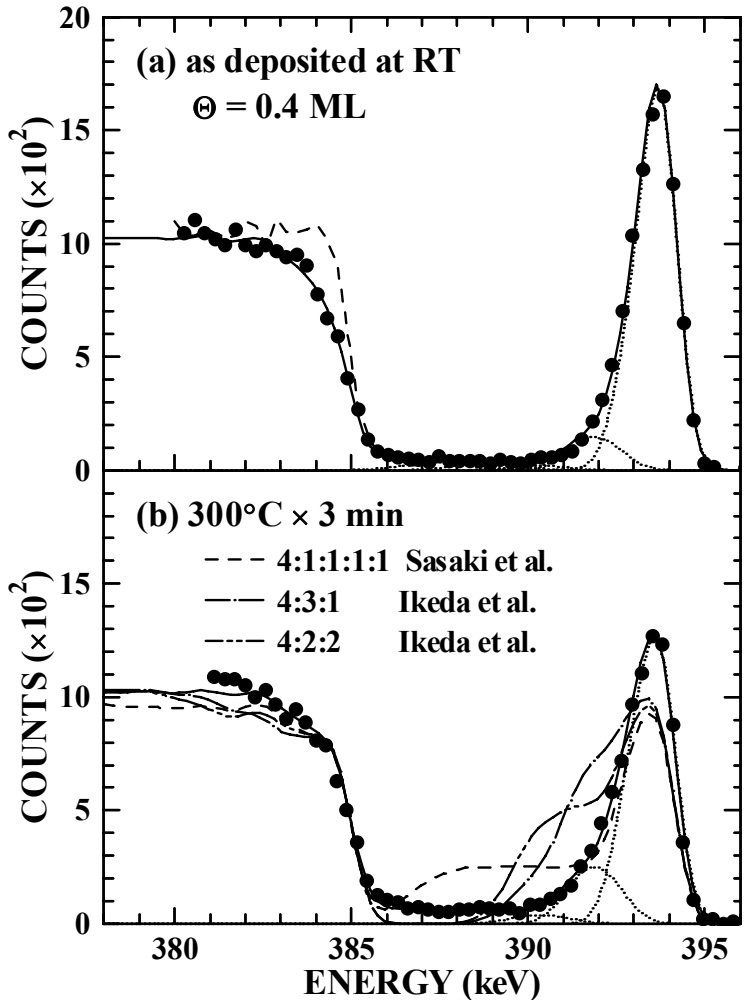

Fig. 5.1 (a) HRBS spectrum of Ge/Si(001) prepared by deposition of 0.4 ML Ge onto Si(001) at RT. The dashed curve shows the spectrum of the virgin Si(001). The bestfit simulation result is shown by the solid curve. The dotted curves show the contribution of Ge for individual atomic layers. (b) Postannealed (300°C × 3 min) result. The calculated spectra with Ge distributions proposed by Sasaki *et al.* [7] and Ikeda *et al.* [9] are also shown for comparison.

(STM) observations, which showed no Ge island higher than one atomic height [8]. Thus the observed change is ascribed to the intermixing of Ge and Si. The best-fit result of the spectral simulation is shown by the solid and dotted curves. The obtained Ge concentrations of the top four atomic layers are 26%, 6%, 1%, and 1.5% ± 0.5%, respectively. The HRBS spectra calculated with the concentration ratios reported by Sasaki *et al.* and Ikeda *et al.* are also shown for comparison [Fig. 5.1(b)]. These curves do not agree with the present results.

A series of anneals at 400, 500, 600, 700, and 800°C for 3 min each was applied to the Ge/Si(001) sample after the 300°C anneal mentioned above. The change in the Ge concentration is shown in Fig. 5.2(a). The concentration C_i of each layer normalized to that of the first layer (C_1) is also shown in Fig. 5.2(b) to see clearly the small change. After the decrease at 300°C, C_1 is almost constant up to 600°C and then decreases rapidly at 800°C. The behavior of C_2 is characteristic: C_2 shows a maximum at 400°C, while the concentrations of deeper layers show monotonic increases. The bulk diffusion coefficients estimated from the high temperature data (a pre-exponential factor 0.35 cm^2/s and an activation energy 3.93 eV [13]) are 9.5×10^{-36}, 1.3×10^{-30}, 7.2×10^{-24}, and 1.2×10^{-19} cm^2/s at 300, 400, 600, and 800°C, respectively. These values are too small to explain the observed intermixing, except at 800°C.

The present results can be qualitatively understood by the following scenario. The migration energy in the surface region is usually smaller than the bulk value. The observed intermixing at 300°C indicates that the height

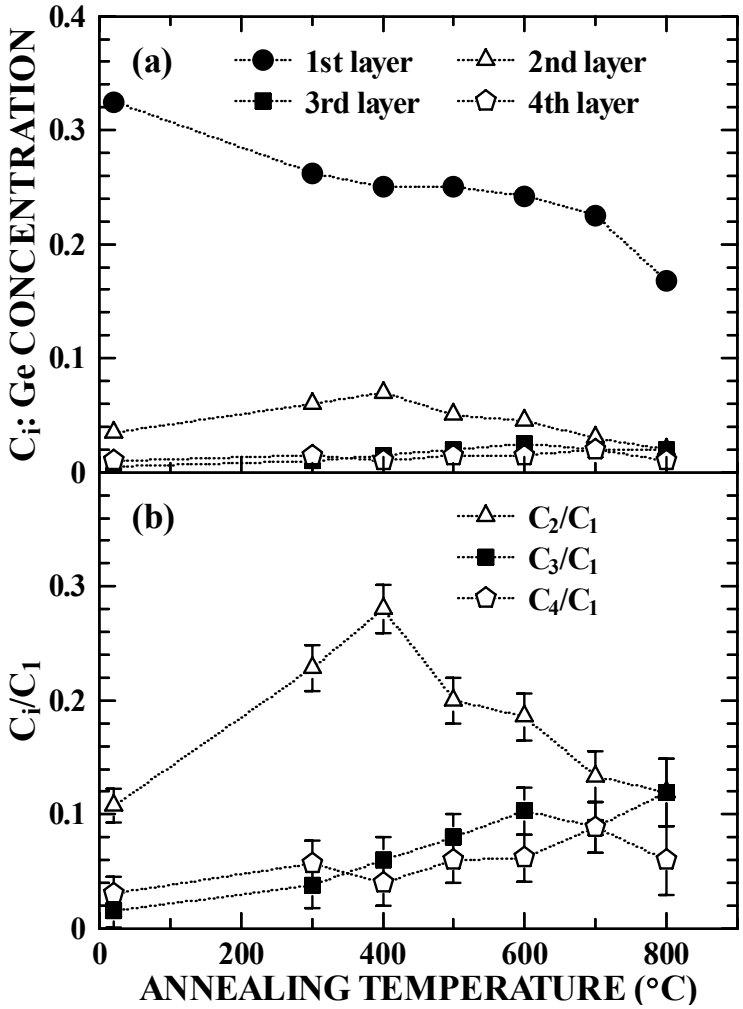

Fig. 5.2 (a) Change of the measured Ge concentrations in the first four atomic layers as a function of temperature for the last annealing step. (b) Concentrations relative to the first layer.

of the energy barrier E_{12} for Ge migration from the first layer to the second layer is much smaller than the bulk migration energy. At 500°C, C_2 starts to decrease, indicating that Ge atoms migrate into the third layer. This means that the energy barrier E_{23} for Ge migration from the second layer to the third layer is larger than E_{12}, but still smaller than the bulk value.

The mechanism of the intermixing of Ge and Si is often discussed in terms of the stress induced by surface dimers [8,14-16]. There are atomic

sites under tensile stress in the third and fourth layers between the surface dimers. These sites favor Ge occupation, because Ge atoms reduce the tensile stress with their larger atomic size. Nevertheless, our results show no accumulation of Ge in the third and fourth layers. This is consistent with a recent theoretical study based on a generalized gradient approximation density functional calculation, which predicted no anomaly in the Ge concentration in the third or fourth layers [17]. The slightly larger occupation probability at the between-dimer-row sites is canceled out by the lower occupation probability at the under-dimer-row site, which is compressed by the dimer row. The calculated ratios for 0.4 ML under thermodynamical equilibrium at 600°C are C_2/C_1 = 0.067, C_3/C_1 = 0.06, and C_4/C_1 = 0.05. These are of the same order as our results, although the observed Ge concentration decreases somewhat more rapidly with depth than the calculated results. This suggests that full thermodynamical equilibrium is not reached at 600°C in our experiments.

5.3.2 Deposition at 500°C

Figure 5.3 shows the HRBS spectra observed during the initial stage of the Ge growth at 500°C. The amount of the deposited Ge was 0.5 ML for Fig. 5.3(a) and 1.5 ML for Fig. 5.3(b). The obtained Ge concentrations in the first four layers are 34%, 8.5%, 2%, and 1% ± 0.5% at 0.5 ML, and 64.5%, 38%, 22.5%, and 11% ± 1% at 1.5 ML. Based on simple surface energy considerations, after the complete occupation of 1 ML Ge in the first layer, the Ge atoms start to occupy up to 0.5 ML at the fourth-layer

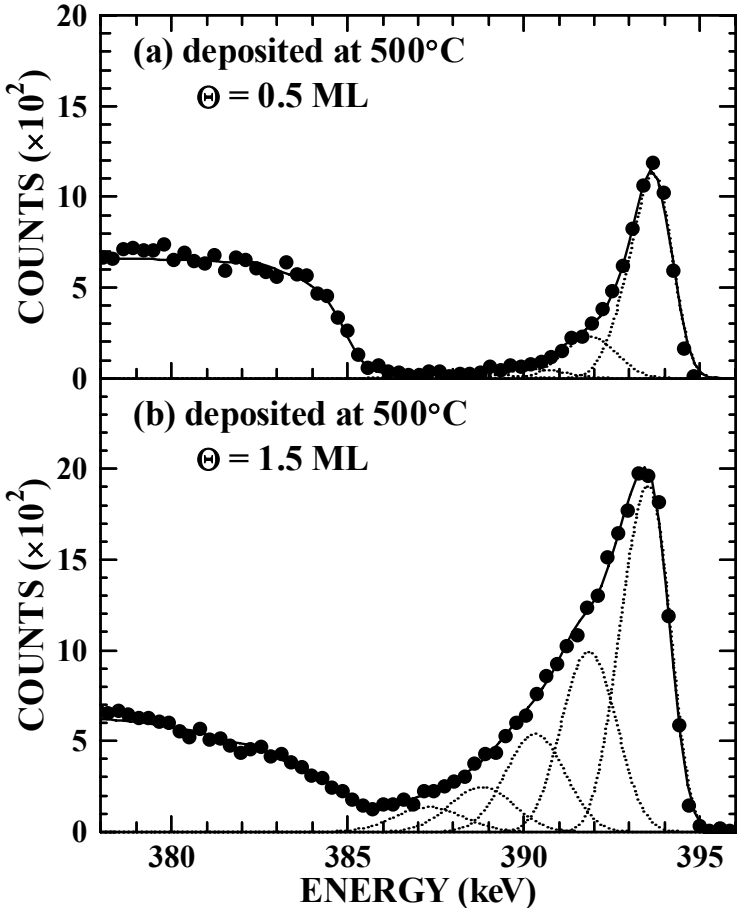

Fig. 5.3 HRBS spectra of Ge/Si(001) prepared by deposition at 500°C. Best-fit simulation results are shown by curves. Significant intermixing can be seen at 1.5 ML.

tensile sites [16]. The present result, however, does not show any anomaly in the Ge concentration in the fourth layer, and the concentration in the first layer is not 100% but about 65% at 1.5 ML. This clearly indicates that simple surface energy considerations are not sufficient.

5.3.3 Miscellaneous issues in analysis

In this section miscellaneous issues in quantitative analysis of the Ge/Si(001) with HRBS are discussed. The first one is relating to the surface

steps (roughness). In the determination of the composition from an observed spectrum analysis with the simulation code, the surface was assumed to be atomically flat. If the surface step density is comparable or larger than $\sin\theta_e/d$ (d is the surface step height), however, the surface steps would affect the HRBS spectrum and then lead to a significant error in the obtained composition. To see the effect of the surface steps on the determination of the composition in the present case, HRBS measurements at various θ_e (= 2°, 3°, 4°, 6°) were performed for the identical sample of Ge/Si(001). The obtained Ge concentrations hardly depend on θ_e, indicating that the surface step density is low enough not to undermine the assumption that the surface is atomically flat. This is also supported by the STM observation of the Si(001) prepared with the same wafer and procedures as the present case. The observed step density was about 0.05 nm^{-1}.

The second one is concerning the charge-state distribution of the scattered ions (particles). In the present study, the energy spectrum of the backscattered He^+ ions was measured as usual because the fraction of He^+ is highest among the possible charge state and almost independent of the energy in the energy region of 200–400 keV. If the charge-state distribution depends on the atomic species and/or depth from which the ion scattered, however, the Ge distribution deduced only from the He^+ spectrum does not represent the true distribution. Figure 5.4 shows examples of He^+ and He^{2+} spectra for Ge/Si(001) prepared by the deposition of 0.5 ML Ge at 500°C, together with the ratio of the He^+ yield to the He^{2+} yield (filled circles). The

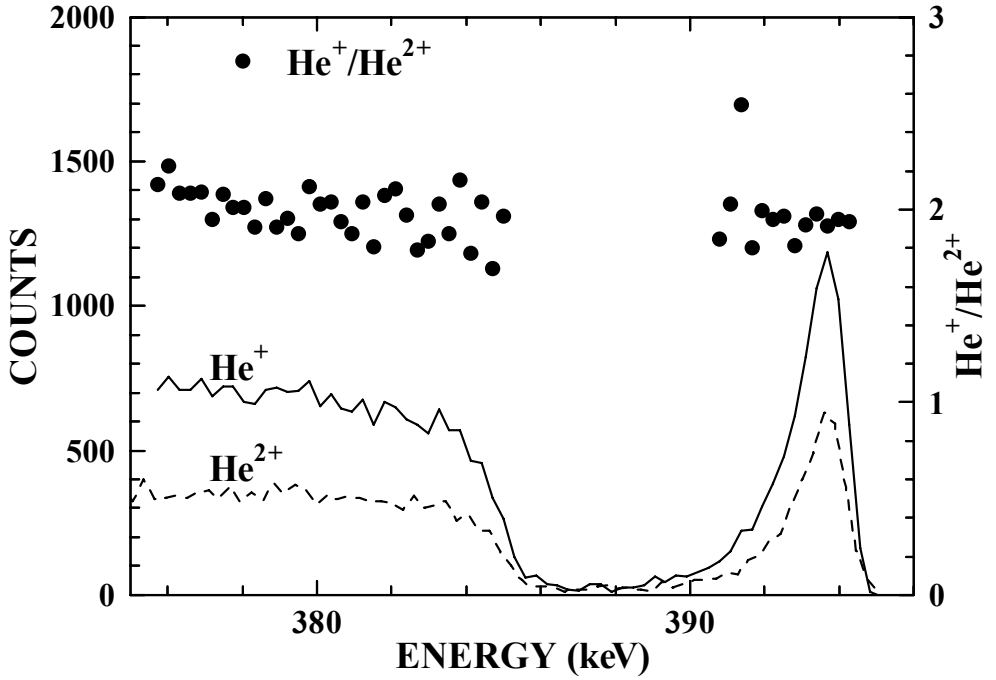

Fig. 5.4 HRBS spectra of the scattered He^+ and He^{2+} ions for Ge/Si(001) prepared by deposition of 0.5 ML Ge onto Si(001) at 500°C. The ratio of the He^+ yield to the He^{2+} yield is also shown by filled circles. The charge state distribution does not depend on the atomic species or depth.

He^+/He^{2+} ratio is almost constant, indicating that charge state distribution does not depend on the atomic species or depth [18]. This allows quantitative analysis in HRBS without measuring all charge states.

The last one is concerning the irradiation damage. During the HRBS measurements, radiation damage may cause so-called ion-beam mixing. The defect distribution in Si(001) generated by the irradiation of 400 keV He ions was estimated using the TRIM95 code. The calculated concentration of vacancies produced by one HRBS measurement (irradiation of 6.5×10^{14} ions/cm^2) is about 0.7% in the surface region. This concentration is low enough to neglect the effects of the irradiation damage.

In order to confirm this, the same HRBS measurements were repeated after the irradiation of 3×10^{15} ions/cm^2, which corresponds to the fluence of five HRBS measurements. There was no detectable change in the HRBS spectrum as shown in Fig. 5.5, indicating that the effect of the radiation damage induced by the HRBS measurements is negligibly small.

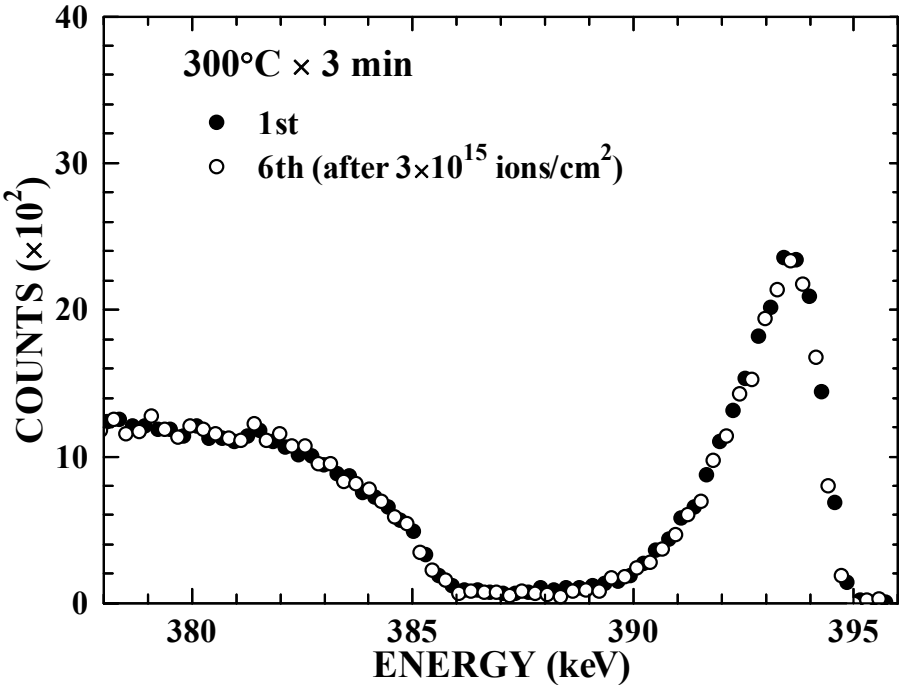

Fig. 5.5 HRBS spectra for Ge/Si(001) annealed at 300°C, which were obtained from the initial measurement (filled circles) and one after the irradiation of 3×10^{15} ions/cm^2 (open circles), respectively. There was no detectable change in the spectrum.

5.4 Conclusion

HRBS was successfully used to study the intermixing on the initial stage of Ge/Si(001) epitaxial growth. The distribution of Ge was directly determined with monolayer resolution using the simulation code calculating a HRBS spectrum from the elemental compositions in the individual atomic layers. The growth of 0.4 ML Ge on Si(001) at RT can be understood as the simultaneous multilayer growth without the intermixing. In contrast, substantial Ge concentration beyond that expected from the simultaneous multilayer growth was found in the subsurface atomic layers up to the fifth layer when the Ge/Si(001) was annealed at over 300°C after RT or Ge was deposited at 500°C. This indicates that the intermixing between Ge and Si takes place even in the stage of submonolayer deposition at elevated temperature. While a simple energetic consideration predicts preferential Ge occupation in the between-dimer-row sites in the third and fourth layers, the observed Ge concentration does not show any anomaly in the third or fourth layer. These results are in reasonable agreement with recent first principles calculations based on a generalized gradient approximation density functional method [17].

References

[1] H.-J. Gossmann, L.C. Feldman, W.M. Gibson, Surf. Sci. 155 (1985) 413.

[2] R.M. Tromp, M.C. Reuter, Phys. Rev. Lett. 68 (1992) 954.

[3] A.J. Schell-Sorokin, R.M. Tromp, Phys. Rev. Lett. 64 (1990) 1039.

[4] R. M. Tromp, Phys. Rev. B 47 (1993) 7125.

[5] M. Copel, M.C. Reuter, M. Horn von Hoegen, R.M. Tromp, Phys. Rev. B 42 (1990) 11682.

[6] H. Oyanagi, K. Sakamoto, R. Shioda, Y. Kuwahara, K. Haga, Phys. Rev. B 52 (1995) 5824.

[7] M. Sasaki, T. Abukawa, H.W. Yeom, M. Yamada, S. Suzuki, S. Sato, S. Kono, Appl. Surf. Sci. 82/83 (1994) 387.

[8] H.W. Yeom, M. Sasaki, S. Suzuki, S. Sato, S. Hosoi, M. Iwabuchi, K. Higashiyama, H. Fukutani, M. Nakamura, T. Abukawa, S. Kono, Surf. Sci. 381 (1997) L533.

[9] A. Ikeda, K. Sumitomo, T. Nishioka, T. Yasue, T. Koshikawa, Y. Kido, Surf. Sci. 385 (1997) 200.

[10] K. Kimura, K. Ohshima, and M. Mannami, Appl. Phys. Lett. 64 (1994) 2232.

[11] K. Kimura, M. Mannami, Nucl. Instr. and Meth. B 113 (1996) 270; K. Kimura, K. Nakajima, M. Mannami, Nucl. Instr. and Meth. B 136–138 (1996) 1196.

[12] C. Argile and G. E. Rhead, Surf. Sci. Rep. 10 (1989) 277.

[13] G. Hettich, H. Mehrer, K. Maier, in *Proceedings of the International Conference on Physics of Semiconductors* (Institute of Physics, London, 1979), p. 500.

[14] P. C. Kelires, J. Tersoff, Phys. Rev. Lett. 63 (1989) 1164.

[15] F. K. LeGoues *et al.,* Phys. Rev. Lett. 64 (1990) 2038.

[16] F. Liu, M.G. Lagally, Phys. Rev. Lett. 76 (1996) 3156.

[17] Y. Yoshimoto, M. Tsukada, Surf. Sci. 423 (1999) 32.

[18] K. Kimura, H. Ohtsuka, M. Mannami, Phys. Rev. Lett. 68 (1992) 3797.

Chapter 6

Initial oxidation process on Si(001) studied by high-resolution Rutherford backscattering spectroscopy

We have observed the initial oxidation process on Si(001) at 20–700°C in 10^{-7}–10^{-4} Torr O_2 pressure by high-resolution Rutherford backscattering spectroscopy. The oxygen coverage saturates at 1.45±0.2 ML (1 ML = 6.78×10^{14} cm^{-2}) and 2.3±0.3 ML at room temperature (RT) and 640°C, respectively. The oxidation of the second layer is found to start before the first layer oxidation is completed even at RT. Further oxidation proceeds basically in the layer-by-layer mode, although there is a compositional transition layer of sub-nm thickness in the interface.

6.1 Introduction

Reduction of the thickness of gate oxide films in ultralarge-scale-integrated circuits is a crucial issue in shrinking design rules. Metal-oxide-semiconductor field-effect transistor devices with oxide layers of 1.1 nm thickness have already been fabricated in laboratories [1]. For further reduction, the initial oxidation process on Si(001) surfaces should be clarified. A recent study with scanning reflection electron microscopy (SREM) revealed that the oxidation proceeds in the layer-by-layer mode [2]. A barrierless oxidation of the first layer was observed to occur at room temperature (RT), and the energy barrier of the second layer of oxidation was determined to be 0.3 eV. This suggests the possibility of formation of a SiO_2 layer as thin as one monolayer thickness (~0.3 nm). Previous studies, however, reported the existence of transition layers of 0.5–2.5 nm thickness at the SiO_2/Si(001) interface [3-7], suggesting that the composition and/or structure of such a ultrathin oxide layer of sub-nm thickness is different from thicker oxide layers.

From the theoretical viewpoint, the backbond (BB) site of the down dimmer atom is known to be the most preferable site for oxygen adsorption [8]. Based on first-principles calculations, oxidation of BB sites was shown to be via an apparently barrierless reaction in accordance with the SREM observation [9]. The scanning tunneling microscopy (STM) observations also suggested that oxygen atoms adsorb on the BB sites in the early stage of oxidation [10-12], although direct imaging of the adsorbed oxygen atom

by STM is rather difficult [13]. After one BB site is oxidized, the first-principles calculation showed that the second layer bonds are energetically preferred to the other Si-Si bonds of the first layer [14,15]. This results in vertical growth rather than layer-by-layer growth in contradiction to the SREM observation. Thus the initial oxidation process is still unclear. Especially, information about the composition and structure of the oxide layer in the initial oxidation stage is not sufficient for full understanding of the oxidation process.

In the chapter, the initial oxidation process on Si(001) is observed by high-resolution Rutherford backscattering spectroscopy (HRBS). HRBS allows us to measure oxygen depth profiles with depth resolution at an atomic level [16,17]. Sequential oxidation by oxygen isotopes was employed to see the dynamics of the initial oxidation process [6]. The results of the HRBS measurement indicate that second layer oxidation starts before the first layer oxidation is completed even at RT.

6.2 Experimental

An ultrahigh vacuum (UHV) scattering chamber (base pressure 8×10^{-11} Torr) was connected to a 4 MV Van de Graaff accelerator via a differential pumping system. A clean Si(001) (2×1) surface was prepared *in situ* by flashing a Si(001) wafer at ~1150°C. A Si buffer layer of ~100 nm thickness was deposited at 650°C with an electron beam evaporator to prepare a flat and clean surface. Oxidation of the Si(001) was carried out by introducing molecular oxygen into the scattering chamber. Both $^{16}O_2$ (99.995%) and $^{18}O_2$ (95%) gases were used for sequential isotopic exposures to see the dynamics of the oxidation [6].

A beam of 350 keV He^+ ions from the accelerator was collimated to 2×2 mm^2 and a divergence angle of less than 1 mrad by a series of apertures. The beam current, which was monitored by a vibrating beam chopper, was ~25 nA, and a typical fluence for one HRBS measurement was 15 μC (1.6×10^{15} ions cm^{-2}). The measurement was usually performed on a new area of the sample to avoid radiation damage, although there was no detectable change in the spectrum even if the measurement was repeated on the same position.

The ions scattered at 50° from the Si sample were energy analyzed by a 90° sector magnetic spectrometer. The acceptance angle of the spectrometer was 0.3 msr. The best energy resolution observed using the present HRBS system was 0.33 keV at 292 keV, including the energy spread of the incident beam. A quadrupole electrostatic lens was installed

just before the spectrometer to correct the so-called ‘‘kinematic broadening’’ [18]. The estimated kinematic broadening without the correction is about 2 keV for 350 keV He ions scattered from ^{16}O atoms under the present experimental conditions. Because the corresponding depth resolution is about 0.5 nm, the correction for the kinematic broadening is essential to achieve atomic level depth resolution.

6.3 Results and discussion

Figure 6.1 shows examples of the HRBS spectra observed under [011] channeling conditions. The spectra for the clean surface (closed circles), after 20 min oxidation at RT under $^{16}O_2$ gas pressure of 2×10^{-6} Torr (open circles), and after an additional 20 min oxidation at 640°C under $^{18}O_2$ gas pressure of 2×10^{-6} Torr (triangles) are shown. These oxidation conditions are the same as those in the previous SREM study [2], where the oxidation of the first (second) layer was observed at RT (640°C). In the HRBS spectra, separated peaks of ^{16}O and ^{18}O signals are clearly seen at

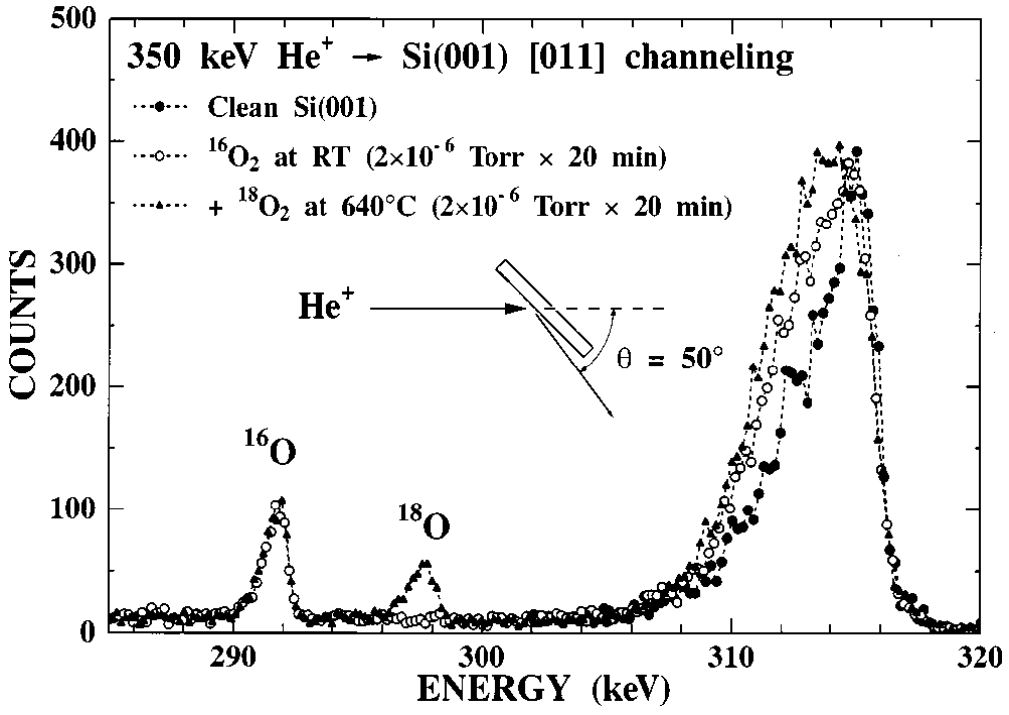

Fig. 6.1 Observed HRBS spectra for a clean Si(001) surface (closed circles), after 20 min oxidation under $^{16}O_2$ gas pressure of 2×10^{-6} Torr at room temperature (open circles), and after additional 20 min oxidation under $^{18}O_2$ gas pressure of 2×10^{-6} Torr at 640°C (triangles). The ^{16}O peak is not changed by the additional oxidation at 640°C.

around 292 and 298 keV, respectively.

The amounts of ^{16}O and ^{18}O atoms were derived from the observed HRBS spectra at various oxidation conditions. The oxygen coverage θ was found to be saturated at RT as well as at 640°C, while no clear saturation was observed at 700°C in agreement with the previous report [2]. The observed saturation coverage was 1.45±0.2 ML (1 ML = 6.78×10^{14} cm^{-2}) and 2.3±0.3 ML at RT and 640°C, respectively. These values indicate that the first (second) Si layer is not completely oxidized at RT (640°C). It should be noted that the ^{16}O yield was not changed by the additional $^{18}O_2$ oxidation at 640°C (see Fig. 6.1) showing no exchange of oxygen atoms during oxidation at 640°C. This is different from the MEIS observation for relatively thicker oxide layers (1.5–5 nm) at higher temperatures (1020–1170 K), where the exchange of oxygen atoms at the surface region during oxidation was reported [6].

From the observed HRBS spectrum, the oxygen depth profile was derived. Here, we employed a simple procedure, i.e., oxygen concentration was calculated from the yields of oxygen and silicon at the same depth taking account of the cross-section difference. The stopping power of a typical thermal oxide (ρ = 2.35 g/cm^3) was used in conversion from energy to depth. There might be an error of several percent in the depth scale because the stopping power of the pure Si is larger than that of the typical thermal oxide film by ~8% for ~300 keV He ions.

Figure 6.2 shows the obtained oxygen depth profiles at various oxidation conditions. After oxygen exposure of 2400 L (Langmuir: 1×10^{-6}

Torr s) at RT [profile (b)], the oxygen concentration reaches 50% at the surface region, showing formation of a SiO-like oxide layer. An almost stoichiometric SiO_2 layer is formed by oxidation at 640°C [profile (c)]. In further oxidation, the oxygen profile moves deeper without a significant change in shape, indicating that the oxidation process is basically layer-by-layer in harmony with the SREM observation [2].

The observed oxygen profile can be fitted reasonably well by an error function as shown by solid curves in Fig. 6.2. The standard deviation σ of the error function is 0.28 and 0.32 nm for the profiles (d) and (e), respectively, while the contribution of the instrumental energy resolution (δE ~0.6 keV, estimated from the shape of Si leading edge) and the energy

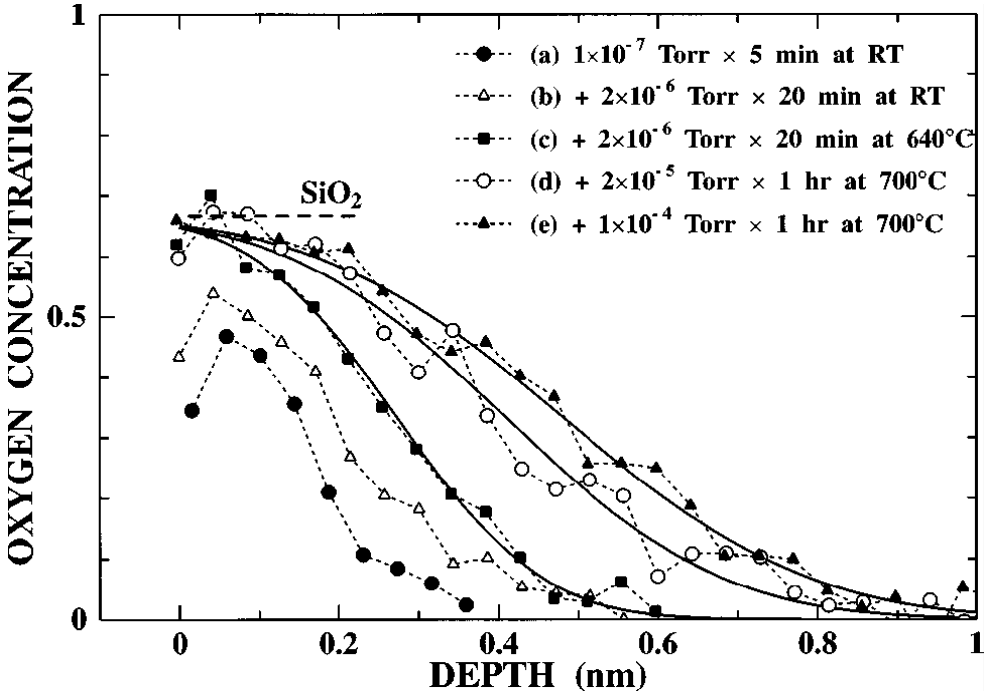

Fig. 6.2 Oxygen depth profiles observed during the initial oxidation process. Formation of stoichiometric SiO_2 layer is seen after oxidation at 640°C. The profile moves to deeper region without a significant shape change, indicating the layer-by-layer growth mode.

loss straggling is much smaller (estimated σ is about 0.12 nm with Lindhard formula [19] and about 0.13 nm with Yang formula [20] including δE). This indicates the existence of a compositional transition layer of σ ~0.3 nm [21] in the SiO_2/Si(001) interface in accordance with the recent theoretical studies by Pasquarello *et al.* [22], and Ng and Vanderbilt [23]. Using first-principles molecular dynamics, they found a transition layer of ~0.5 nm thickness having stoichiometry close to SiO [22].

Careful analysis of the HRBS spectra observed during the sequential isotopic oxidation allows us to deduce more detailed information. There were several theoretical studies about the initial oxidation process [9,13-15,24]. A scenario for laterally uniform oxidation of the first layer was proposed by Uchiyama *et al.* [15]: After one BB site of each down dimmer atom is occupied at θ = 0.5 ML, 0.5 ML of oxygen atoms occupy the dimer-bridge (DB) sites, and then the other BB sites of the down dimmer atoms are occupied by 0.5 ML of oxygen atoms at θ = 1.5 ML. Demkov and Sankey proposed a ‘‘peeling’’ oxidation mechanism, which explains the layer-by-layer oxidation [24]. According to their model, dimer units having four oxygen atoms [one terminal oxygen, one oxygen atom in the DB site and two oxygen atoms in the BB sites] are formed in the first layer oxidation, opening a channel for the second layer oxidation. The tendency for oxygen agglomeration was observed by infrared spectroscopy [25] and also by ultraviolet photoemission spectroscopy [26]. IR absorption spectroscopy revealed formation of surface silicon epoxide structures that contain 3–5 oxygen atoms in single dimer units [one oxygen atom in the

on-dimer (OD) site and 2–4 atoms in the BB sites] [25]. Based on *ab initio* quantum chemical cluster calculations, the epoxides were found to be the thermodynamically favored product [25]. Observed HRBS spectra are compared with these three models.

Figure 6.3(a) shows the background subtracted oxygen spectra observed after 5 min oxidation at RT under $^{16}O_2$ gas pressure of 1×10^{-7} Torr. The oxygen coverage is estimated to be 0.95±0.2 ML. The calculated spectra are also shown for comparison. These spectra were calculated as a sum of the contributions from individual sites, which were assumed to be given by Gaussians. For example, dotted curves show the individual contributions for the epoxide model, i.e., the contribution of the OD site (small peak) and that of the BB site [an epoxide structure containing five oxygen atoms, $(O_2)SiØSi(O_2)$, was employed]. The peak energy E_p of the individual contribution was calculated as

$$E_p = K\left(E_0 - \sum_{i=Si,O}\frac{S(i)\left[N(i)+n(i)/2\right]}{\cos\theta_i}\right) - \sum_{i=Si,O}\frac{S'(i)\left[N(i)+n(i)/2\right]}{\cos\theta_e}, \qquad (6.1)$$

where K is the kinematic factor for He-O scattering, E_0 is the incident energy, $N(i)$ is the area density of i species (i = Si,O) located higher than the relevant oxygen site, $n(i)$ is that located at the same height as the relevant oxygen site [27], $S(i)$ and $S'(i)$ are the stopping cross sections of i species for He ions before and after scattering, respectively, and θ_i (θ_e) is the incident (exit) angle. The peak width was calculated from the instrumental energy resolution (δE ~0.6 keV) as well as the energy-loss straggling estimated with the Lindhard formula [19]. The calculated spectra

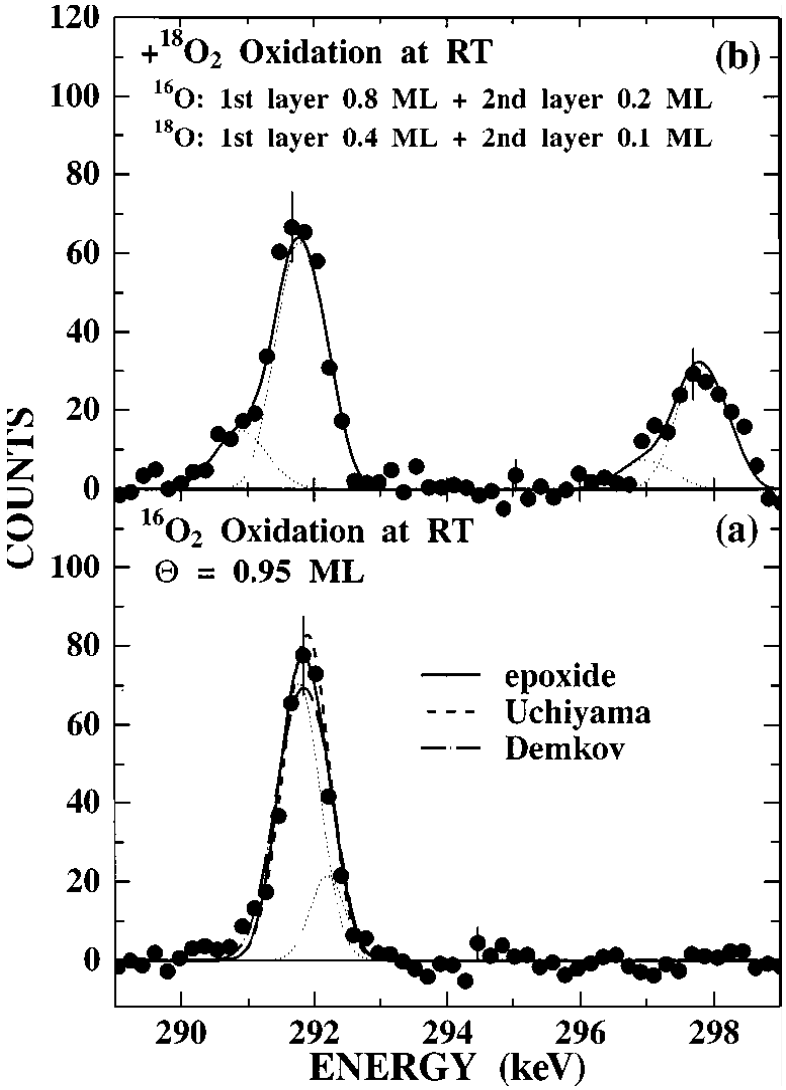

Fig. 6.3 HRBS spectra observed in sequential isotopic oxidation. Oxidation conditions were (a) 5 min under $^{16}O_2$ gas pressure of 1×10^{-7} Torr at RT; and (b) additional 20 min oxidation under $^{18}O_2$ gas pressure of 2×10^{-6} Torr at RT. Simulated spectra with various oxidation models are shown by curves (a). Typical error bars are also shown.

for various oxidation models are almost the same. Although the epoxide model gives a slightly better fit, the results of other models can be improved if the instrumental energy resolution is changed by ~10%, indicating that a definite judgment on these three models is difficult. It is,

however, clear that the oxygen atoms are predominantly incorporated in the first atomic layer at this stage of oxidation (the amount of the second layer oxygen was estimated to be less than 0.1 ML using the fitting procedure described below).

An additional oxidation by $^{18}O_2$ gas was performed at RT (2×10^{-6} Torr, 20 min). Figure 6.3(b) shows the observed HRBS spectrum. The ^{16}O peak becomes broader and shows a shoulder at ~291 keV while the yield is almost the same as before. This indicates that some ^{16}O atoms move into deeper layers during the additional oxidation.

The observed spectrum was fitted by simulated spectrum taking account of the oxidation of deeper layers. The best-fitted result is shown by a solid curve. The contributions of individual layers are shown by dotted curves. In the simulation, we employed the epoxide model [(O_2)SiØSi(O_2)] for the first layer oxidation and the oxygen atoms incorporated in the second layer were assumed to be at the same height as the second layer silicon atoms. The amount of ^{16}O (^{18}O) atoms in the first layer is found to be 0.8 (0.4) ML and that in the second layer is 0.2 (0.1) ML, showing that 0.1–0.2 ML of ^{16}O atoms move from the first layer into the second layer during the additional oxidation at RT. The present result indicates that most oxygen atoms in the second layer are not directly incorporated at RT. They were incorporated in the first layer before coming to the second layer. The observed second layer oxygen fraction increases very rapidly from < 10% to 20% when the oxygen coverage increases from 0.95 to 1.5 ML. This suggests that surface oxide structures containing more than three oxygen

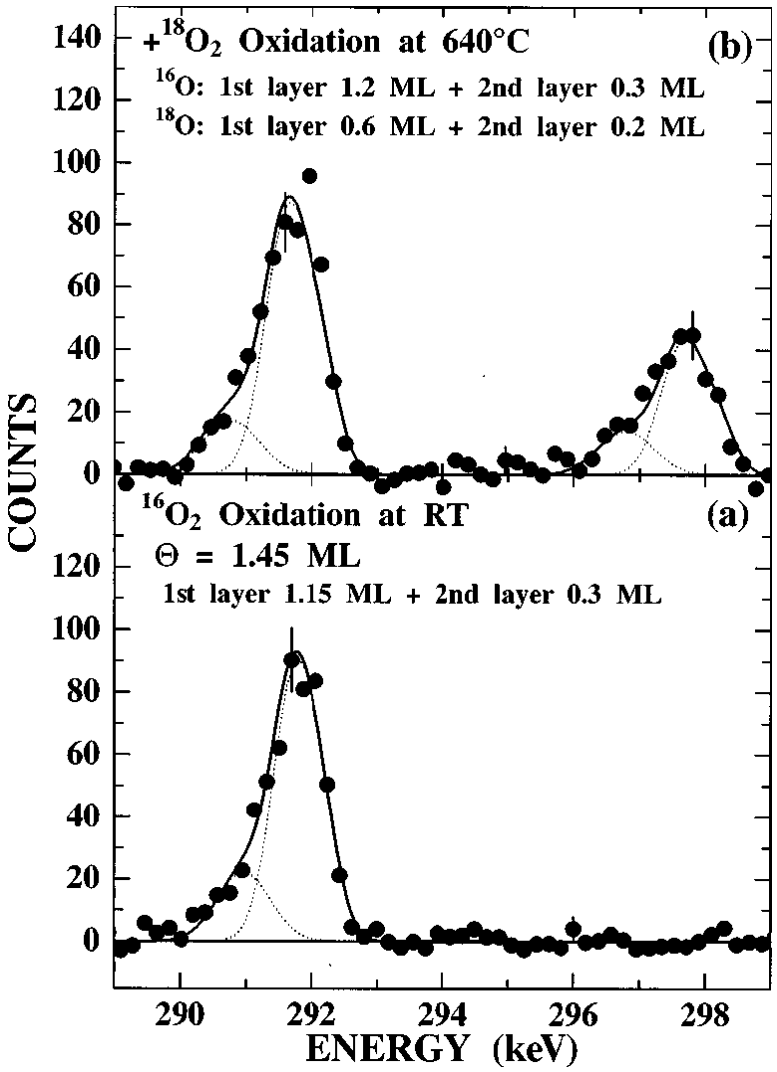

Fig. 6.4 HRBS spectra observed in sequential isotopic oxidation. Oxidation conditions were (a) 20 min under $^{16}O_2$ gas pressure of 2×10^{-6} Torr at RT; and (b) additional 20 min oxidation under $^{18}O_2$ gas pressure of 2×10^{-6} Torr at 640°C. Simulated best-fitted spectra are also shown by solid curves. The dotted curves show the contributions from individual layers. Typical error bars are also shown.

atoms per dimer unit accelerate the second layer oxidation. Similar measurements were performed at elevated temperatures. Figure 6.4 shows the result of the sequential oxidation, ^{16}O oxidation at RT (2×10^{-6} Torr, 20 min) followed by ^{18}O oxidation at 640°C (2×10^{-6} Torr, 20 min).

Surprisingly, ^{16}O distribution hardly changes during the additional oxidation at 640°C in contrast to the sequential oxidation at RT. Newly incorporated ^{18}O atoms distribute in both the first and second layers. The total amount of the first layer oxygen is 1.8 ML, indicating that the first layer is almost completely oxidized at this stage.

6.4 Conclusion

In summary, we have observed the initial oxidation process on Si(001) by high-resolution RBS. The coverage of oxygen is found to saturate at 1.45±0.2 and 2.3±0.3 ML at RT and 640°C, respectively. An almost stoichiometric SiO_2 layer is formed at 640°C, while a SiO-like layer is formed at RT. Oxygen atoms of ~0.3 ML are incorporated in the second layer before the first layer is completely oxidized even at RT. A part of these second layer oxygen atoms are not directly incorporated but via the first layer. On the contrary, oxygen atoms incorporated at RT does not change their distribution during the additional oxidation at 640°C. In the further oxidation at elevated temperatures, the oxidation proceeds basically in the layer-by-layer mode although there is a compositional transition layer of sub-nm thickness in the SiO_2/Si(001) interface.

References

[1] G. Timp, in *Proceedings of the 1998 International Electronic Devices Meeting (IEDM)* (IEEE, San Francisco, CA, 1998), Vol. 98, p. 615.

[2] H. Watanabe, K. Kato, T. Uda, K. Fujita, M. Ichikawa, T. Kawamura, K. Terakura, Phys. Rev. Lett. 80 (1998) 345.

[3] L.C. Feldman, P.J. Silverman, J.S. Williams, T.E. Jackman, I. Stensgaard, Phys. Rev. Lett. 41 (1978) 1396.

[4] A. Ourmazd, D.W. Taylor, J.A. Rantschler, J. Bauk, Phys. Rev. Lett. 59 (1987) 213.

[5] H. Akatsu, Y. Sumi, I. Ohdomari, Phys. Rev. B 44 (1991) 1616.

[6] E.P. Gusev, H.C. Lu, T. Gustafsson, E. Garfunkel, Phys. Rev. B 52 (1995) 1759.

[7] Y.P. Kim, S.K. Choi, H.K. Kim, D.W. Moon, Appl. Phys. Lett. 71 (1997) 3504.

[8] T. Uchiyama, M. Tsukada, Phys. Rev. B 53 (1996) 7917.

[9] K. Kato, T. Uda, K. Terakura, Phys. Rev. Lett. 80 (1998) 2000.

[10] P. Kliese, B. Röttger, D. Badt, H. Neddermeyer, Ultramicroscopy 42-44 (1992) 824.

[11] Ph. Avouris, D.G. Cahill, Ultramicroscopy 42-44 (1992) 838.

[12] H. Ikegami, K. Ohmori, H. Ikeda, H. Iwano, S. Zaima, Y. Yasuda, Jpn. J. Appl. Phys. 35 (1996) 1593.

[13] T. Uchiyama, M. Tsukada, Phys. Rev. B 55 (1997) 9356.

[14] H. Kageshima, K. Shiraishi, Phys. Rev. Lett. 81 (1998) 5936.

[15] T. Uchiyama, T. Uda, K. Terakura, Surf. Sci. 433-435 (1999) 896.

[16] K. Kimura, K. Ohshima, M. Mannami, Appl. Phys. Lett. 64 (1994) 2232.

[17] K. Nakajima, Y. Okazaki, K. Kimura, Jpn. J. Appl. Phys. 39 (2000) 4481.

[18] H. A. Enge, Rev. Sci. Instrum. 29 (1958) 885.

[19] J. Lindhard and M. Scharff, K. Dan, Viedensk. Selsk. Mat. Fys. Medd. 28 (1954) 8.

[20] Q. Yang, D.J. O'Connor, Z. Wang, Nucl. Instr. and Meth. B 61 (1991) 149.

[21] Taking account of the possible interface roughness, this is the upper limit.

[22] A. Pasquarello, M. S. Hybertsen, R. Car, Nature (London) 396 (1998) 58.

[23] K.-O. Ng, D. Vanderbilt, Phys. Rev. B 59 (1999) 10132.

[24] A.A. Demkov, O.F. Sankey, Phys. Rev. Lett. 83 (1999) 2038.

[25] B.B. Stefanov, K. Raghavachari, Surf. Sci. 389 (1997) L1159.

[26] H.W. Yeom, H. Hamamatsu, T. Ohta, R.I.G. Uhrberg, Phys. Rev. B 59 (1999) R10413.

[27] The heights of oxygen sites were taken from Fig. 1 of Ref. 24, Fig. 2 of Ref. 25, and private communication with Dr. Uchiyama.

Chapter 7

Lattice distortion at SiO_2/Si(001) interface studied with high-resolution Rutherford backscattering spectroscopy/channeling

The growth-temperature dependence of the transition structure at the SiO_2/Si interface is studied by high-resolution Rutherford backscattering spectroscopy/channeling. A Si lattice distortion is found at the interface. Such distortion propagates more than 2 nm from the interface. It is shown that the SiO_2/Si grown by wet oxidation at 1100°C has a smaller lattice distortion than that grown at 900°C. This can be explained in terms of the relaxation of the strained SiO_2 network caused by the viscous flow of SiO_2 at high temperatures.

7.1 Introduction

With the downscaling of metal−oxide−semiconductor field-effect transistors (MOSFETs), the thickness of gate insulator films is approaching 1 nm. In this regime, the interface between SiO_2 and Si plays a crucial role in MOSFET performance [1,2]. For example, the carrier mobility is significantly affected by properties observed in the channel region just under the interface, particularly by lattice distortion. In this respect, control of lattice distortion at the interface is of prime importance. This is also the case even if SiO_2 is replaced with high-k materials in future microelectronic devices because a thin SiO_2 layer is intentionally formed between high-k films and Si.

A SiO_2 transition layer of about 1 nm thickness exists in thermally grown SiO_2 films [1,3]. In the transition layer, the SiO_2 network is believed to be compressed due to a large volume expansion upon oxidation [4]. Compressive strain, however, decreases when the thermal oxide is grown at temperatures higher than 1000°C [4,5]. This growth temperature dependence has been explained in terms of the viscous flow of SiO_2 [4,5].

The compressive stress in a SiO_2 transition layer may affect the Si lattice at the interface. Actually, there are several lines of evidence of Si lattice distortion in the SiO_2/Si interface [6-9]. According to the above-mentioned finding in the transition layer, it is expected that the amount of lattice distortion in the substrate Si is also reduced when the

SiO_2 film is grown at temperatures higher than 1000°C. In the present study, we investigate the growth temperature dependence of lattice distortion using high-resolution Rutherford backscattering spectroscopy (RBS)/channeling. The amount of Si suboxide species at the interface is also discussed.

7.2 Experimental

Ultrathin (~1 nm) SiO_2 films were grown on p-type Czochralski (Cz-)Si(001) wafers by wet oxidation at 900 and 1100°C. Because the oxidation rate is very high at 1100°C, it is difficult to directly grow ultrathin SiO_2 films. We, therefore, first prepared a thick SiO_2 layer (~1 μm) at 1100°C and etched this thick SiO_2 layer with a dilute HF solution down to a thickness of about 1 nm. The prepared samples were measured using high-resolution RBS (HRBS). Details of the HRBS measurement were described elsewhere [10,11]. Briefly, a 400 keV He^+ ion beam generated by an accelerator was collimated by two 4-jaw slit systems to 2 × 2 mm^2. The divergence angle of the ion beam was less than 2 mrad. The beam was incident on the specimen mounted on a high-precision goniometer in a UHV chamber. The He^+ ions that scattered from the specimen were analyzed of their energy using a 90° sector magnetic spectrometer and detected by a one-dimensional position-sensitive detector.

7.3 Results and discussion

Figure 7.1 shows an example of the HRBS spectrum for the SiO_2/Si(001) grown at 900°C observed under [110] channeling conditions. There are two peaks corresponding to silicon (~355 keV) and oxygen (~332 keV) in the spectrum. The amount of O atoms Y_O in the SiO_2 film was obtained to be 5.76×10^{15} atoms/cm^2 from the observed oxygen peak using a random spectrum (not shown) as reference. The error in Y_O was estimated to be ~5%, which mainly comes from the uncertainty of stopping power. If a stoichiometric SiO_2 layer was formed, the amount of Si atoms in the SiO_2 layer would be $Y_O/2 = 2.88\times10^{15}$ atoms/cm^2 (the thickness of the SiO_2 layer is about 1.2 nm). The amount of Si atoms observed with the channeling ions, however, is much larger, i.e., 7.34×10^{15} atoms/cm^2. This large difference can be ascribed to (i) the so-called interface peak, (ii) Si atoms in the suboxide state and (iii) lattice distortion.

The contribution of the interface peak was estimated by ion scattering simulation. In the simulation, Molière potential was employed for the ion-atom interaction potential and the thermal vibration amplitude of 6.5 pm, calculated at a Debye temperature of 645 K, was used. The total yield of the interface peak for the ideal Si lattice was determined to be 2.67×10^{15} atoms/cm^2. Using this result, the HRBS spectrum was calculated. In the calculation, the semi-empirical formula for energy loss straggling reported by Yang et al. [12] was used. The calculated spectrum is shown as a dashed curve in Fig. 7.1. Although the agreement between the observed

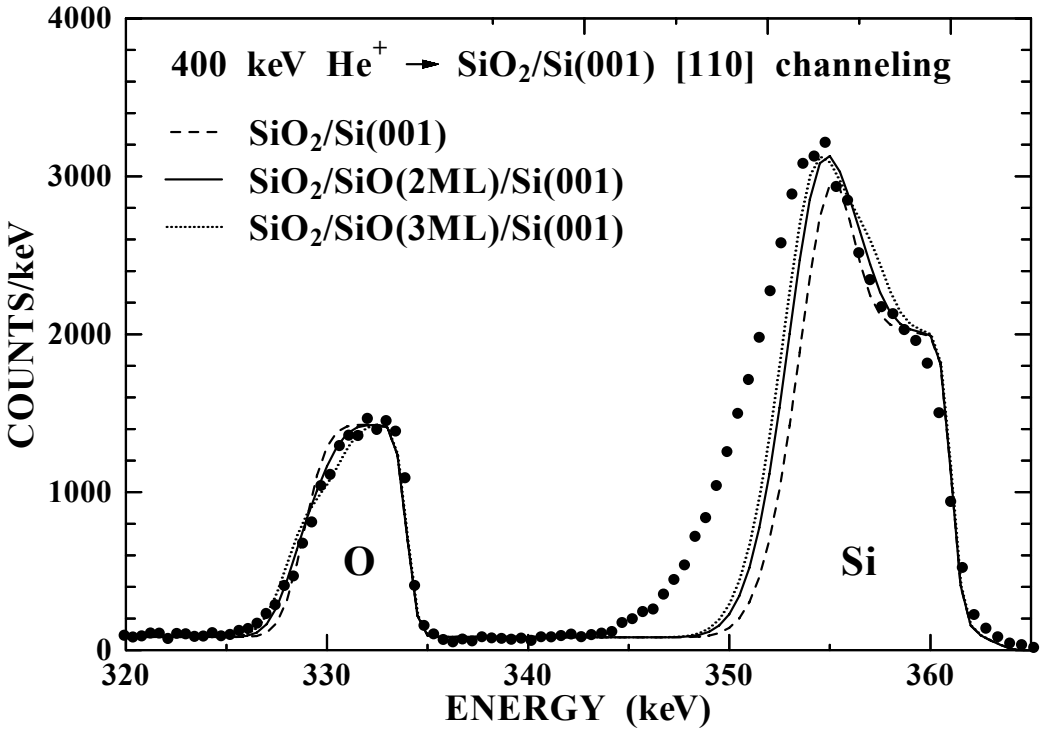

Fig. 7.1 High-resolution RBS spectrum of SiO_2 (1.2 nm)/Si(001) observed under the [110] channeling conditions. SiO_2/Si(001) was grown by wet oxidation at 900°C. The dashed curve shows the calculated spectrum of the ideal interface structure without Si lattice distortion. The solid and dotted curves show the calculated spectra of SiO_2/SiO/Si(001) structures without lattice distortion. Although the calculated spectrum reproduces the oxygen peak, there is a large difference in the Si peak between the spectra, indicating that the Si lattice is distorted at the interface.

and calculated oxygen peaks is reasonably good, there is a large difference between the observed and calculated Si peaks. The observed yield is much larger than the calculated one in the low energy part of the Si peak. The excess Si yield is estimated to be 1.79×10^{15} atoms/cm^2. This excess Si can be attributed to Si lattice distortion and/or suboxide Si atoms at the interface.

Excess Si yield was measured at different sample positions. The

average excess Si yield is obtained to be $1.7\pm0.1\times10^{15}$ atoms/cm^2. This is slightly smaller than the recent result of $\sim2\times10^{15}$ atoms/cm^2 observed under [100] channeling conditions [13]. This small difference can be explained by the fact that [100] channeling is more sensitive to the displacement of Si atoms than [110] channeling.

Excess Si yield was also measured for the SiO_2/Si grown at 1100°C. Figure 7.2 shows the excess Si yields measured at different positions on the sample. The measured SiO_2 layer thickness is also shown as a function of sample position. The thickness varies from 0.8 nm through 2.6 nm across the sample, showing that the prepared SiO_2 film was not uniform. This is because the growth and etching could not proceed in a perfect layer-by-layer mode, although the nonuniformity is very small compared with the thickness of the layer removed (~1 μm). The observed excess Si yield is almost constant in spite of the large variation in SiO_2 thickness. The observed excess Si yields are summarized in Table I. The excess Si yield for the SiO_2/Si grown at 1100°C is smaller than that for the SiO_2/Si grown at 900°C by ~30%. A recent X-ray photoelectron spectroscopy (XPS) study revealed that the amount of suboxide Si atoms in the SiO_2/Si interface is almost independent of the preparation conditions of the SiO_2 films [14]. Thus, the observed difference in excess Si yield can be attributed to the difference in lattice distortion.

Looking at the oxygen peak more closely, there is a small difference between the observed and simulated spectra in the trailing edge (see Fig. 7.1). This difference can be explained by the formation of a suboxide layer

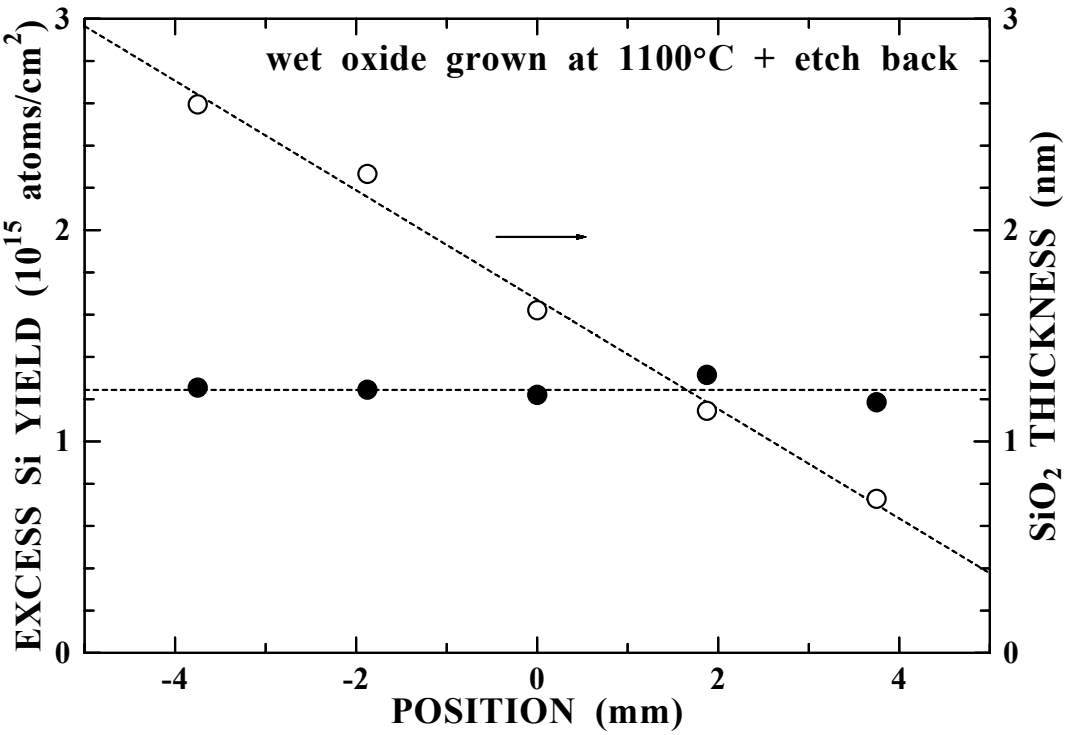

Fig. 7.2 Observed excess Si yield as function of sample position for ultrathin SiO_2/Si(001) prepared by etching in dilute HF solution after growth of SiO_2 layer of about 1 mm thickness at 1100°C. The thickness of the SiO_2 layer is also shown by open circles. In spite of a large variation in SiO_2 thickness, the excess Si yield is almost constant.

in the SiO_2/Si(001) interface. HRBS spectra were calculated for SiO_2/SiO/Si(001) structures with various SiO thicknesses. Examples of the calculated spectra are shown in Fig. 7.1. The best-fit result was obtained when the suboxide Si is 2 ML (1 ML = 6.78×10^{14} Si atoms/cm^2) as shown by the solid curve. However, there is still a large difference between the observed and calculated Si peaks. This indicates that the excess Si is mainly attributed to lattice distortion. The observed scattering yield is larger than the calculated result down to ~345 keV, indicating that the lattice distortion propagates more than 2 nm from the interface. Note that

Table I Observed excess Si yields at SiO_2/Si(001) interface grown at 900 and 1100°C

Growth temperature (°C)	Excess Si yield (cm^{-2})
900	$1.7\pm0.1\times10^{15}$
1100	$1.24\pm0.08\times10^{15}$

the oxygen profile can also be reproduced without the suboxide layer if the SiO_2 layer is not uniform. The obtained SiO layer thickness, that is 2 ML, is therefore the upper-bound suboxide layer thickness.

There has been considerable debate regarding the suboxide layer at the SiO_2/Si interface. Molecular dynamics simulation showed that the amount of Si suboxide species in the interface is 4.7 ML [15], which is far beyond the upper bound estimated here. There have been numerous experimental studies on the suboxide layer at the SiO_2/Si interface using XPS and photoelectron spectroscopy (PES). The thickness of the suboxide layer was estimated to be about 1 ML by XPS [1,14,16] and about 2 ML by PES [17-19]. Both results are consistent with the present result (~2 ML). Taking account of the effect of a possible nonuniformity of the SiO_2 layer, however, a 1 ML suboxide layer model, derived by XPS measurements, seems plausible.

7.4 Conclusion

In summary, Si lattice distortion at the SiO_2/Si interface is measured by HRBS/channeling. The observed silicon distortion for the SiO_2/Si grown at 1100°C is smaller than that grown at 900°C. This can be explained in terms of the viscous flow of SiO_2. Such a viscous flow releases the compressive strain in the SiO_2 transition layer at temperatures higher than 1000°C. As a result, the strain induced in the Si lattice is also reduced. The thickness of the suboxide layer in the interface is estimated to be less than 2 ML by the detailed analysis of the oxygen peak in the HRBS spectrum.

References

[1] T. Hattori, Crit. Rev. Solid State Mater. Sci. 20 (1995) 339.

[2] L.C. Feldman, in *Fundamental Aspects of Silicon Oxidation*, ed. Y.J. Chabal (Springer-Verlag, Berlin, 2001).

[3] Y. Watanabe, J. Electrochem. Soc. 145 (1998) 1306.

[4] Y. Sugita, S. Watanabe, N. Awaji, S. Komiya, Appl. Surf. Sci. 100-101 (1996) 268.

[5] S. Miyazaki, H. Nishimura, M. Fukuda, L. Ley, J. Ristein, Appl. Surf. Sci. 113−114 (1997) 585.

[6] L.C. Feldman, P.J. Silverman, J.S. Williams, Phys. Rev. Lett. 41 (1978) 1396.

[7] W. Daum, H.-J. Krause, U. Reichel, H. Ibach, Phys. Rev. Lett. 71 (1993) 1234.

[8] N.V. Nguyen, D. Chandler-Horowitz, P.M. Amirtharai, J.G. Pellegrino, Appl. Phys. Lett. 64 (1994) 2688.

[9] Y.P. Kim, S.K. Choi, H.K. Kim, D.W. Moon, Appl. Phys. Lett. 71 (1997) 3504.

[10] K. Kimura, K. Ohshima, M. Mannami, Appl. Phys. Lett. 64 (1994) 2232.

[11] K. Kimura, S. Joumori, Y. Oota, K. Nakajima, M. Suzuki, Nucl. Instr. and Meth. B 219−220 (2004) 351.

[12] Q. Yang, D.J. O'Connor, Z. Wang, Nucl. Instr. and Meth. B 61 (1991)

149.

[13] A. Bongiorno, A. Pasquarello, M.S. Hybertsen, L.C. Feldman, Phys. Rev. Lett. 90 (2003) 186101.

[14] M. Shioji, T. Shiraishi, K. Takahashi, H. Nohira, K. Azuma, Y. Nakata, Y. Takata, S. Shin, K. Kobayashi, T. Hattori, Appl. Phys. Lett. 84 (2004) 3756.

[15] K.-O. Ng, D. Vanderbilt, Phys. Rev. B 59 (1999) 10132.

[16] P.J. Grunthaner, M.H. Hecht, F.J. Grunthaner, N.M. Johnson, J. Appl. Phys. 61 (1987) 629.

[17] F.J. Himpsel, F.R. McFeely, A. Taleb-Ibrahimi, J.A. Yarmoff, G. Hollinger, Phys. Rev. B 38 (1988) 6084.

[18] F. Rochet, C. Poncey, G. Dufour, H. Roulet, Ch. Guillot, F. Sirotti, J. Non-Cryst. Solids 216 (1997) 148.

[19] J.H. Oh, H.W. Yeom, Y. Hagimoto, K. Ono, M. Oshima, N. Hirashita, M. Nywa, A. Toriumi, Phys. Rev. B 63 (2001) 205310.

Chapter 8

Characterization of HfO_2/Si(001) interface with high-resolution Rutherford backscattering spectroscopy

Characterization of a HfO_2(3 nm)/Si(001) interface prepared by atomic-layer chemical vapor deposition has been performed with high-resolution Rutherford backscattering spectroscopy (HRBS). Strain depth profile in the interface region has been measured with a combination of HRBS and channeling technique. It is found that a thin interface SiO_x layer lies between the HfO_2 film and the Si(001) substrate, and that compressive strain in the direction perpendicular to the surface is present in the Si(001) substrate near the SiO_x/Si(001) interface. The observed maximum strain is about 1% at the interface and the strained region extends down to ~3 nm from the interface.

8.1 Introduction

Metal-oxide-semiconductor field effect transistors (MOSFETs) are key components in silicon microelectronics technology. SiO_2 film has been used almost exclusively as gate dielectrics because the interface between SiO_2 and Si(001) is very abrupt and smooth, and SiO_2 film is thermodynamically stable in contact with silicon. With rapid downscaling of MOSFETs, however, we have encountered a fundamental limit of SiO_2 as gate dielectrics. The thickness of the SiO_2 film for sub-100 nm MOSFETs should be less than ~2 nm, resulting in high leakage current through the SiO_2 film. To reduce the gate leakage current while maintaining the area capacitance density of MOSFETs, a number of metal oxides or silicates with higher dielectric constant have been investigated as possible alternative to SiO_2 [1,2]. Among those materials, HfO_2 is one of most promising candidates to replace SiO_2 as gate dielectrics because of the high stability against thermal treatments on silicon [3]. However, the interface structure of HfO_2/Si(001) has not been characterized extensively in contrast to that of SiO_2/Si(001). In this chapter, we report strain depth profiling of the HfO_2/Si(001) interface using high-resolution Rutherford backscattering spectroscopy (HRBS) in combination with channeling technique.

8.2 Experimental

A ultrathin HfO_2 film ~3 nm thick was prepared on p-type Si(001) by means of atomic-layer chemical vapor deposition (ALCVD) at 300°C. The surface of Si(001) was pre-cleaned by HF vapor in situ before the deposition. As a metal precursor and oxygen source, $HfCl_4$ and H_2O were used, respectively. The HfO_2 film was expected to be amorphous since it had undergone no post-annealing. The HfO_2/Si(001) interface was observed ex situ with HRBS. The details of the HRBS setup are described elsewhere [4]. Briefly, a beam of 400 keV He^+ ions was collimated to 2 mm × 2 mm and to a divergence angle less than 1 mrad. The beam was incident on the HfO_2/Si(001) sample which is mounted on a high-precision five-axis goniometer installed in an UHV chamber. Energy spectra of He^+ ions scattered at 50° were measured by a high-resolution magnetic spectrometer (energy resolution ~1×10^{-3}, acceptance angle 0.4 msr) in combination with a one-dimensional position-sensitive detector (energy window 25%).

8.3 Results and discussion

Figure 8.1 shows an example of the observed HRBS spectrum. There are a prominent hafnium peak at ~390 keV and an oxygen peak at ~330 keV superimposed on a step with a leading edge at ~350 keV corresponding to the Si substrate. A small peak at ~360 keV is attributed to Cl contamination, which may originate from the $HfCl_4$ precursor. Depth profile of Hf, Si, O and Cl atoms were derived from the observed HRBS spectrum as shown in Fig. 8.2. A solid line shows twice the Hf concentration. The Hf concentration is nearly half of the oxygen concentration in the surface region (< 2 nm), which proves that an almost

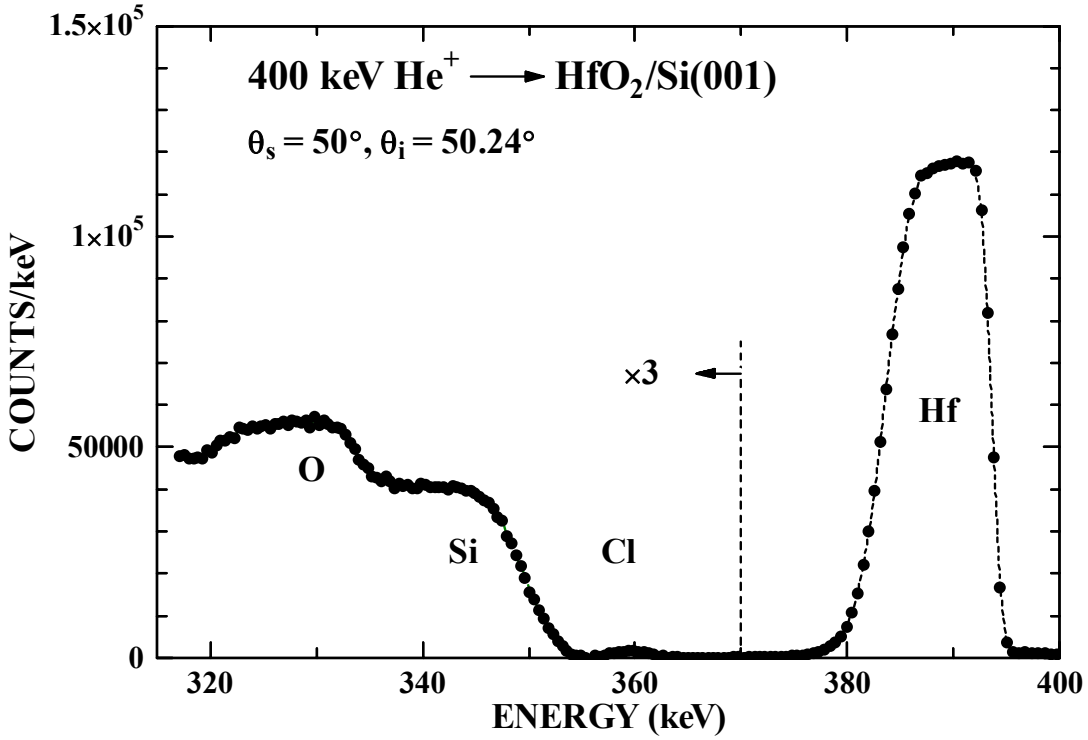

Fig. 8.1 HRBS spectrum of HfO_2/Si(001) for the incidence of 400 keV He^+ ions. The scattering angle is 50° and the angle of incidence is 50.24° from the normal direction to the surface.

stoichiometric HfO_2 film was formed by ALCVD. However, there are excess oxygen atoms in the interface region, showing formation of a thin SiO_x (~1 nm) layer between the HfO_2 film and the Si(001) substrate.

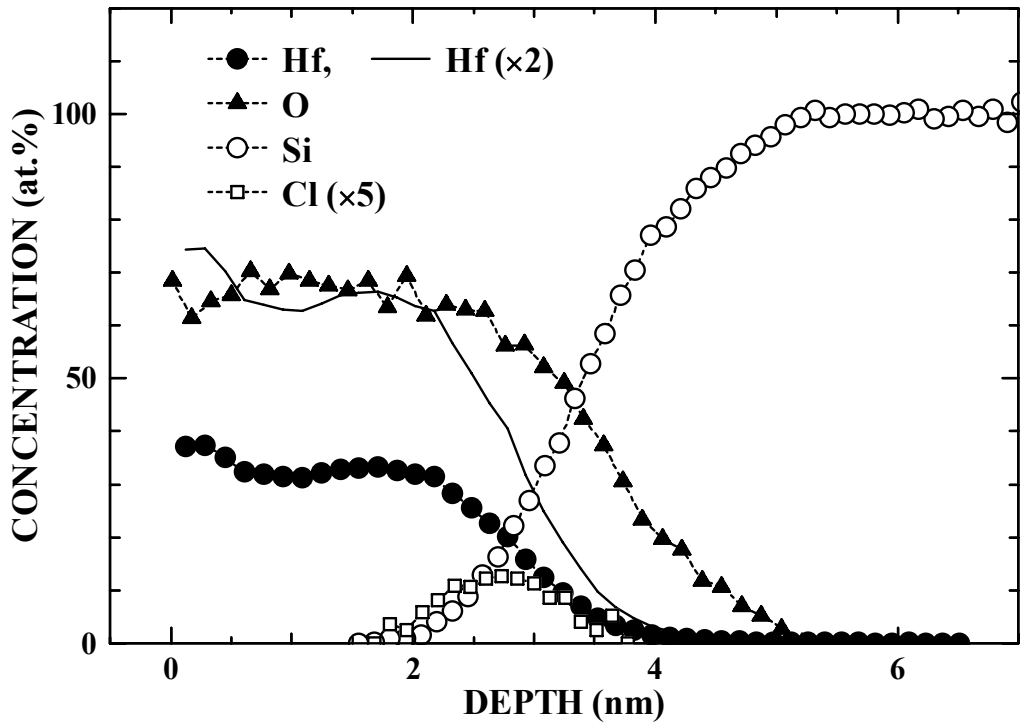

Fig. 8.2 Depth profiles of Hf, Si, O and Cl (×5) atoms in HfO_2/Si(001) derived from the observed HRBS spectrum. The solid curve shows twice the Hf concentration.

An angular scan of incidence was performed around a [111] axis of the Si(001) substrate at a fixed azimuth to measure strain in the Si substrate near the SiO_x/Si(001) interface. Figure 8.3 shows some observed HRBS spectra at various angles of incidence. Scattering yield from the Si(001) substrate changes dramatically with the angle of incidence and is lowest at the angle coinciding with the [111] axis of the Si(001) substrate. The

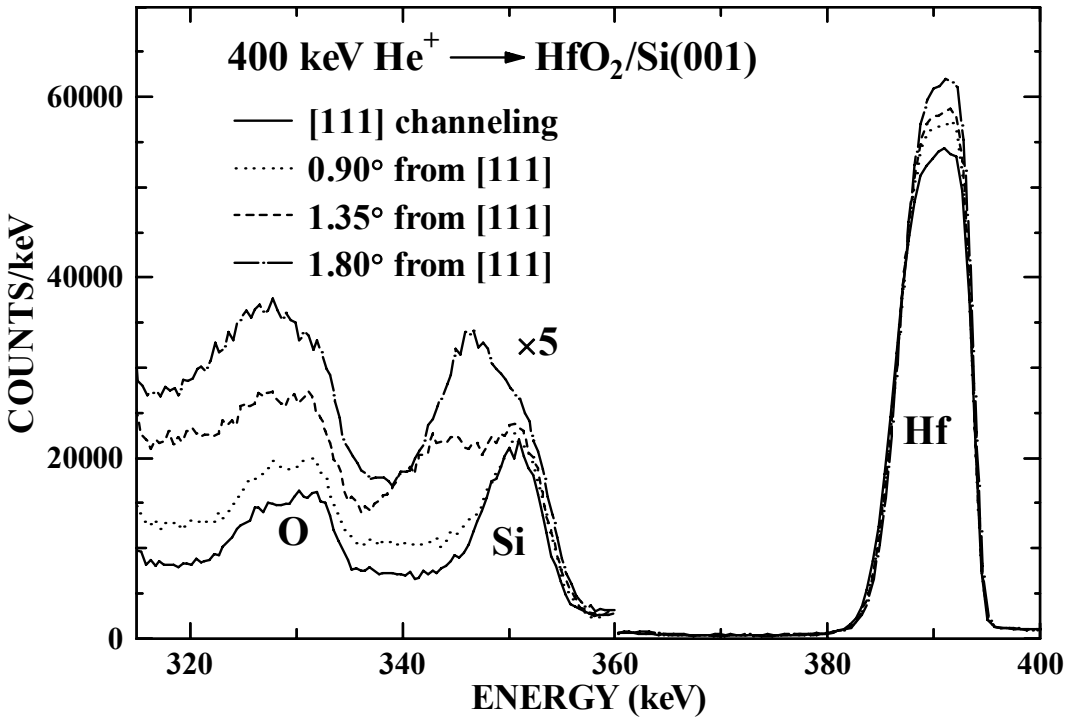

Fig. 8.3 HRBS spectra at various angles of incidence around the [111] direction of the Si(001) substrate. Scattering yield from the Si(001) substrate changes dramatically with the angle of incidence and is lowest at the angle coinciding with the [111] direction.

observed HRBS spectra were divided into a number of strips corresponding to depth windows of 0.5 nm, and scattering yield from the individual depth regions was obtained as a function of the angle of incidence from the [111] direction. Figure 8.4 shows the results for various depth regions measured from the HfO_2/SiO_x interface. A so-called channeling dip of scattering yield can be observed around the [111] direction except for very shallow depth region which correspond to the SiO_x layer (curve A). Although the position of the channeling dip for deeper region coincides with the bulk [111] axis (curve F), that for shallower region shifts toward larger angle of incidence. The shift should be caused by bending of the [111] axis near the

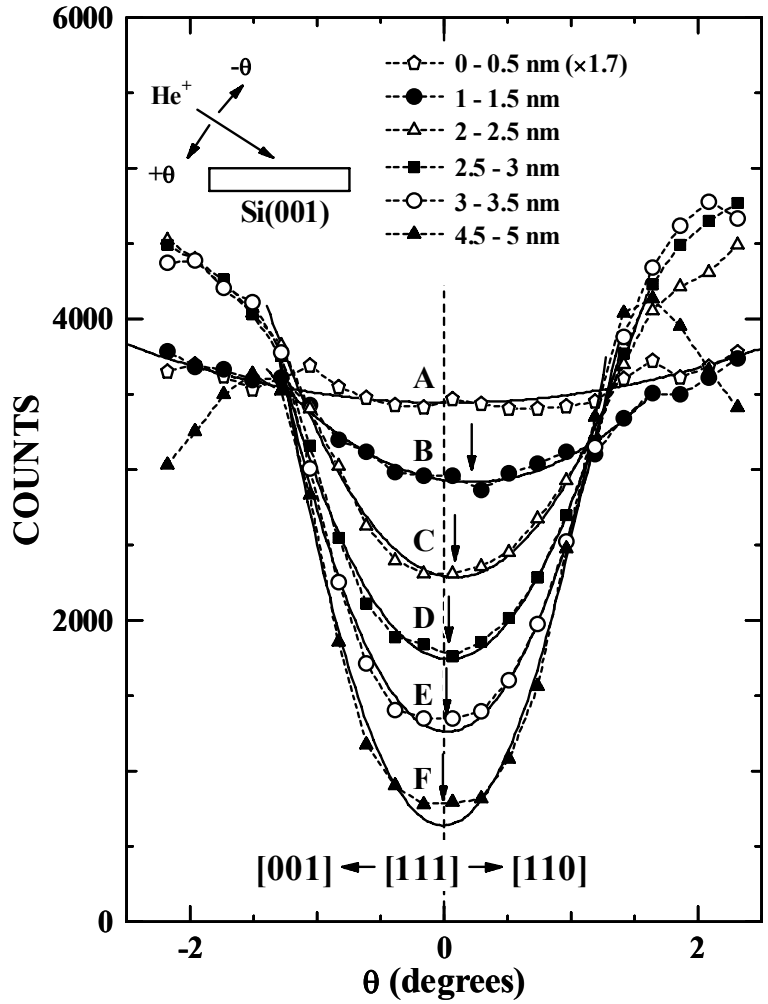

Fig. 8.4 Scattering yields from various depth regions in the Si(001) substrate as a function of the angle of incidence around the [111] direction. The depth is measured from the HfO_2/SiO_x interface. The channeling dip shifts toward larger angle of incidence for shallower region.

SiO_x/Si(001) interface due to compressive strain of Si lattice in the direction perpendicular to the surface.

Figure 8.5 shows the observed angular shift of the channeling dip as a function of depth from the surface. The axis on the right shows the local compressive strain estimated by

$$\varepsilon = 1 - \frac{\tan\theta_i}{\tan(\theta_i + \Delta\theta_i)} = \frac{2\Delta\theta_i}{\sin 2\theta_i} \quad (for\ \Delta\theta_i << 1), \tag{8.1}$$

where θ_i = 54.74° is the angle of incidence for [111] channeling and $\Delta\theta_i$ (rad) the observed angular shift. Again we remark that the angular shift $\Delta\theta_i$ is fully assigned to the local strain in the direction perpendicular to the surface in Eq. (8.1), because no enhancement of the scattering yield due to edge dislocations, which a uniform lateral strain would produce between the strained layer and the bulk crystal, was observed in the channeling spectrum. The observed compressive strain is about 1% near the SiO_x/Si(001) interface. The strain decreases rapidly with increasing depth and becomes smaller than the present detection limit (~0.1%) at depth more than ~3 nm from the SiO_x/Si(001) interface.

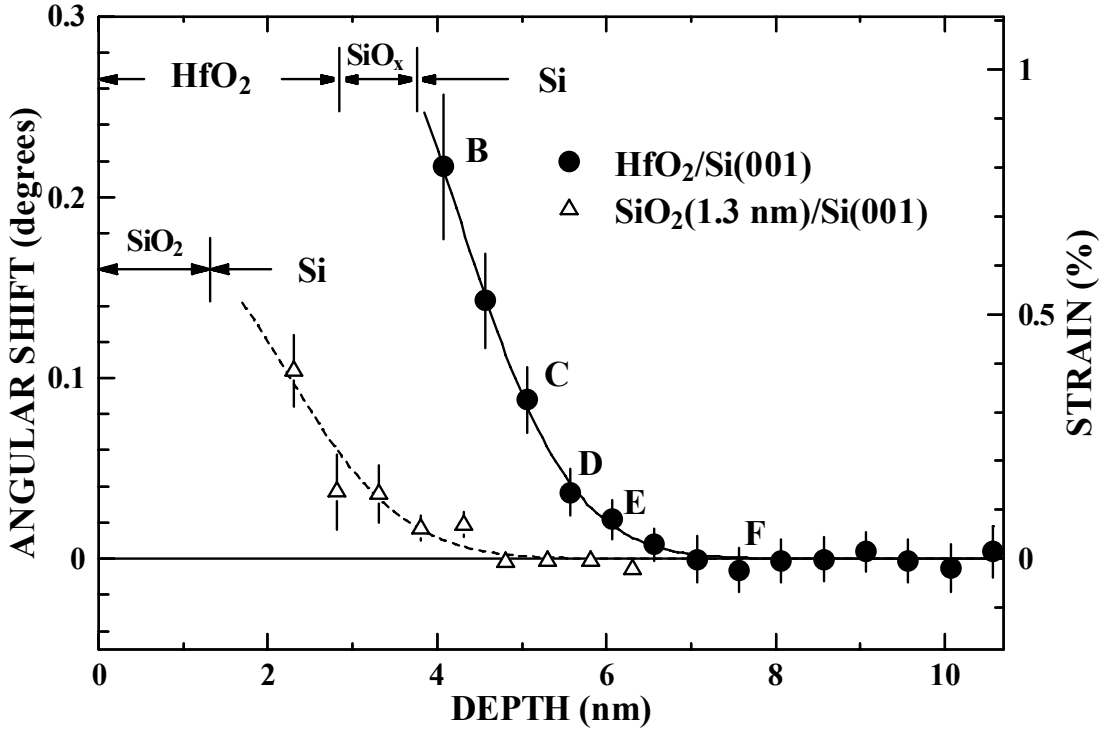

Fig. 8.5 Angular shift of the channeling dip as a function of depth from the surface. The axis on the right shows the local compressive strain estimated from the observed angular shift with Eq. (8.1). Triangles show the result of our recent measurement for a SiO_2(1.3 nm)/Si(001) interface.

There are some experimental evidences of a strained Si layer near the SiO_2/Si(001) interfaces [5-8]. Measurements of optical second-harmonic generation spectra of oxidized Si suggested existence of a thin strained layer with expansion of Si–Si bond lengths close to the interface [6]. Spectroscopic ellipsometry also revealed the existence of a strained Si layer at the SiO_2/Si(001) interface [7]. Triangles in Fig. 8.5 show the result of our recent measurement for a SiO_2 (1.3 nm)/Si(001) interface. A compressive strain perpendicular to the surface was also observed in the Si substrate near the SiO_2/Si(001) interface. The strain depth profiles for both the samples in Fig. 8.5 are similar in the dependence on the depth from the SiO_x/Si(001) or SiO_2/Si(001) interface, respectively. Considering the formation of the thin SiO_x layer at the interface in the present HfO_2/Si(001) sample, the observed strain for the HfO_2/Si(001) could be related to the strained Si layer observed at the SiO_2/Si(001) interface.

8.4 Conclusion

The interface of HfO_2/Si(001) grown by ALCVD was characterized by HRBS. A thin SiO_x layer was found to lie between the HfO_2 film and the Si(001) substrate. Strain depth profiling of the Si(001) substrate near the interface was performed by HRBS/channeling. The channeling dip of scattering yield from the Si substrate near the interface of SiO_x/Si(001) was shifted toward larger angle of incidence, indicating the existence of compressive strain in the direction perpendicular to the surface. The observed maximum strain was about 1% at the interface between the SiO_x layer and the Si(001) substrate. The strain decreases rapidly with increasing depth and becomes smaller than the detection limit (~0.1%) at depth more than ~3 nm from the SiO_x/Si(001) interface. The strain could be associated with the formation of the SiO_x layer between the HfO_2 film and the Si(001) substrate.

References

[1] E.P. Gusev, M. Copel, E. Cartier, I.J.R. Baumvol, C. Krug, M.A. Gribelyuk, Appl. Phys. Lett. 76 (2000) 176.

[2] J.-P. Maria, D.Wicaksana, A.I. Kingon, B. Busch, H. Schulte, E. Garfunkel, T. Gustafsson, J. Appl. Phys. 90 (2001) 3476.

[3] M. Gutowski, J.E. Jaffe, C.-L. Liu, M. Stoker, R.I. Hegde, R.S. Rai, P.J. Tobin, Appl. Phys. Lett. 80 (2002) 1897.

[4] K. Kimura, K. Ohshima, M. Mannami, Appl. Phys. Lett. 64 (1994) 2232.

[5] L.C. Feldman, P.J. Silverman, J.S.Williams, Phys. Rev. Lett. 41 (1978) 1396.

[6] W. Daum, H.-J. Krause, U. Reichel, H. Ibach, Phys. Rev. Lett. 71 (1993) 1234.

[7] N.V. Nguyen, D. Chandler-Horowitz, P.M. Amirtharai, J.G. Pellegrino, Appl. Phys. Lett. 64 (1994) 2688.

[8] Y.P. Kim, S.K. Choi, H.K. Kim, D.W. Moon, Appl. Phys. Lett. 71 (1997) 3504.

Chapter 9

Closing remarks
– Recent approaches to improve high-resolution RBS –

Even today, nearly 20 years after high-resolution RBS was successfully applied in studies on solid surfaces for the first time, it is still one of most reliable technieques for compositional depth profiling because of its high accuracy. This advantage is due largely to its straightforward principle based on approximately-single classical ion-atom elastic collisions. Besides, authoritative data of stopping cross sections available for large combinations of projectile ions and target atoms also lead to quantitative reliability of high-resolution RBS. In the future, therefore, high-resolution RBS will remain a standard technique for compositional depth profiling in growing nanoscale technology. However, further improvement should be achieved for high-resolution RBS to provide advanced analysis and to gain more users besides researchers.

First, downsizing of the ion accelerator and the spectrometer, as well as shorter measurement time is essential to improve usability, for example, for on-line check of quality of products in a factory. Dr. Ichihara of Kobe Steel co. ltd. has developed compact cyclotron RBS apparatus (1.8 m wide × 1.4 m long × 2.5 m high) including a 500 kV vertical ion accelerator and a spectrometer with larger acceptance angle and demonstrated the analysis of a sample of HfO_2(2.2 nm)/SiO_2(4.5 nm)/Si with depth resolution of 4.3 nm [1,2].

Second, (high-resolution) RBS can not provide information of chemical states of the constituent elements, which is often required to understand the behavior of the films in detail, such as stability of a gate dielectric film in oxidizing ambient. This drawback of high-resolution RBS

can be avoided in combination with other techniques. Precise depth profiling of chemical states has been demonstrated in combination with angle-resolved XPS (AR-XPS), where the elemental depth profiles obtained by high-resolution RBS are used as constrained conditions in depth profiling from AR-XPS measurements [3].

Moreover, even high-resolution RBS has no high resolution in the lateral direction because it usually adopts ion beam of several mm^2 as primary ions. Although several RBS measurements with a focused MeV ion micro-beam (micro-RBS) have recently reported [4,5], the depth resolution of these measurements was limited to several tens nanometers as well as for conventional RBS. RBS with high-resolution in both lateral and depth directions would be a stronger analysis technique for miniaturizing electronic devices with nanoscale dimensions or other laterally non-uniform specimens.

References

[1] C. Ichihara, A. Kobayashi, K. Inoue, K. Kimura, Nucl. Instr. and Meth. B 229 (2005) 527.

[2] C. Ichihara, Doctor thesis..

[3] K. Kimura, K. Nakajima, M. Zhao, H. Nohira, T. Hattori, M. Kobata, E. Ikenaga, J.J. Kim, K. Kobayashi, T. Conard, W. Vandervorst, Surf. Interface Anal. 40 (2008) 423.

[4] A. Simon, Z. Kántor, I. Rajta, T. Szörényi, Á.Z. Kiss, Nucl. Instr. and Meth. B 181 (2001) 360.

[5] A. Simon, Z. Kántor, Nucl. Instr. and Meth. B 190 (2002) 351.

LIST OF PUBLICATIONS

Publications concerning this thesis:

1. *The (111) surface of PbTe observed by high-resolution RBS*
   K. Nakajima, K. Kimura, M. Mannami
   Nucl. Instr. and Meth. B 135 (1998) 350.

2. *Direct observation of intermixing at Ge/Si(001) interfaces by high-resolution Rutherford backscattering spectroscopy*
   K. Nakajima, A. Konishi, K. Kimura
   Phys. Rev. Lett. 83 (1999) 1802.

3. *Intermixing at Ge/Si(001) interfaces studied by high-resolution RBS*
   K. Nakajima, A. Konishi, K. Kimura
   Nucl. Instr. and Meth. B 161-163 (2000) 452.

4. *Oxidation of Si(001) surfaces studied by high-resolution Rutherford backscattering spectroscopy*
   K. Nakajima, Y. Okazaki, K. Kimura
   Jpn. J. Appl. Phys. 39 (2000) 4481.

5. *Initial oxidation process of Si(001) studied by high-resolution Rutherford backscattering spectroscopy*
   K. Nakajima, Y. Okazaki, K. Kimura
   Phys. Rev. B 63 (2001) 113314.

6. *Strain profiling of HfO_2/Si(001) interface with high-resolution Rutherford backscattering spectroscopy*
   K. Nakajima, S. Joumori, M. Suzuki, K. Kimura, T. Osipowicz, K.L. Tok, J.Z. Zheng, A. See, B.C. Zhang
   Appl. Phys. Lett. 83 (2003) 296.

7. *Charge-state distribution of 400 keV He ions scattered from solid surfaces*

K. Nakajima, Y. Okura, M. Suzuki, K. Kimura
Nucl. Instr. and Meth. B 219–220 (2004) 514.

8. *Characterization of HfO_2/Si(001) interface with high-resolution Rutherford backscattering spectroscopy*
K. Nakajima, S. Joumori, M. Suzuki, K. Kimura, T. Osipowicz, K.L. Tok, J.Z. Zheng, A. See, B.C. Zhang
Appl. Surf. Sci. 237 (2004) 416.

9. *Lattice distortion at SiO_2/Si(001) interface studied with high-resolution Rutherford backscattering spectroscopy/channeling*
K. Nakajima, M. Suzuki, K. Kimura, M. Yamamoto, A. Teramoto, T. Ohmi, T. Hattori
Jpn. J. Appl. Phys. 45 (2006) 2467.

Publications concerning other studies:

1. *Observation of the PbSe(111) surface using high-resolution Rutherford backscattering spectroscopy*
K. Kimura, K. Nakajima, Y. Fujii, M. Mannami
Surf. Sci. 318 (1994) 363.

2. *Layer-by-layer growth of PbSe studied by glancing angle scattering of 500-keV protons*
Y. Fujii, K. Nakajima, K. Narumi, K. Kimura, M. Mannami
Surf. Sci. 318 (1994) L1225.

3. *Monolayer resolution in Rutherford backscattering spectroscopy*
K. Kimura, K. Ohshima, K. Nakajima, Y. Fujii, M. Mannami, H.-J. Gossmann
Nucl. Instr. and Meth. B 99 (1995) 472.

4. *A RHEED study of temperature dependence of homoepitaxy of SnTe(111)*
K. Nakajima,Y. Fujii, K. Kimura, M. Mannami

J. Cryst. Growth 158 (1996) 505.

5. *Oscillations of the intensity of scattered energetic ions from growing surface*
   K. Nakajima, Y. Fujii, K. Narumi, K. Kimura, M. Mannami
   in *Advances in the Understanding of Crystal Growth Mechanisms*, edited by T. Nishinaga *et al*., (North-Holland, Amsterdam, 1997) 309.

6. *Growth mode and defect generation in ZnSe heteroepitaxy on Te-terminated GaAs(001) surfaces*
   A. Ohtake, L.H. Kuo, T. Yasuda, K. Kimura, S. Miwa, T. Yao, K. Nakajima, K. Kimura
   J. Vac. Sci. Technol. B 15 (1997) 1254.

7. *Heterovalent ZnSe/GaAs Interfaces*
   T. Yao, F. Lu, M.W. Cho, K.W. Koh, Z. Zhu, L. H. Kuo, T. Yasuda, A. Ohtake, S. Miwa, K. Kimura, K. Nakajima, K. Kimura
   Phys. Stat. Sol. (b) 202 (1997) 657.

8. *Defect generation in layer-by-layer-grown ZnSe films on Te-terminated GaAs(001) surfaces*
   A. Ohtake, L.H. Kuo, K. Kimura, S. Miwa, T. Yasuda, C. Jin, T. Yao, K. Nakajima, K. Kimura
   Phys. Rev. B 57 (1998) 1410.

9. *Energy losses of B clusters transmitted through carbon foils*
   K. Narumi, K. Nakajima, K. Kimura, M. Mannami, Y. Saitoh, S. Yamamoto, Y. Aoki, H. Naramoto
   Nucl. Instr. and Meth. B 135 (1998) 77.

10. *Some applications of high-resolution RBS and ERD using a magnetic spectrometer*
    K. Kimura, K. Nakajima, M. Mannami
    Nucl. Instr. and Meth. B 136-138 (1998) 1196.

11. *Energy losses of MeV B clusters in solids*

K. Narumi, K. Nakajima, K. Kimura, M. Mannami, Y. Saitoh, S. Yamamoto, Y. Aoki, H. Naramoto
Mater. Chem. and Phys. 54 (1998) 229.

12. *Secondary-electron emission from specularly reflected MeV protons*
K. Kimura, S. Ooki, G. Andou, K. Nakajima, M. Mannami
Phys. Rev. A 58 (1998) 1282.

13. *Enhancement of the secondary-electron production process in front of insulator surfaces*
K. Kimura, G. Andou, K. Nakajima
Phys. Rev. Lett. 81 (1998) 5438.

14. *Hydrogen depth profiling with sub-nm resolution in high-resolution ERD*
K. Kimura, K. Nakajima, H. Imura
Nucl. Instr. and Meth. B 140 (1998) 397.

15. *Direct thermal fluorination of DLC surfaces*
Y. Hattori, K. Kobayashi, S. Kawasaki, F. Okino, K. Yanagiuchi, A. Tsuyoshi, M. Nakayama, K. Nakajima, K. Kimura, H. Touhara
Carbon 36 (1998) 1399.

16. *Preparation of smooth Si(001) surfaces by glancing angle sputtering*
K. Kimura, A. Fukui, K. Nakajima, M. Mannami
Nucl. Instr. and Meth. B 148 (1999) 149.

17. *Amorphization of Si(001) by ultra low energy (0.5±5 keV) ion implantation observed with high-resolution RBS*
K. Kimura, A. Agarwal, H. Toyofuku, K. Nakajima, H.-J. Gossmann
Nucl. Instr. and Meth. B 148 (1999) 284.

18. *Position-dependent stopping power of low velocity rare gas atoms at a SnTe(001) surface*
K. Nakajima, Y. Fukusumi, K. Kimura, M. Mannami, M. Yamamoto, S. Naito

Nucl. Instr. and Meth. B 149 (1999) 31.

19. *Secondary electron emission from surface channeled protons at a KCl(001) surface*
G. Andou, K. Nakajima, K. Kimura
Nucl. Instr. and Meth. B 160 (2000) 16.

20. *Secondary-electron emission by MeV He ions reflected from a SnTe(001) surface: Separation of above- and below-surface processes*
K. Kimura, S. Ooki, G. Andou, K. Nakajima
Phys. Rev. A 61 (2000) 012901.

21. *Secondary-electron emission by 0.5-MeV/u H, He, and Li ions specularly reflected from a SnTe(001) surface: Possibility of the surface track potential reducing the secondary-electron yield at a semiconductor surface*
K. Kimura, S. Usui, K. Nakajima
Phys. Rev. A 62 (2000) 062902.

22. *Characterization of ultra thin oxynitrides: A general approach*
B. Brijs, J. Deleu, T. Conard, H.De Witte, W. Vandervorst, K. Nakajima, K. Kimura, I. Genchev, A. Bergmaier, L. Goergens, P. Neumaier, G. Dollinger, M. Döbeli
Nucl. Instr. and Meth. B 161-163 (2000) 429.

23. *Stopping power of a KCl(001) surface for low energy Ne atoms*
K. Nakajima, S. Sonobe, K. Kimura
Nucl. Instr. and Meth. B 164-165 (2000) 553.

24. *Surface-plasmon-assisted secondary-electron emission from an atomically flat LiF(001) surface*
K. Kimura, G. Andou, K. Nakajima
Nucl. Instr. and Meth. B 164-165 (2000) 933.

25. *Nitrogen depth profiling in ultrathin silicon oxynitride films with high-resolution Rutherford backscattering spectroscopy*

K. Kimura, K. Nakajima, Y. Okazaki, H. Kobayashi, S. Miwa, K. Satori
Jpn. J. Appl. Phys. 39 (2000) 4663.

26. *Hydrogen depth-profiling in chemical-vapor-deposited diamond films by high-resolution elastic recoil detection*
K. Kimura, K. Nakajima, S.Yamanaka, M. Hasegawa, H. Okushi
Appl. Phys. Lett. 78 (2001) 1679.

27. *Oxidation of Si(001) observed by high-resolution RBS*
K. Kimura, K. Nakajima, Y. Okazaki
Nucl. Instr. and Meth. B 183 (2001) 166.

28. *Nitrogen profile in SiO_xN_y prepared by thermal nitridation of ozone oxide*
K. Nakajima, K. Kimura, A. Kurokawa, S. Ichimura, H. Fukuda
Jpn. J. Appl. Phys. 40 (2001) 4011.

29. *Anomalous surface amorphization of Si(001) induced by 3–5 keV Ar^+ ion bombardment*
K. Nakajima, H. Toyofuku, K. Kimura
Jpn. J. Appl. Phys. 40 (2001) 2119.

30. *Development of a new high-resolution RBS system*
K. Kimura, K. Nakajima
J. Surf. Surf. Soc. Jpn. (Hyomen kagaku) 22 (2001) 431 (in Japanese).

31. *Advanced characterization of high-k materials: A nuclear approach*
B. Brijs, C. Huyghebaert, S. Nauwelaerts, M. Caymax, W. Vandervorst, K. Nakajima, K. Kimura, A. Bergmaier, G. Döllinger, W.N. Lennard, G. Terwagne, A. Vantomme
Nucl. Instr. and Meth. B 190 (2002) 505.

32. *Hydrogen analysis of CVD homoepitaxial diamond films by high-resolution elastic recoil detection*
K. Kimura, K. Nakajima, S. Yamanaka, M. Hasegawa, H. Okushi
Nucl. Instr. and Meth. B 190 (2002) 689.

33. *Surface segregation of Ge during Si growth on Ge/Si(001) at low temperature observed by high-resolution RBS*
K. Nakajima, N. Hosaka, T. Hattori, K. Kimura
Nucl. Instr. and Meth. B 190 (2002) 587.

34. *Release of nitrogen from SiO_xN_y films during RBS measurement*
K. Kimura, K. Nakajima, H. Kobayashi, S. Miwa, K. Satori
Nucl. Instr. and Meth. B 190 (2002) 423.

35. *Ion scattering on crystalline surfaces: Effects of surface track potential on secondary electron emission*
Kenji Kimura, S. Usui, K. Maeda, K. Nakajima
Nucl. Instr. and Meth. B 193 (2002) 661.

36. *Energy loss of 15-keV Ar^{q+} (q = 1–3) ions reflected from a KCl(001) surface*
K. Nakajima, M. Nakamura, T. Tsujioka, K. Kimura
Nucl. Instr. and Meth. B 205 (2002) 705.

37. *SIMS and high-resolution RBS analysis of ultrathin SiO_xN_y films*
K. Kimura, K. Nakajima, , H. Kobayashi, S. Miwa, K. Satori
Appl. Surf. Sci. 203–204 (2003) 418.

38. *High-resolution depth profiling of ultrashallow boron implants in silicon using high-resolution RBS*
K. Kimura, Y. Oota, K. Nakajima, T.H. Büyüklimanli
Curr. Appl. Phys. 3 (2003) 9.

39. *Compositional transition layer in SiO_2/Si interface observed by high-resolution RBS*
K. Kimura, K. Nakajima
Appl. Surf. Sci. 216 (2003) 283.

40. *Molecular effect on projected range in ultralow-energy ion implantation*

K. Kimura, Y. Oota, K. Nakajima, M. Suzuki, T. Aoki, J. Matsuo, A. Agarwal, B. Freer, A. Stevenson, M. Ameen
Nucl. Instr. and Meth. B 211 (2003) 206.

41. *Depth profiling of ultra-shallow dopant with high-resolution Rutherford backscattering spectroscopy*
K. Kimura, Y. Oota, K. Nakajima, M. Suzuki
J. Vac. Soc. Jpn. 46 (2003) 767 (in japanese).

42. *Effects of surface track potential on secondary electron emission and surface stopping power*
K. Kimura, S. Usui, T. Tsujioka, S. Tanaka, K. Nakajima, M. Suzuki
Vacuum 73 (2004) 59.

43. *Auger neutralization rate for slow Ar^+ ions in front of KCl(001)*
K. Kimura, T. Tsujioka, S. Tanaka, A. Nakamoto, K. Nakajima, M. Suzuki
Phys. Rev. A 70 (2004) 022901.

44. *Composition, chemical structure, and electronic band structure of rare earth oxide/Si(100) interfacial transition layer*
T. Hattori, T. Yoshida, T. Shiraishi, K. Takahashi, H. Nohira, S. Joumori, K. Nakajima, M. Suzuki, K. Kimura, I. Kashiwagi, C. Ohshima, S. Ohmi, H. Iwai
Microelectronic Engineering 72 (2004) 283.

45. *Use of grazing angle sputtering for improving depth resolution in high resolution RBS*
W. Sakai, K. Nakajima, M. Suzuki, K. Kimura
Nucl. Instr. and Meth. B 219–220 (2004) 369.

46. *High-resolution RBS: a powerful tool for atomic level characterization*
K. Kimura, S. Joumori, Y. Oota, K. Nakajima, M. Suzuki
Nucl. Instr. and Meth. B 219–220 (2004) 351.

47. *Formation of iron silicide on Si(001) studied by high resolution*

Rutherford backscattering spectroscopy
K. Kinoshita, R. Imaizumi, K. Nakajima, M. Suzuki, K. Kimura
Thin Solid Films 461 (2004) 131.

48. *Atomic-scale depth profiling of composition, chemical structure and electronic band structure of La_2O_3/Si(100) interfacial transition layer*
H. Nohira, T. Shiraishi, K. Takahashi, T. Hattori, I. Kashiwagi, C. Ohshima, S. Ohmi, H. Iwai, S. Joumori, K. Nakajima, M. Suzuki, K. Kimura
Appl. Surf. Sci. 234 (2004) 493.

49. *Quality of SiO_2 and of SiGe formed by oxidation of $Si/Si_{0.7}Ge_{0.3}$ heterostructure using atomic oxygen at 400°C*
H. Nohira, T. Kuroiwa, M. Nakamura, Y. Hirose, J. Mitsui, W. Sakai, K. Nakajima, M. Suzuki, K. Kimura, K. Sawano, K. Nakagawa, Y. Shiraki, T. Hattori
Appl. Surf. Sci. 237 (2004) 134.

50. *Structure of ultrathin epitaxial CeO_2 films grown on Si(111)*
S. Joumori, K. Nakajima, M. Suzuki, K. Kimura, Y. Nishikawa, D. Matsushita, T. Yamaguchi, N. Satou
Jpn. J. Appl. Phys. 43 (2004) 7881.

51. *Direct formation of arrays of prolate Ag nanoparticles by dynamic oblique deposition*
M. Suzuki, W. Maekita, K. Kishimoto, S. Teramura, K. Nakajima, K. Kimura, Y. Taga
Jpn. J. Appl. Phys. 44 (2005) L193.

52. *Radiation damage induced by 5 keV Si^+ ion implantation in strained-$Si/Si_{0.8}Ge_{0.2}$*
T. Matsushita, W. Sakai, K. Nakajima, M. Suzuki, K. Kimura, A. Agarwal, H.-J. Gossmann, M. Ameen
Nucl. Instr. and Meth. B 230 (2005) 230.

53. *Neutralization rate for slow Ar^+ ions in front of KCl(001)*

T. Tsujioka, S. Tanaka, A. Nakamoto, K. Nakajima, M. Suzuki, K. Kimura
Nucl. Instr. and Meth. B 230 (2005) 369.

54. *Si emission from the SiO_2/Si interface during the growth of SiO_2 in the HfO_2/SiO_2/Si structure*
Z. Ming, K. Nakajima, M. Suzuki, K. Kimura, M. Uematsu, K. Torii, S. Kamiyama, Y. Nara, K. Yamada
Appl. Phys. Lett. 88 (2006) 153516.

55. *In-line aligned and bottom-up Ag nanorods for surface-enhanced Raman spectroscopy*
M. Suzuki, W. Maekita, Y. Wada, K. Nakajima, K. Kimura, T. Fukuoka, Y. Mori
Appl. Phys. Lett. 88 (2006) 203121.

56. *Convoy electrons emitted by 2-MeV He^+ ions at grazing incidence on KCl(001)*
K. Nakajima, A. Nakamoto, M. Suzuki, K. Kimura
Nucl. Instr. and Meth. B 248 (2006) 21.

57. *Vapor phase growth of Al whiskers induced by glancing angle deposition at high temperature*
M. Suzuki, K. Nagai, S. Kinoshita, K. Nakajima, K. Kimura, T. Okano, K. Sasakawa
Appl. Phys. Lett. 89 (2006) 133103.

58. *The analysis of a thin $SiO_2/Si_3N_4/SiO_2$ stack: A comparative study of low-energy heavy ion elastic recoil detection, high-resolution Rutherford backscattering and secondary ion mass spectrometry*
B. Brijs, T. Sajavaara, S. Giangrandi, T. Janssens, T. Conard, K. Arstila, K. Nakajima, K. Kimura, A. Bergmaier, G. Dollinger, A. Vantomme, W. Vandervorst
Nucl. Instr. and Meth. B 249 (2006) 847.

59. *Measurement of the strain in strained-Si/$Si_{0.79}Ge_{0.21}$ with*

HRBS/channeling
T. Matsushita, W. Sakai, K. Nakajima, M. Suzuki, K. Kimura, A. Agarwal, H.-J. Gossmann, M. Ameen, H. Harima
Nucl. Instr. and Meth. B 249 (2006) 432.

60. *Accumulation of hydrogen near the interface between ultrathin SiO_2 and Si(001) under ion irradiation in high-resolution elastic recoil detection*
K. Nakajima, R. Imaizumi, M. Suzuki, K. Kimura
Nucl. Instr. and Meth. B 249 (2006) 425.

61. *Observation of Si emission during thermal oxidation of Si(001) with high-resolution RBS*
S. Hosoi, K. Nakajima, M. Suzuki, K. Kimura, Y. Shimizu, S. Fukatsu, K.M. Itoh, M. Uematsu, H. Kageshima, K. Shiraishi
Nucl. Instr. and Meth. B 249 (2006) 390.

62. *Observation of the interfacial layer in HfO_2(10 nm)/Si by high-resolution RBS in combination with grazing angle sputtering*
W. Sakai, K. Nakajima, M. Suzuki, K. Kimura, B. Brijs
Nucl. Instr. and Meth. B 249 (2006) 238.

63. *Observation of lattice strain near interface using high-resolution RBS*
K. Nakajima, M. Suzuki, K. Kimura
J. Vac. Soc. Jpn. 49 (2006) 286 (in japanese).

64. *Isotopic labeling study of the oxygen diffusion in $HfO_2/SiO_2/Si$*
M. Zhao, K. Nakajima, M. Suzuki, K. Kimura, M. Uematsu, K. Torii, S. Kamiyama, Y. Nara, H. Watanabe, K. Shiraishi, T. Chikyow, K. Yamada
Appl. Phys. Lett. 90 (2007) 133510.

65. *Influence of elastic scattering of photoelectrons on angle-resolved x-ray photoelectron spectroscopy*
K. Kimura, K. Nakajima, T. Conard, W. Vandervorst
Appl. Phys. Lett. 91 (2007) 104106.

66. *Subsurface structures in initial stage of $FeSi_2$ growth studied by high-resolution Rutherford backscattering spectroscopy*
M.Suzuki, K. Kinoshita, S. Jomori, H. Harada, K. Nakajima, K. Kimura
Thin Solid Films 515 (2007) 8281.

67. *In situ observation of oxygen gettering by titanium overlayer on $HfO_2/SiO_2/Si$ using high-resolution Rutherford backscattering spectroscopy*
K. Nakajima, A. Fujiyoshi, Z. Ming, M. Suzuki, K. Kimura
J. Appl. Phys. 102 (2007) 064507.

68. *Neutralization of slow C_{60}^+ ions in front of KCl(001) surface*
S. Tamehiro, T. Matsushita, K. Nakajima, M. Suzuki, K. Kimura
Nucl. Instr. and Meth. B 256 (2007) 16.

69. *Secondary ion emission from a KCl(001) surface by grazing-angle incidence of swift heavy ions*
K. Nakajima, S. Yamasaki, M. Suzuki, K. Kimura
Nucl. Instr. and Meth. B 256 (2007) 524.

70. *Au nanorod arrays tailored for surface-enhanced Raman spectroscopy*
M. Suzuki, K. Nakajima, K. Kimura, T. Fukuoka, Y. Mori
Analytical Sciences 23 (2007) 829.

71. *Morphological evolution of Al whiskers grown by high temperature glancing angle deposition*
M. Suzuki, K. Nagai, S. Kinoshita, K. Nakajima, K. Kimura, T. Okano, K. Sasakawa
J. Vac. Sci. Technol. A 25 (2007) 1096.

72. *Effect of oblique-angle deposition on early stage of Fe–Si growth*
H. Harada, S. Jomori, M. Suzuki, K. Kinoshita, K. Nakajima, K. Kimura
Thin Solid Films 515 (2007) 8277.

73. *Energy loss of slow C_{60}^+ ions during grazing scattering from a*

KCl(001) surface
T. Matsushita, K. Nakajima, M. Suzuki, K. Kimura
Phys. Rev. A 76 (2007) 032903.

74. *Principles and Precision of high-resolution RBS*
K. Kimura, K. Nakajima
J. Surf. Surf. Soc. Jpn. (Hyomen kagaku) 28 (2007) 626 (in japanese).

75. *Observation of molecular ordering at the surface of trimethylpropylammonium bis(trifluoromethanesulfonyl)imide using high-resolution rutherford backscattering Spectroscopy*
K. Nakajima, A. Ohno, M. Suzuki, K. Kimura
Langmuir 24 (2008) 4482.

76. *Combination of high-resolution RBS and angle-resolved XPS: accurate depth profiling of chemical states*
K. Kimura, K. Nakajima, M. Zhao, H. Nohira, T. Hattori, M. Kobata, E. Ikenaga, J.J. Kim, K. Kobayashi, T. Conard, W. Vandervorst
Surf. Interface Anal. 40 (2008) 423

77. *Ag nanorod arrays tailored for surface-enhanced Raman imaging in the near-infrared region*
M. Suzuki, W. Maekita, Y. Wada, K. Nagai, K. Nakajima, K. Kimura, T. Fukuoka, Y. Mori
Nanotechnology 19 (2008) 265304.

78. *Surface analysis using high-resolution Rutherford backscattering spectroscopy*
K. Kimura, K. Nakajima
J. Vac. Soc. Jpn. 51 (2008) 613 (in japanese).

79. *Characterization of surfaces and interfaces by high-resolution RBS*
K. Nakajima, K. Kimura
J. Surf. Finish. Soc. Jpn. 59 (2008) 882 (in japanese).

80. *Surface structure of an ionic liquid with high-resolution Rutherford*

backscattering spectroscopy
K. Nakajima, A. Ohno, M. Suzuki, K. Kimura
Nucl. Instr. and Meth. B 267 (2009) 605.